Theory of semiconductor superlattice electronic structure

D. L. Smith

Los Alamos National Laboratory, Los Alamos, New Mexico 87545

C. Mailhiot*

Xerox Webster Research Center, Webster, New York 14580

The authors review the theory of semiconductor superlattice electronic structure. First a survey of theoretical methods is presented. These methods can be divided into two general classes: the supercell approach in which the superlattice is viewed as a material with a large unit cell, and the boundary-condition approach in which bulk wave functions in the constituent semiconductors are matched at the superlattice interfaces. Supercell approaches are essentially the same as conventional band-structure methods. They can only be applied to thin-layer superlattices because of numerical cost. The authors discuss problems of interface matching that occur in various boundary-condition methods and relate these methods to each other. A particular boundary-condition method is used to discuss the electronic structure of various III-V semiconductor superlattices. Emphasis is placed on discussing the qualitatively different behavior that can arise because of different energy-band lineups, strain conditions, and growth orientations. The authors compare the results of three commonly used boundary-condition methods and find generally good agreement.

CONTENTS

I. INTRODUCTION

In this article we review the theory of semiconductor superlattice electronic structure. We specifically consider one-electron (band-structure) theories of compositional superlattices. We concentrate on superlattices whose constituent materials are zinc-blende-structure semiconductors. This subject is related to the theory of semiconductor heterojunctions and the electronic properties of two-dimensional systems. Reviews of various properties of superlattices are included in *Synthetic Modulated Structures* edited by Chang and Giessen (1985). The paper by Schulman and McGill (1985c) in that volume, on the theory of superlattices, is complementary to this article. Reviews on superlattices have also been edited by Chang and Ploog (1985) and Dingle (1987). A review by Ploog and Döhler (1983) concentrates on doping superlattices. The electronic properties of two-dimensional systems has been reviewed by Ando, Fowler, and Stern (1982). Properties of semiconductor heterojunctions have been reviewed by Cohen (1980), Kroemer (1983, 1985), and Pollmann and Mazur (1983).

A. Overview

The idea of semiconductor superlattices was originated by Esaki and Tsu (1970). (For a discussion of the history of semiconductor superlattices, see Esaki, 1985a, 1985b.) Two kinds of superlattices were envisioned: compositional and doping. Compositional superlattices consist of alternating layers of two different semiconductors. The thickness of the individual layers is between a few angstroms and a few hundred angstroms. The composition variation modulates the electronic potential on a length scale shorter than an electron mean free path. Doping superlattices consist of alternating n- and p-type layers of a single semiconductor. Electric fields generated by the charged dopants modulate the electronic potential. More recently, superlattices in which both the composition and the doping are modulated have been considerd (Döhler, 1981).

The first attempt to grow superlattices used the chemical vapor deposition technique in the $GaAs/GaAs_{1-x}P_x$

---

*Present address: Lawrence Livermore National Laboratory, Livermore, CA 94550.

$(0.1 \le x \le 0.5)$ materials systems (Blakeslee and Aliotta, 1970; Esaki, Chang, and Tsu, 1970). The relatively large lattice-constant mismatch (1.8% between GaAs and $GaAs_{0.5}P_{0.5}$) caused difficulties in these early growth experiments. Subsequently, the $GaAs/Ga_{1-x}Al_xAs$ materials system was considered (Cho, 1971; Woodall, 1972). The lattice-constant mismatch (0.08% between GaAs and $Ga_{0.5}Al_{0.5}As$) is very small in this system. Observations of negative differential resistance (Esaki *et al.*, 1972) were the first evidence of quantum confinement effects in a superlattice. Since then, the $GaAs/Ga_{1-x}Al_xAs$ system has been extensively studied by both electrical transport and optical techniques. It is by far the most thoroughly investigated superlattice.

The band gap of GaAs is smaller than that of $Ga_{1-x}Al_xAs$. In a $GaAs/Ga_{1-x}Al_xAs$ heterojunction, the conduction-band edge in GaAs lies at a lower energy than the conduction-band edge in $Ga_{1-x}Al_xAs$ and the valence-band edge in GaAs lies at a higher energy than the valence-band edge in $Ga_{1-x}Al_xAs$. Thus the GaAs acts as a quantum well and the $Ga_{1-x}Al_xAs$ as a potential barrier both for electrons and for holes. Because of the very close match of lattice constants in this materials system, the constituent materials are not significantly strained. Therefore the heavy- and light-hole band edges of the constituent materials remain essentially degenerate.

As epitaxial growth techniques, especially molecular-beam epitaxy (MBE) and metal-organic chemical vapor deposition (MOCVD), improved, it became possible to investigate a wider range of materials systems. Qualitatively, new physical effects can occur in materials systems other than $GaAs/Ga_{1-x}Al_xAs$. One origin for such new effects is a different lineup of the conduction and valence bands of the constituent materials at the superlattice interfaces. The InAs/GaSb system is fairly closely lattice matched (0.6% difference), but the relative energies of the band edges are quite different from those in $GaAs/Ga_{1-x}Al_xAs$. In an InAs/GaSb heterojunction, the InAs conduction-band edge lies lower in energy than the GaSb valence-band edge (Sai-Halasz, Tsu, and Esaki, 1977; Sakaki *et al.*, 1977; Sai-Halasz, Esaki, and Harrison, 1978). In an InAs/GaSb superlattice, electrons are confined in the InAs, whereas holes are confined in the GaSb. (Superlattices with a $GaAs/Ga_{1-x}Al_xAs$-type band-edge lineup are called type I, whereas superlattices with an InAs/GaSb-type band-edge lineup are called type II.) Intermediate band-edge lineups have been achieved in the $In_{1-x}Ga_xAs/GaSb_{1-y}As_y$ system (Sai-Halasz, Chang, *et al.*, 1978). (The alloy compositions, x and y, were constrained so that the two constituent materials were lattice matched.) By choosing the alloy compositions (within the lattice matching constraint), one can adjust the conduction-band edge of $In_{1-x}Ga_xAs$ to be higher or lower in energy than the valence-band edge of $GaSb_{1-y}As_y$. Another interesting case occurs in the HgTe/CdTe materials system (Schulman and McGill, 1979b). In this system (lattice-constant mismatch of 0.3%), the HgTe is a zero-band-gap semiconductor. The valence and conduction bands of HgTe, which have the same energy, lie within the CdTe band gap.

Lattice-mismatched heterostructures can be grown with essentially no misfit defect generation if the layers are sufficiently thin (Frank and van der Merwe, 1949; Frank, 1963). The lattice-constant mismatch is accommodated by coherent strain in the individual layers. This effect was first explored in the context of semiconductor superlattices by Matthews and Blakeslee (1974, 1975, 1976). Removal of the close lattice-constant matching constraint greatly extended the number of superlattice materials systems that could be considered. In addition, Osbourn (1982a, 1982b, 1983, 1984, 1985) showed that the lattice-constant-mismatch-induced strain caused interesting new behavior in such strained-layer superlattices by deformation-potential effects. Strain changes the band gaps of the constituent materials and splits the degeneracy of the zone-center heavy- and light-hole bands. In Fig. 1 we show a schematic diagram of the band-edge lineup for type-I and type-II superlattices for three lattice-constant conditions: equal lattice constants, the lattice constant of material A greater than that of material B, and the lattice constant of material A less than that of material B. One sees that a rich range of possibilities exists. The epitaxial growth of high-quality strained-layer superlattices has been conclusively demonstrated (Osbourn, Biefeld, and Gourley, 1982; Fritz, Dawson, and Zipperian, 1983).

Most superlattices have been grown along the [001] crystallographic axis. Recently, lattice-matched $GaAs/Ga_{1-x}Al_xAs$ superlattices have been grown along the [111] axis and the optical spectroscopy of this superlattice has been studied (Hayakawa, Takahashi, *et al.*, 1988a, 1988b). Qualitatively, new behavior has been predicted in strained-layer superlattices with axis other than [001] because of piezoelectrically generated polarization fields (Smith, 1986; Smith and Mailhiot, 1988b). In particular, for a [111] growth axis, large (exceeding 10^5 V/cm) electric fields, which alternate in polarity in the two constituent materials making up the superlattice, are predicted. Epitaxial growth of strained layers along a [111] axis has been demonstrated (Elcess, Liévin, and Fonstad, 1988). Evidence for the predicted piezoelectric effects has been presented (Beery *et al.*, 1989; Laurich *et al.*, 1989).

A wide range of superlattice systems has been grown and studied. Established epitaxial growth techniques are capable of growing many new systems that have not yet been investigated. Because of different band-edge lineups, strain conditions, and growth orientations, the various materials systems can show qualitatively different physical behavior. The electronic structure of a superlattice depends on the layer thicknesses as well as on the constituent materials. Because the layer thicknesses can be precisely controlled, superlattices allow us to design the electronic band structure of semiconducting materials. The flexibility in electronic properties that is intro-

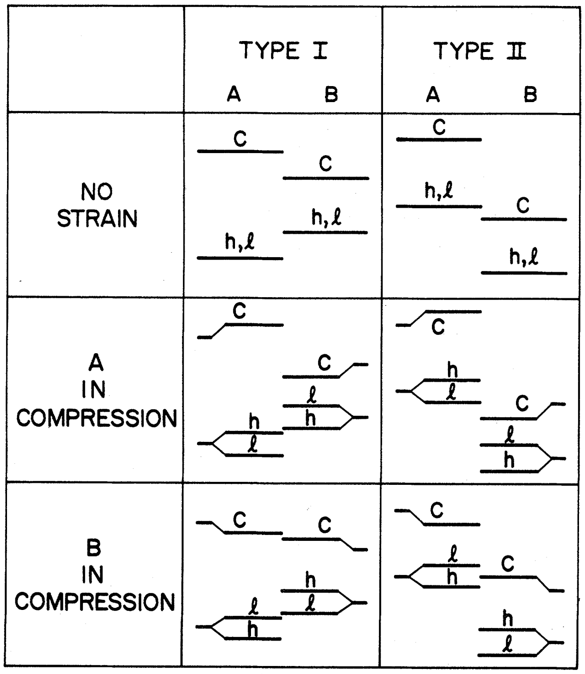

FIG. 1. Schematic illustration of the band-edge lineup in type-I and type-II superlattices. Band lineups for three strain conditions are shown.

duced by this design possibility makes superlattices useful in several technological applications, including semiconductor diode lasers (see, for example, van der Ziel *et al.*, 1975; Holonyak *et al.*, 1980; and Tsang, 1981); electro-optic modulators (see, for example, Miller *et al.*, 1984a, 1984b, 1985; Chang, Schulman, and Efron, 1987; Wood, Tkach, and Chraplyvy, 1987; and Mailhiot and Smith, 1988c); nonlinear optical materials (see, for example, Bloss and Friedman, 1982, 1983; Chemla *et al.*, 1984; Cooperman, Friedman, and Bloss, 1984; Chang, 1985a, 1985b; and Smith and Mailhiot, 1987b, 1987c); and infrared detectors (see, for example, Smith, McGill, and Schulman, 1983; Osbourn, 1984; Smith and Mailhiot, 1987a; Goossen, Lyon, and Alavi, 1988; Kurtz *et al.*, 1988; and Levine *et al.*, 1988).

Electronic-structure theory has a unique role to play in superlattice research because of the rich variety of possible materials systems. Theory can be used to invent structures that exhibit new physical phenomena. In some cases, these phenomena may have technological applications. Theory can also be used to tailor superlattice electronic structures either to enhance the observation of a particular effect or to optimize the material for a technological purpose. There is an essential difference between the role of electronic-structure theory in superlattice research and its role in research in conventional semiconductors. For conventional semiconductors, theory can be used to describe the electronic structure and to interpret experiments that depend on the electronic structure. There are, however, few parameters available with which to design new materials. The large number of potential superlattice systems allows great freedom in materials design. Theory can play an important role in this design process.

The energy offsets between corresponding bands in the constituent materials of a superlattice are typically on the order of a few hundred meV. Modifications in the electronic structure due to the periodic superlattice potential are on this energy scale. Thus a theoretical description of superlattice electronic structure must deal with questions on this energy scale. Those electronic states whose mean free path is comparable to or longer than the thickness of the constituent material layers are significantly influenced by the spatial modulation of the superlattice. States whose mean free path is much less than the thickness of the constituent material layers are essentially kinetically confined within a particular material. Such states, therefore, are not much modified by superlattice modulation. As a result, electronic states relatively close in energy to band edges, which have relatively long lifetimes and mean free paths, are of greatest interest in superlattice materials. Thus theories of superlattice electronic structure are band-edge theories. (Secondary energy minima can also be important.) It is seldom of interest to describe superlattice electronic structures on the scale of bonding and antibonding bandwidths (a few tens of eV). Instead one cares about a detailed description of the band edges. Perturbations such as the spin-orbit interaction, strain, and electric fields are important on the energy scale of interest. These considerations are important in choosing a theoretical approach to superlattice electronic structure. For example, a theory that neglected the spin-orbit interaction could not be expected to give a meaningful description of superlattice valence bands on the energy scale of interest.

This paper has two principal purposes. The first is to survey and to compare the theoretical methods used for electronic-structure calculations of semiconductor superlattices. A wide variety of methods has been used; we try to clarify the connections between the various methods. In the remainder of this section we present a broad survey of approaches. In the next section we discuss three frequently used empirical approaches, based on the pseudopotential, **k**·**p**, and tight-binding methods, in more detail. We specifically consider why the basis sets used in these methods (plane waves, zone-center Bloch functions, and local atomic-centered orbitals) lead to different types of calculations. We discuss the problems that arise in wave-function matching in the pseudopotential and **k**·**p** methods. In Sec. IV, results of three specific numerical calculations on two superlattices are compared in detail.

The second principal purpose of the article is to discuss the results of electronic-structure calculations for various superlattice systems. The results of such calculations are presented in Sec. III. We describe the wide range of physical effects that can be achieved in different superlattice systems. In our view, one of the most interesting challenges in the physics of semiconductor superlattices is to utilize the power of modern epitaxial growth techniques to invent new physical structures that show interesting and technologically important new properties. We hope that the description of what has been done to date will prove useful in continuing this process of invention. To some extent the two purposes of the article can be separated. For example, it would be possible to read about the results of electronic-structure calculations discussed in Sec. III without reading about the methods for performing these calculations discussed in Sec. II.

B. Survey of theoretical methods

A very wide range of theoretical techniques has been applied to superlattice electronic-structure calculations. The degree of complexity in these approaches ranges from scaled Kronig-Penney models to self-consistent many-electron calculations. For this survey, we divide the various approaches that have been used into two groups; empirical methods and *ab initio* methods.

Which theoretical approach is most appropriate depends both on the material system studied and on the questions asked about that material system. For example, the GaAs/$Ga_{1-x}Al_xAs$ ($x \sim 0.2$) superlattice is relatively easy to describe theoretically. Both constituent materials have direct band gaps; they are relatively wide-band-gap semiconductors; the band lineups are type I; and the constituent materials are closely lattice matched. As a result of these simplifying features, there is little mixing of constituent material bands with different bulk symmetry in the superlattice wave functions, and Kronig-Penney models scaled by the appropriate effective masses and with barrier potentials given by the band discontinuities provide a fairly good description of the zone-center energy levels. For more complex materials systems (e.g., small-band-gap materials or type-II band lineups in which band mixing can become important) or for more complex questions (e.g., details of the dispersion relations), more sophisticated theoretical approaches become necessary.

1. Empirical methods

In these approaches, the electronic structure of the constituent materials is assumed to be understood and to be described by a parametrized bulk model. The parameters of the bulk model are assumed not to change when the constituent materials are combined to form the superlattice. In addition to the bulk constituent materials, the interface region must be described. For virtually all of the empirical methods, a valence-band offset must be specified. This offset, combined with the bulk electronic-structure models, will determine the rest of the band lineups. In some approaches, additional parameters are required to describe the interface. For example, in tight-binding models, matrix elements between orbitals on near-neighbor atoms at opposite sides of the interface must be specified. To date, most theoretical information on superlattices has been obtained through empirical methods.

We shall divide our discussion of empirical methods into "supercell approaches" and "boundary-condition approaches." By "supercell approaches" we mean methods in which the superlattice is described by a Hamiltonian with a large unit cell and the eigenfunctions of the Hamiltonian are found by conventional band-structure methods. By "boundary-condition approaches" we mean methods in which the eigenfunctions of the superlattice Hamiltonian are found by matching wave functions in each of the constituent materials at the superlattice interfaces. In principle, these two kinds of approaches are, of course, equivalent and would yield the same results for a given Hamiltonian. Operationally, however, these two approaches lead to rather different kinds of calculations.

a. Supercell approaches

Except for the scaled Kronig-Penney-type models, the first superlattice electronic-structure calculations were done using supercell approaches. A principal advantage of these approaches is their conceptual simplicity. A principal disadvantage is that the dimension of matrices that must be diagonalized increases rapidly with the thickness of the superlattice period. Thus they are restricted to rather thin-layer superlattices. Empirical pseudopotential and tight-binding models have been investigated using supercell approaches.

Empirical pseudopotential calculations were performed on thin-layer GaAs/$Ga_{1-x}Al_xAs$ superlattices using the supercell approach by Caruthers and Lin-Chung (1977, 1978a, 1978b) and Andreoni, Baldereschi, and Car (1978). In both calculations, screened atomic pseudopotentials were expressed as form factors, which were empirically determined, and wave functions were expanded in terms of plane waves. The number of plane waves required increases linearly with the thickness of the superlattice period. Caruthers and Lin-Chung used about 190 plane waves for a superlattice consisting of one layer each of GaAs and AlAs. Full calculations on superlattices consisting of up to three molecular layers of each constituent material were performed. Because of the rapid increase in computing cost with layer thickness, only these very-thin-layer superlattices could be considered. The results of the two sets of calculations were rather different. This difference arose because different sets of pseudopotential form factors were used by the two groups. As always with empirical methods, the choice of the input parameters (in this case the pseudopotential form factors) is important. For these superlattice calculations, a larger number of form factors (and thus a larger number of input parameters) enter than in bulk zinc-blende-structure semiconductor calculations. In particular, the zero-wave-vector form factors determine the valence-band offset. These calculations did not include the spin-orbit interaction. To do so, it would have been necessary to double the dimension of the matrices that were diagonalized.

Tight-binding calculations were performed on $GaAs/Ga_{1-x}Al_xAs$ superlattices by Schulman and McGill (1977, 1979a); on InAs/GaSb superlattices by Nucho and Madhukar (1978), Madhukar, Dandekar, and Nucho (1979), and Madhukar and Nucho (1979); on CdTe/HgTe superlattices by Schulman and McGill (1979b, 1979c, 1981); on Si/GaP superlattices by Madhukar and Delgado (1981); and on $GaAs/GaAs_{1-x}P_x$ superlattices by Osbourn (1982a, 1982b) using the supercell approach. In these calculations, a tight-binding basis, typically one *s*-type function and three *p*-type functions centered at each atom, was chosen, and Hamiltonian matrix elements between these functions were parametrized. The basis functions were usually taken to be orthonormal and matrix elements out to second-nearest neighbors were included. [More recently, tight-binding models including five orthonormal basis functions and only first-nearest-neighbor interactions have become popular (Vogl, Hjalmarson, and Dow, 1983).] The tight-binding parameters are typically fixed by fitting to a bulk band structure. (The basis functions themselves are not actually specified.) This fitting procedure does not uniquely specify the tight-binding parameters, and considerable care needs to be taken in selecting them. Harrison (1980) has discussed the physical basis for choosing tight-binding parameters. Bulk valence bands can usually be fit fairly well, but the conduction bands tend to be too flat (i.e., the electron effective masses tend to be too large). Valence-band offsets are set by adjusting the on-site energy parameters in the two constituent materials. Overlap parameters between basis functions on opposite sides of the interface are specified by an extrapolation scheme. (There really is no unambiguous way to choose these parameters.) The spin-orbit interaction was included in the calculations on the CdTe/HgTe and $GaAs/GaAs_{1-x}P_x$ superlattices by Schulman and McGill and by Osbourn, respectively. It was ignored in the other calculations. The spin-orbit interaction is described by spin-dependent Hamiltonian matrix elements between *p*-type orbitals on the same site (Chadi, 1977a). In strained-layer superlattices, overlap matrix elements are adjusted to give known bulk deformation potentials (Osbourn, 1982a, 1982b).

After the superlattice tight-binding model has been specified by these parameters, the Hamiltonian matrix is constructed (Schulman and McGill, 1979a). If the spin-orbit interaction is ignored, the dimension of the Hamiltonian matrix is $(M+N)n$, where M and N are the number of molecular layers of each of the two constituent materials in the superlattice period and n is the number of basis functions, typically eight, in a bulk unit cell. If the spin-orbit interaction is included, the dimension of the Hamiltonian is doubled. Because the dimension of the Hamiltonian gets quite large for thick-period superlattices, this approach has been restricted to periods of about 20 molecular layers (~ 60 Å) or less.

Recently, a new supercell method for performing empirical pseudopotential calculations of superlattice electronic structure has been developed by Jaros and co-workers (Jaros, Wong, and Gell, 1985; Jaros, Wong, Gell, and Wolford, 1985; Ninno *et al.*, 1985; Gell, Ninno, Jaros, and Herbert, 1986; Gell, Wong, Ninno, and Jaros, 1986; Morrison, Jaros, and Wong, 1987; Morrison and Jaros, 1988). In this method, the superlattice Hamiltonian is written as the sum of two terms,

$$H = H_0 + V \ , \tag{1.1}$$

where H_0 has zinc-blende symmetry. For example, H_0 might be the bulk Hamiltonian of one of the constituent materials, or else it might be an average of the bulk Hamiltonians of the constituents—that is, a virtual-crystal approximation Hamiltonian for the alloy that would result if the superlattice were randomized. The perturbation V reduces the symmetry to that of the superlattice. In the calculation, a superlattice wave vector $\mathbf{q}$ is chosen and the eigenfunctions of H_0 are found for all zinc-blende wave vectors that fold into $\mathbf{q}$. These eigenfunctions of H_0 are then used as a basis set in which to diagonalize H. For any superlattice wave vector, $N+M$ zinc-blende wave vectors fold into it (where N and M are the number of molecular layers of each of the constituent materials in the superlattice period). The dimension of the superlattice Hamiltonian is $(N+M)n$, where n is the number of bands in the model for the zinc-blende Hamiltonian. At first it appears that this method has the same problems with thick-period superlattices as the other supercell approaches. However, because V is expected to be weak and one usually only cares about a limited energy range, the matrix V can be truncated around the zeroth-order eigenvalues (i.e., eigenvalues of H_0) that are near the energy range of interest. Thus unlike the other supercell approaches, this method allows one to take advantage of the inherent simplifying features of the superlattice problem.

b. Boundary-condition approaches

The superlattice electronic-structure problem has a number of simplifying features. One usually cares only about results in a small energy region near the band edges. The electronic structure of the bulk constituent materials is well understood. The size of the perturbing superlattice potential is not large on the scale of bonding and antibonding bandwidths. Except for the method of Jaros and co-workers, the supercell approaches do not take advantage of these simplifying features. They lead to large-dimensional Hamiltonians that describe a much larger energy region than is of interest. A great deal of computer time is required to diagonalize these matrices of large dimensionality. Only a small fraction of the eigenvalues and eigenfunctions are of any interest.

Boundary-condition approaches attempt to take advantage of the simplifying features of the problem. In these approaches, eigenfunctions of the constituent materials are matched at the superlattice interfaces to construct a superlattice eigenfunction. They generally lead to smaller-dimensional matrices than those in the supercell approaches. The matrices that appear in the boundary-condition approaches generally do not increase in dimension with increasing superlattice period. This feature is the principal advantage of these methods. There is a close connection between the single-interface problem (i.e., two semi-infinite material slabs joined at an interface) and the superlattice problem described by boundary-condition approaches. We consider empirical pseudopotential, tight-binding, and $\mathbf{k}\cdot\mathbf{p}$ methods.

Empirical pseudopotential calculations using a boundary-condition approach have been applied to the single-semiconductor-interface problem (Marsh and Inkson, 1984a, 1984b, and 1986) but not to superlattices themselves. In principle, these methods could be extended to describe superlattices. The bulk Hamiltonians describing the two semiconductors are parametrized by a set of pseudopotential form factors, and the energies in the two bulk materials are related by an empirically given valence-band offset. The interface does not mix bulk wave functions in the two semiconductors with different values of wave vector parallel to the interface, $\mathbf{k}_{\parallel}$. A value of $\mathbf{k}_{\parallel}$ and energy E is chosen. The bulk wave functions are expanded in a finite series of plane waves of the form $|\mathbf{k}+\mathbf{G}\rangle$, where $\{\mathbf{G}\}$ is a finite set of reciprocal lattice vectors and $\mathbf{k}$ has the projection $\mathbf{k}_{\parallel}$ on the interface plane. An eigenvalue equation for $k_{\perp}$, the component of $\mathbf{k}$ normal to the interface, is solved (Pendry, 1969; Chang and Schulman, 1982a). The eigenvectors for this equation give the expansion coefficients for the bulk material wave functions. The value of $k_{\perp}$ can be either real or complex. Complex values of $k_{\perp}$ correspond to evanescent bulk states (Heine, 1963; Jones, 1966). Boundary conditions far from the interface are fixed. For example, the coefficients of evanescent states that grow away from the interface must certainly vanish. Typically, the coefficients of Bloch (real $k_{\perp}$) states traveling toward the interface are specified. Expansion coefficients for the bulk eigenfunctions making up the heterojunction wave function are determined by requiring that the heterojunction wave function and its derivative be continuous at the interface. When a finite amplitude for at least one incoming Bloch state is specified, the equation for the expansion coefficients is an inhomogeneous linear equation. If the coefficients of all incoming Bloch states are set to zero, the equation for the expansion coefficients becomes a homogeneous linear equation. A nontrivial solution to this equation would correspond to a bound interface state.

In practice, complications arise in the procedure described. In particular, after the plane-wave basis set has been truncated to a finite number of reciprocal lattice vectors, the Hamiltonian matrix no longer has translational symmetry. As a result, when the bulk complex band-structure eigenvalue equation is solved, spurious out-of-zone solutions result. In principle, these solutions should simply correspond to repeated-zone solutions. However, because of the loss of translational symmetry by the truncation procedure, they do not. Simply dropping the spurious solutions causes the interface matching equations to be overspecified (too many equations for the number of unknown coefficients). It also destroys formal completeness relations from which one deduces flux conservation. Fortunately, coupling to the spurious solutions is usually quite weak, and "common-sense" truncation procedures work pretty well in practice. Analogous problems arise in $\mathbf{k}\cdot\mathbf{p}$ approaches and other methods in which the Hamiltonian loses translational symmetry when the basis set is truncated to a finite set. We discuss these questions more extensively in Sec. II.

Tight-binding calculations using a boundary-condition approach have also been applied to problems involving one interface or a small number of interfaces (Osbourn and Smith, 1979a, 1979b; Osbourn, 1980, 1981; Mailhiot, McGill, and Schulman, 1983; Mailhiot, Smith, and McGill, 1983). These calculations are generally similar to the analogous pseudopotential calculations. Efficient methods for solving the complex band-structure problem in a tight-binding basis have been developed (Chang, 1982; Chang and Schulman, 1982a). The interface boundary conditions are given by tight-binding equations that depend on the overlap parameters between basis functions on opposite sides of the interface. One major difference between the pseudopotential and tight-binding calculations occurs because the truncated (finite-dimensional) bulk tight-binding Hamiltonian matrix has translational symmetry. As a result, no spurious out-of-zone solutions occur in the tight-binding complex band structure. There are no truncation problems such as those that occur in the pseudopotential calculations. Evanescent states with very large decay constants do occur in the tight-binding complex band structure. (Such states also occur in the pseudopotential complex band structure.) These states cannot be considered physically significant. However, they couple extremely weakly to physically significant states and do not cause real problems with the calculations.

Tight-binding calculations using a boundary-condition approach have been applied to superlattice electronic-structure calculations by Schulman and Chang (1981, 1983). The complex band structure is calculated (Chang and Schulman, 1982a) using a transfer-matrix method (Lee and Joannopoulos, 1981a, 1981b). The Bloch and evanescent states in the constituent materials are used to construct a reduced Hamiltonian. This Hamiltonian is diagonalized for a given superlattice wave vector to determine a superlattice energy eigenvalue and wave function. The basis set, constituent-material Bloch and evanescent states, is energy dependent. For consistency, the scheme must be iterated until the input and output energies agree. Spin orbit and strain (in strained-layer superlattices) have been included (Chang and Schulman, 1983, 1985; Schulman and Chang, 1985a, 1986). The dimension of the matrices that must be diagonalized is independent of the superlattice period and is of modest size. For the five-orbital-per-atom and first-nearest-neighbor tight-binding model (including the spin-orbit interaction), 40×40 matrices are required to describe a [001] interface. For the four-orbital-per-atom and second-nearest-neighbor tight-binding model (including the spin-orbit interaction), 64×64 matrices are required to describe a [001] interface. Calculations of this type are currently the state of the art for superlattice tight-binding calculations. The approach has many advantages: it has modest-dimensional matrices that do not depend on the superlattice period; it has the ability to handle spin-orbit and strain interactions; it can be adapted to optical calculations; and it treats the entire Brillouin zone. Thus, for example, superlattices made from indirect band-gap materials can be described. The disadvantages of the approach are those common to tight-binding methods: a large number of input parameters are required; the relation between the various input parameters and the results is complex; the bulk tight-binding parameters are not uniquely specified by the bulk band structure; there is no clear prescription for determining the interface tight-binding parameters; and the bulk conduction-band dispersion is usually too flat.

It is the band-edge states of superlattices that are of primary interest. In bulk semiconductors, $\mathbf{k}\cdot\mathbf{p}$ theory is particularly effective at describing states near the conduction- and valence-band edges (Dresselhaus, Kip, and Kittel, 1955; Luttinger and Kohn, 1955; Kane, 1956, 1957, 1966; Luttinger, 1956; Cardona and Pollak, 1966; Pollak and Cardona, 1966). For this reason, it is natural to consider $\mathbf{k}\cdot\mathbf{p}$ methods for describing these states in superlattices. The first theoretical efforts to describe superlattices were based on Kronig-Penney-type models scaled by bulk effective masses and energy-band offsets. (Because the effective-mass picture is based on $\mathbf{k}\cdot\mathbf{p}$ theory, the scaled Kronig-Penney models can be viewed as a simple $\mathbf{k}\cdot\mathbf{p}$ method.) These models had considerable success in describing the optical properties of GaAs/$\mathrm{Ga}_{1-x}\mathrm{Al}_x\mathrm{As}$ superlattices (Dingle, Wiegmann, and Henry, 1974; Dingle, Gossard, and Wiegmann, 1975). Modifications of the scaled Kronig-Penney model, within a one-band framework, to include nonparabolicity and the fact that the constituent materials have different bulk effective masses were made by Mukherji and Nag (1975). Sham and Nakayama (1979) discussed the effective-mass picture in the presence of an interface from a somewhat more fundamental point of view. They specifically considered the Si/SiO_2 interface that occurs in Si MOSFET's.

The scaled Kronig-Penney-type models do not include coupling between different bulk bands by the superlattice potential. In type-I superlattices made from relatively wide-band-gap constituent semiconductors, such as GaAs/$\mathrm{Ga}_{1-x}\mathrm{Al}_x\mathrm{As}$, these models can give the zone-center energies fairly well. They are not appropriate for superlattices in which there is extensive band mixing, such as the type-II superlattice InAs/GaSb. A two-band model, which can account for mixing between the conduction- and light-hole bands, was developed by Bastard (1981, 1982, 1985) and White and Sham (1981). These authors used rather different approaches to arrive at the same basic result. This model, which is usually called the two-band envelope-function model, has had considerable success in predicting zone-center energies and has been used extensively for interpretation of experimental data. This model can be arrived at by writing the superlattice wave function as a sum of products of zone-center Bloch functions in each constituent material and slowly varying envelope function. The Bloch functions in the constituent materials are known from bulk calculations. Coupled equations for the envelope functions are found from the bulk $\mathbf{k}\cdot\mathbf{p}$ equations and assumed interface matching conditions. The two-band envelope-function model can describe dispersion relations for a wave vector along the growth axis but not for a wave vector normal to the growth axis. Recently, Johnson *et al.* (1987) have shown that one can find superlattice effective masses for a wave vector normal to the growth axis from zone-center energies and momentum matrix elements using the f sum rule. However, dispersion relations in these directions are usually rather nonparabolic. The spin-orbit interaction was taken to be very large, so that the split-off valence band could be ignored. This is not an essential approximation, however (Taylor and Burt, 1987). The principal advantages of the method are that it is very simple to implement, there are direct and easily understood connections between the input parameters and the results, and the calculated results are easily understood on a physical basis.

The two-band envelope-function method considers mixing between the conduction- and light-hole bands, where the light-hole band is defined for the wave vector along the growth axis. It does not include mixing of the heavy-hole band (defined for the wave vector along the growth axis). This band is treated as uncoupled in a one-band model. Therefore dispersion normal to the growth axis cannot be described by this two-band model. The envelope-function method has been generalized by Altarelli and co-workers (Altarelli, 1983, 1985; Ekenberg and Altarelli, 1984; Altarelli, Ekenberg, and Fasolino, 1985). In this multiband envelope-function model, the conduction and valence bands are coupled. (The spin-orbit splitting was usually taken to be very large, so that the split-off bands were neglected. This approximation is not essential to the method, however.) Therefore, dispersion relations in any direction can be calculated. The coupled equations for the envelope functions are more complicated in the multiband model than in the two-band model, of course. These equations are usually solved approximately by variational methods. Matrices of moderately large dimensions [e.g., 72×72 in one particular application of the model (Altarelli, 1983)] result. The multiband envelope-function model has been extended to describe superlattices in magnetic fields (Fasolino and Altarelli, 1984a, 1984b; Bastard and Brum, 1986; Brum *et al.*, 1988; Lamari and Sham, 1988; Maan, 1988). It has also been used for optical properties calculations

(Chang, 1985a, 1985b; Sanders and Chang, 1985a, 1985b, 1987). The multiband envelope-function method, as formulated by Altarelli and co-workers, has a formal structure similar to that of the two-band envelope-function method as formulated by Bastard. A similar many-band model can be arrived at by expanding the superlattice wave function in terms of Bloch and evanescent states in each constituent material (Eppenga, Schuurmans, and Colak, 1987). This is analogous to the approach used by White and Sham (1981) in their derivation of the two-band envelope-function model. Burt (1988) has discussed the formulation of the envelope-function models from a somewhat different point of view.

Matching of the wave functions at the superlattice interfaces is an essential part of the various **k**·**p** approaches. Such wave-function matching is not straightforward in practice because zone-center Bloch functions, which are not usually treated explicitly in these approaches, are different in the two constituent materials. Symptoms of these problems appear even in simple one-band models because of different effective masses in the two materials (Ben-Daniel and Duke, 1966). In envelope-function approaches, differences in the zone-center Bloch functions are usually ignored. If one takes these Bloch functions to be the same in the two constituent materials, the momentum matrix elements between these Bloch functions must also be the same in the two materials. These momentum matrix elements, together with zone-center energy-band differences, determine effective masses and valence-band parameters that enter in the bulk **k**·**p** description of the constituent materials. It is inconsistent to assume that corresponding zone-center Bloch functions in the constituent materials are the same for the purpose of wave-function matching at the interface and at the same time use bulk **k**·**p** parameters for the constituent materials that imply different momentum matrix elements. Such inconsistencies can easily occur when bulk **k**·**p** parameters are determined empirically.

The present authors developed a **k**·**p** theory of superlattices in which differences in zone-center Bloch functions in the constituent materials were explicitly included (Smith and Mailhiot, 1986; Mailhiot and Smith, 1986a). A principal purpose of this work was to investigate wave-function matching conditions when the zone-center Bloch functions are different (as is really the case). The theory was worked out in a pseudopotential framework; that is, pseudo wave functions, with the core region projected out, were matched at the interface. A reference Hamiltonian was defined by averaging the bulk pseudopotentials of the constituent materials. (In the actual calculations, empirical pseudopotential form factors were used.) Zone-center eigenstates and eigenvalues were found for this reference Hamiltonian. These eigenstates formed a common basis set for the two constituent materials. The Γ_{15} valence states and Γ_1 conduction state were coupled with a spinor and treated explicitly. The spatial zone-center states closest in energy (typically 23, as actually implemented) were treated in Löwdin perturbation theory (Löwdin, 1951), with the **k**·**p** operator and the difference between the material pseudopotential and the reference Hamiltonian pseudopotential (ΔV) as the perturbation.

The calculation was carried out to first order for wave functions and second order for energies in these two interactions. Zone-center Bloch functions in the constituent materials are different because of wave-function mixing by ΔV. Had this perturbation been treated to a lower order (i.e., zeroth order for wave functions and first order for energies), the zone-center Bloch functions in the constituent materials would have been the same. The spin orbit and strain (for strained-layer superlattices) interactions were included between the explicitly treated states. Bloch and evanescent states for each bulk constituent material were computed. Matching of the bulk Bloch and evanescent states at the superlattice interfaces was accomplished using results derived about the normal component of the current-density operator. The superlattice translational symmetry was used to derive an eigenvalue equation for superlattice wave vectors and wave functions. The resulting eigenvalue equation involved matrices whose dimension did not depend on the superlattice period and was rather small (typically 12×12 as actually implemented). This **k**·**p** theory was used to investigate superlattice electronic structure (Mailhiot and Smith, 1986a, 1986b, 1987a, 1987b); optical properties (Smith and Mailhiot, 1987a, 1987b, 1988a; Mailhiot and Smith, 1988c); the effects of external stress (Mailhiot and Smith, 1987c, 1988a, 1988b); and the effects of external magnetic fields (Wu *et al.*, 1986, 1987, 1989).

Smith and Mailhiot's **k**·**p** theory is based on a systematic perturbation calculation in which the perturbation operator ($\mathbf{k}\cdot\mathbf{p}/m+\Delta V$) is kept to first order in wave functions and second order in energies. Both the bulk material Hamiltonians and the wave-function matching conditions depend on the order to which the perturbation is treated. For example, the direct momentum matrix element between the valence- and conduction-band states, which appears in terms first order in **k**·**p**, is different in the two constituent materials because of wave-function mixing by ΔV. (These terms are first order in ΔV and in **k**·**p**.) However, second-order momentum matrix elements (as well as the energy denominators that show up in the valence-band parameters) are the same in the constituent materials, since these terms are second order in **k**·**p** and therefore independent of ΔV. The order of the perturbation theory also affects the wave-function matching conditions. For example, in our theory, there is a discontinuity in the envelope function that is first order in ΔV. This discontinuity in the envelope function is necessary because of the first order in ΔV discontinuity in the zone-center Bloch functions. (It is the total wave function, which is a sum of products of envelope functions and zone-center Bloch functions, that is continuous.) If ΔV was kept only to zero order in wave functions and first order in energies, the envelope functions would be continuous. Other systematic perturbation approaches are, of course, possible. For example, the multiband envelope-function model of Altarelli (1983) can be considered as systematically treating $\mathbf{k}\cdot\mathbf{p}$ to first order in wave functions and second order in energies and ΔV to zeroth order in wave functions and first order in energies. The two-band envelope-function model of Bastard (1981, 1982, 1985) and White and Sham (1981) can be considered as systematically treating $\mathbf{k}\cdot\mathbf{p}$ and ΔV to zeroth order in wave functions and first order in energies. Our theory reduces to these envelope-function models if we calculate to lower order. Although various perturbation schemes are possible, we believe that it is important to use a systematic scheme. (This is not always done.) Otherwise one ends up with ambiguous wave-function matching conditions. Often *ad hoc* prescriptions are invoked, for example, to ensure flux conservation. Such procedures are not necessary if one works out a theory systematically.

The $\mathbf{k}\cdot\mathbf{p}$ approaches are the most frequently used models for superlattice electronic structure. [Recently Chang (1988) has developed a bond-orbital model that has features in common with both tight-binding and $\mathbf{k}\cdot\mathbf{p}$ models.] They have many advantages. They are relatively simple and easy to implement. Input parameters (typically, momentum matrix elements, zone-center band energies, deformation potentials, etc.) are often well known, and the dependence of the results on these input parameters is usually fairly direct and easy to understand. One disadvantage is that only zone-center states are considered. Therefore superlattices made from indirect band-gap constituent materials are not described, and it is necessary to assume that mixing of bulk states far from the zone center is not important. In principle, a full-zone $\mathbf{k}\cdot\mathbf{p}$ superlattice theory could be formulated. There has been one attempt to construct such a theory (Mailhiot, McGill, and Smith, 1984), but it was not extensively developed.

2. *Ab initio* methods

There have been far fewer *ab initio* studies than empirical studies of superlattice electronic structure. All *ab initio* studies of superlattices have used supercell approaches and are restricted to very-thin-layer superlattices. Baraff, Appelbaum, and Hamann (1977) used a self-consistent pseudopotential boundary-condition approach to study a single interface. Recently, Stiles and Hamann (1988) have developed an *ab initio* boundary-condition approach based on the linearized augmented plane-wave (LAPW) band-structure method and applied it to a single interface, the Si(111) twist boundary. (In principle, it should be possible to generalize this approach to describe superlattice electronic structure.) Many *ab initio* calculations have specifically considered ground-state properties of interfaces rather than electronic structure, which requires a description of excited states. Interface ground-state properties that are particularly interesting for superlattices include valence-band offsets and stability conditions. The *ab initio* methods have not generally been applied to superlattices containing an alloy constituent. Presumably, a virtual-crystal-type approximation would be technically possible in some *ab initio* methods. However, such an approach is in a somewhat different spirit than the *ab initio* calculations.

Self-consistent calculations in a supercell geometry have been used to study the ground-state properties of interfaces. The local approximation to density-functional theory was generally used. Several approaches have been tried. These calculations do not differ substantially from corresponding calculations for a bulk material, except that the number of required basis functions increases rather rapidly with the superlattice period. As a result, calculations have typically been restricted to superlattices with periods of about ten or fewer molecular layers. Differences from bulk electron densities have been found to decay rather rapidly away from the interface, and the thin-layer superlattice geometry appears adequate for investigation of interface properties. Early self-consistent calculations (Baraff, Appelbaum, and Hamann, 1977; Pickett and Cohen, 1978; Pickett, Louie, and Cohen, 1978; Ihm and Cohen, 1979; Ihm, Lam, and Cohen, 1979; Kunc and Martin, 1981) used empirical ion-core pseudopotentials and concentrated on interface charge distributions and valence-band offsets. More recently, *ab initio* pseudopotentials have been used for superlattice-geometry studies of interfaces (Bylander and Kleinman, 1986, 1987a, 1987b; Van de Walle and Martin, 1986a, 1986b, 1987; Batra, Ciraci, and Nelson, 1987; Ciraci and Batra, 1987, 1988; Oshiyama and Saito, 1987; Wood, Wei, and Zunger, 1987, 1988). These calculations concentrated on valence-band offsets and stability conditions for very-thin-layer superlattices. All-electron calculations have been performed using the LAPW (Massidda, Min, and Freeman, 1987) and linear-muffin-tin-orbital (LMTO) methods (Christensen, 1988). The *ab initio* calculations have provided important information that can be used in empirical methods to treat the electronic structure of thicker-layer superlattices. For example, prescriptions to treat the effect of strain (in strained-layer superlattices) and different crystallographic orientation on the valence-band offsets have been provided by *ab initio* calculations.

Ab initio methods have also been applied to calculations of the electronic structure of very-thin-layer superlattices. Empirical methods, which are based on a knowledge of the bulk electronic structure of the constituent materials, become somewhat questionable in dealing with extremely-thin-layer superlattices. This is particularly true for highly strained systems such as Si/Ge. The application of linear elastic continuum theory, like that used to describe strained-layer superlattices in the empirical methods, is not obviously valid in such highly strained cases. The *ab initio* calculations of thin-layer-superlattice electronic structure using the complex unit-cell approach do not differ substantially from corresponding calculations for a bulk material. The *ab initio* electronic-structure calculations were performed using the local-density approximation (LDA). It is well known that the LDA leads to large errors in the band gaps of semiconductors (Perdew and Levy, 1983; Sham and Schlüter, 1983). However, to a large extent, the correct experimental band structure is given if the LDA conduction bands are rigidly shifted to higher energy. In principle, quasiparticle calculations, which require knowledge of the electron self-energy, are necessary to determine the electronic structure (Hybertsen and Louie, 1985, 1986; Godby, Schlüter, and Sham, 1986, 1987). *Ab initio* pseudopotential calculations have been performed for the electronic structure of thin-layer Si/Ge superlattices (Hybertsen and Schlüter, 1987; Ciraci and Batra, 1988; Froyen, Wood, and Zunger, 1988; Satpathy, Martin, and Van de Walle, 1988). In one case (Hybertsen and Schlüter, 1987), full quasiparticle calculations were performed. In the other calculations, the conduction bands were rigidly shifted to higher energy. *Ab initio* calculations of thin-layer GaAs/AlAs electronic structure have been performed using the pseudopotential method (Nakayama and Kamimura, 1985; Bylander and Kleinman, 1986; Nelson, Fong, and Batra, 1987; Taguchi and Ohno, 1988), the LMTO band-structure method (Christensen, Molinari, and Bachelet, 1985), and the augmented spherical-wave method (Eppenga and Schuurmans, 1988).

The *ab initio* methods are much more complex and expensive to implement than empirical methods. To date, *ab initio* methods have been limited to ground-state-interface studies and electronic-structure studies of very-thin-layer superlattices. The ground-state-interface studies have been particularly useful in giving information on valence-band offsets. This information can be usefully applied in empirical electronic-structure methods. *Ab initio* electronic-structure calculations on heavily strained thin-layer Si/Ge superlattices have suggested that empirical methods can adequately describe such systems (Hybertsen and Schlüter, 1987). It was not initially obvious that this was the case.

II. THEORETICAL CONSIDERATIONS FOR BOUNDARY-CONDITION APPROACHES

A. Introduction

In supercell approaches, the superlattice is described by a Hamiltonian with a large unit cell, and the eigenfunctions of the Hamiltonian are found by conventional band-structure methods. These methods are conceptually straightforward. A superlattice is treated the same as any other material. Because the numerical expense increases rapidly with layer thickness, only thin-layer superlattices are generally treated by such methods. In boundary-condition approaches, the eigenfunctions of the superlattice Hamiltonian are found by matching wave functions in each of the constituent materials at the superlattice interfaces. These approaches are not restricted to thin-layer superlattices. They are different in several respects from conventional band-structure calculations. In this section we address a number of theoretical considerations that arise in the application of boundary-condition approaches to superlattice electronic-structure problems.

In order to describe superlattice electronic structure on an appropriate energy scale for the physical phenomena of greatest interest in superlattices, it is necessary to include the spin-orbit interaction and strain interactions in strained-layer superlattices. However, these interactions do not complicate the treatment of the superlattice problem in an essential way. In order to focus on specific features of the superlattice electronic-structure problem, we shall drop the spin-orbit interaction and consider only lattice-matched cases in this section. These interactions will be included in later sections, where examples of calculations are presented. The superlattice will then be described by a one-electron Hamiltonian of the form

$$H=\frac{p^2}{2m}+V_a(\mathbf{r})\theta_a(\mathbf{r})+V_b(\mathbf{r})\theta_b(\mathbf{r}) , \tag{2.1}$$

where V_a (V_b) is the one-electron bulk crystal potential in material a (b) and θ_a (θ_b) is a series of step functions that has the value of unity if $\mathbf{r}$ is in material a (b) and zero otherwise. The potentials in Eq. (2.1) will be viewed as local pseudopotentials. If one of the superlattice constituents is an alloy, it will be described using a virtual-crystal approximation. The symmetries of the two potentials are taken to be the same (e.g., they describe two zinc-blende crystal-structure semiconductors with the same lattice constant).

In the model Hamiltonian of Eq. (2.1), the superlattice interfaces are considered to be abrupt, so that $\mathbf{r}$ is in either material a or material b. The superlattice potential is taken to change abruptly at the interface from one bulk value to the other. On the atomic scale, there is some ambiguity as to the precise location of the superlattice interfaces in this model, which has been used in most superlattice electronic-structure calculations. *Ab initio* calculations, in which the ion cores change on a single atomic plane, have suggested that a rather abrupt change does occur in the self-consistent potential. However, it is unlikely that ion cores actually change on a single atomic plane, over a large lateral distance, in real superlattice samples. Superlattices are seldom so precisely characterized that the extent of interdiffusion at the interfaces is accurately known. It is likely that the extent of interdiffusion in nominally similar samples may vary somewhat. Calculations of the effect of interdiffusion have indicated rather small effects for a grading of one or two atomic layers (Osbourn and Smith, 1979b; Schulman, 1983; Schulman and Chang, 1985b). For these reasons, physically significant improvements to the abrupt interface model represented by Eq. (2.1) will probably be difficult to achieve.

In boundary-condition approaches, eigenstates are found in each constituent material and matched at the superlattice interfaces. Within each constituent, the Hamiltonian has the form

$$H=\frac{p^2}{2m}+V(\mathbf{r}) , \tag{2.2}$$

where $V(\mathbf{r})$ is periodic,

$$V(\mathbf{r})=V(\mathbf{r}+\mathbf{R}_j) , \tag{2.3}$$

for a set of bulk translation vectors $\{\mathbf{R}_j\}$. The translation vectors are the same for the two superlattice constituents. In constructing the superlattice eigenfunction, one matches states with the same energy ε and component of wave vector parallel to the interface, $\mathbf{k}_{\parallel}$. Therefore it is necessary to calculate bulk eigenstates in the constituent materials for fixed ε and $\mathbf{k}_{\parallel}$. Possible values of the wave vector perpendicular to the interfaces, $\mathbf{k}_{\perp}$, must be found. (For notational convenience, we shall use the symbol k, lightface italic, to refer to the normal component of the wave vector and the symbol $\mathbf{k}$, boldface roman, to refer to a three-dimensional wave vector.) Complex values of k, corresponding to evanescent states, are possible. We shall refer to this problem as the complex band-structure problem. To solve this problem, a basis set with Bloch symmetry $\{\Phi_{\alpha\mathbf{k}}(\mathbf{r})\}$ is chosen, and solutions of the equation

$$(H-\varepsilon)\Psi_{d\mathbf{k}}=0 \tag{2.4}$$

are sought by expanding in terms of the basis set:

$$\Psi_{d\mathbf{k}}=\Sigma_\alpha C_{d\alpha}\Phi_{\alpha\mathbf{k}} . \tag{2.5}$$

In the usual band-structure problem, a wave vector $\mathbf{k}$ is input and the energies ε and wave functions $\Psi_{d\mathbf{k}}$ are sought. This problem leads to the usual form of an eigenvalue equation. In the complex band-structure problem, ε and $\mathbf{k}_{\parallel}$ are input and possible values for k and the wave function Ψ_{dk} are sought. This problem does not immediately lead to the usual form of an eigenvalue equation. Depending on the form of the matrix elements

$$\overline{H}_{\alpha\alpha'}(\mathbf{k})=\langle\Phi_{\alpha\mathbf{k}}|H-\varepsilon|\Phi_{\alpha'\mathbf{k}}\rangle , \tag{2.6}$$

it may be possible to cast Eq. (2.4) in the form of an eigenvalue equation. It is necessary to have a numerically efficient method to solve the complex-band-structure problem.

We shall consider three forms for the basis set.

(1) *Plane waves:*

$$\Phi_{\mathbf{G}\mathbf{k}}=\frac{1}{\sqrt{V}}\exp[i(\mathbf{k}+\mathbf{G})\cdot\mathbf{r}] . \tag{2.7}$$

(2) *Zone-center Bloch functions:*

$$\Phi_{b\mathbf{k}}=\frac{1}{\sqrt{N}}\exp(i\mathbf{k}\cdot\mathbf{r})u_b(\mathbf{r}) . \tag{2.8}$$

(3) *Tight-binding functions:*

$$\Phi_{b\mathbf{k}}=\frac{1}{\sqrt{N}}\sum_j\exp(i\mathbf{k}\cdot\mathbf{R}_j)f_b(\mathbf{r}-\mathbf{R}_j-\boldsymbol{\tau}_b) . \tag{2.9}$$

Here, V is the sample volume, N is the number of unit cells in the sample, $\mathbf{G}$ is a reciprocal-lattice vector, and u_b is a zone-center Bloch function, $\boldsymbol{\tau}_b$ specifies an atomic position within the unit cell, and f_b is a local function centered at the atom located at $\boldsymbol{\tau}_b$. The tight-binding basis functions have the property

$$\Phi_{\mathbf{k}+\mathbf{G}}=\Phi_{\mathbf{k}} , \tag{2.10}$$

whereas the plane-wave and zone-center Bloch-function basis functions do not have this property. In the tight-binding basis, the individual Hamiltonian matrix elements satisfy

$$\overline{H}_{\alpha\alpha'}(\mathbf{k}+\mathbf{G})=\overline{H}_{\alpha\alpha'}(\mathbf{k}) , \tag{2.11}$$

whereas, in the plane-wave and zone-center Bloch-function bases, the individual Hamiltonian matrix elements do not satisfy Eq. (2.11). In the plane-wave and zone-center Bloch-function bases, the infinite-dimensional matrices $H(\mathbf{k}+\mathbf{G})$ and $H(\mathbf{k})$ are related by unitary transformation. For example, in the plane-wave basis, $H(\mathbf{k}+\mathbf{G})$ is related to $H(\mathbf{k})$ by a relabeling of rows and columns. Thus the infinite-dimensional matrices $H(\mathbf{k}+\mathbf{G})$ satisfy translation invariance in all three basis sets. However, once the basis sets are truncated to a finite set, $H(\mathbf{k}+\mathbf{G})$ and $H(\mathbf{k})$ are no longer equivalent in the plane-wave and zone-center Bloch-function bases. In the tight-binding basis, $H(\mathbf{k}+\mathbf{G})$ and $H(\mathbf{k})$ are still equivalent after the basis set has been truncated because each individual matrix element satisfies Eq. (2.11). As a result, in the truncated tight-binding basis, the solutions will be periodic,

$$\Psi_{d\mathbf{k}+\mathbf{G}}=\Psi_{d\mathbf{k}} , \tag{2.12}$$

but in the truncated plane-wave and zone-center Bloch-function bases, they will not be periodic. For the usual band-structure problem, this lack of periodicity is not a great problem. Values of $\mathbf{k}$ are fixed in the first Brillouin zone, and a basis is chosen that is large enough that the eigenfunctions are accurately described in the energy range of interest. For the complex band-structure problem, the lack of periodicity causes some difficulties. Values of $\mathbf{k}_{\parallel}$ and ε are fixed and possible values of k are found. In principle, solutions in which k takes on a value such that $\mathbf{k}$ $[=(\mathbf{k}_{\parallel},k)]$ is outside of the Brillouin zone will map onto an equivalent solution inside of the Brillouin zone. However, because of the lack of periodicity, this mapping does not occur in the truncated plane-wave and zone-center Bloch-function bases. As a result, spurious out-of-zone solutions occur in complex band-structure calculations performed in these truncated bases. These spurious solutions have caused considerable confusion in the application of pseudopotential and $\mathbf{k}\cdot\mathbf{p}$ methods (based on plane-wave and zone-center Bloch-functions bases, respectively) to superlattice and interface problems. Similar difficulties occur when one uses other basis sets that do not satisfy Eq. (2.10) and whose Hamiltonian matrix elements therefore do not satisfy Eq. (2.11).

A principal purpose of this section is to resolve these problems.

B. Pseudopotential and k·p methods

In this subsection we consider applications of the pseudopotential method, based on the plane-wave basis set, and of the **k**·**p** method, based on the zone-center Bloch-function basis set. These methods are closely related. We first consider the complex band-structure description of the constituent material, then the interface wave-function matching, and lastly the description of the superlattice. To be specific, we consider zinc-blende-structure materials with a [001] growth axis so that k is in the z direction and $\mathbf{k}_{\|}$ lies in the xy plane.

1. Description of the constituent materials

With the plane-wave basis of Eq. (2.7), the Hamiltonian matrix elements, Eq. (2.6), are

$$\overline{H}_{\mathbf{G}\mathbf{G}'}(\mathbf{k})=\left[\frac{\hbar^2}{2m}|\mathbf{k}+\mathbf{G}|^2-\varepsilon\right]\delta_{\mathbf{G}\mathbf{G}'}+V(\mathbf{G}-\mathbf{G}') , \qquad (2.13)$$

where

$$V(\mathbf{G}-\mathbf{G}')=\frac{1}{\Omega}\int d^3\mathbf{r}\exp[-i(\mathbf{G}-\mathbf{G}')\cdot\mathbf{r}]V(\mathbf{r}) . \qquad (2.14)$$

Here Ω is the volume of the unit cell and the integral in Eq. (2.14) is over the unit cell. The eigenfunctions have the form

$$\Psi_{\mathbf{k}}=\frac{1}{\sqrt{V}}\sum_{\mathbf{G}}C_{\mathbf{G}\mathbf{k}}\exp[i(\mathbf{k}+\mathbf{G})\cdot\mathbf{r}] , \qquad (2.15)$$

where

$$\sum_{\mathbf{G}'}\overline{H}_{\mathbf{G}\mathbf{G}'}C_{\mathbf{G}'\mathbf{k}}=0 . \qquad (2.16)$$

The Hamiltonian matrix elements satisfy

$$\overline{H}_{\mathbf{G}\mathbf{G}'}(\mathbf{k}+\mathbf{G}_1)=\overline{H}_{\mathbf{G}+\mathbf{G}_1;\mathbf{G}'+\mathbf{G}_1}(\mathbf{k}) . \qquad (2.17)$$

If the basis set is not truncated, the expansion coefficients satisfy the periodicity condition

$$C_{\mathbf{G};\mathbf{k}+\mathbf{G}_1}=C_{\mathbf{G}+\mathbf{G}_1;\mathbf{k}} . \qquad (2.18)$$

When the expansion coefficients are solved for a truncated basis, they will not satisfy this periodicity condition. However, if a large enough basis set is chosen so that coefficients for states in the first zone are accurately described, correct out-of-zone states can be constructed using Eq. (2.18). Thus there is no new information in the out-of-zone states. It is possible to formulate a theory based on the truncated basis set, even though periodicity conditions are not satisfied, as long as the basis set is large enough to describe states in the first zone adequately.

The **k**·**p** method, based on the zone-center Bloch-function basis, is related to the pseudopotential method, based on the plane-wave basis, by unitary transformation. In the superlattice problem, two constituent materials must be treated. It is necessary to have a single zone-center basis set to describe the states in both materials. For this reason, we define a reference Hamiltonian by

$$H_R=\frac{p^2}{2m}+\tfrac{1}{2}[V_a(\mathbf{r})+V_b(\mathbf{r})] . \qquad (2.19)$$

The reference Hamiltonian is diagonalized at the zone center in the plane-wave basis to give a set of energies ε_β and cell-periodic eigenfunctions $u_\beta(\mathbf{r})$. We have

$$u_\beta(\mathbf{r})=\frac{1}{\sqrt{\Omega}}\sum_{\mathbf{G}}\mathbf{R}_{\mathbf{G}\beta}\exp(i\mathbf{G}\cdot\mathbf{r}) , \qquad (2.20)$$

where β labels the various eigensolutions and $R_{\mathbf{G}\beta}$ is the unitary transformation matrix between the plane-wave and zone-center Bloch-function bases. In this basis, the Hamiltonian matrix takes the form

$$\overline{H}_{\beta\beta'}(\mathbf{k})=\left[\varepsilon_\beta+\frac{\hbar^2k^2}{2m}-\varepsilon\right]\delta_{\beta\beta'}+\frac{\hbar\mathbf{k}\cdot\mathbf{p}_{\beta\beta'}}{m}+\Delta V_{\beta\beta'} , \qquad (2.21)$$

where

$$\mathbf{p}_{\beta\beta'}=\sum_{\mathbf{G}}(R^+)_{\beta\mathbf{G}}\hbar\mathbf{G}R_{\mathbf{G}\beta'} \qquad (2.22)$$

and

$$\Delta V_{\beta\beta'}=\sum_{\mathbf{G},\mathbf{G}'}(R^+)_{\beta\mathbf{G}}[V(\mathbf{G}-\mathbf{G}')-V_R(\mathbf{G}-\mathbf{G}')]R_{\mathbf{G}'\beta'} . \qquad (2.23)$$

The eigenfunctions have the form

$$\Psi_{\mathbf{k}}=\frac{1}{\sqrt{N}}\sum_{\beta}C_{\beta\mathbf{k}}\exp(i\mathbf{k}\cdot\mathbf{r})u_\beta(\mathbf{r}) , \qquad (2.24)$$

where

$$C_{\beta\mathbf{k}}=\sum_{\mathbf{G}}(R^+)_{\beta\mathbf{G}}C_{\mathbf{G}\mathbf{k}} \qquad (2.25)$$

and satisfies

$$\sum_{\beta'}\overline{H}_{\beta\beta'}(\mathbf{k})C_{\beta';\mathbf{k}}=0 . \qquad (2.26)$$

The periodicity conditions on $C_{\beta\mathbf{k}}$ are found from those of $C_{\mathbf{G}\mathbf{k}}$ and the transformation relating these coefficients,

$$C_{\beta\mathbf{k}+\mathbf{G}_1}=\sum_{\mathbf{G}\beta'}(R^+)_{\beta\mathbf{G}-\mathbf{G}_1}R_{\mathbf{G}\beta'}C_{\beta'\mathbf{k}} . \qquad (2.27)$$

The important advantage of the zone-center Bloch-function basis is its much improved convergence, requiring a much smaller basis set.

In the complex band-structure problem, one fixes $\mathbf{k}_{\|}$ and ε and finds possible values of k. Solutions for k in which **k** lies outside of the Brillouin zone (BZ) are mapped into equivalent solutions in the BZ. It is quite possible that a solution **k** outside the BZ will map into a wave vector $\mathbf{k}'=\mathbf{k}-\mathbf{G}$ where $\mathbf{G}_{\parallel}$ is not zero, so that $\mathbf{k}'_{\parallel}$ and $\mathbf{k}_{\parallel}$ are not equal. It is convenient to define a new zone (call it IZ for interface zone) in order to avoid this possibility. Require that k lie between $\pm\frac{1}{2}G^0_{\perp}$, where $G^0_{\perp}$ is the smallest reciprocal lattice vector along the growth axis, and that $\mathbf{k}_{\parallel}$ lie in the proximity cell of the two-dimensional lattice formed by projecting the three-dimensional reciprocal-lattice points onto the interface plane. For the [001] zinc-blende case, $\mathbf{k}_{\parallel}$ lies in the square formed by bisecting the lines between the origin and the points $\pm 2\pi/a(\hat{\mathbf{x}}+\hat{\mathbf{y}})$ and $\pm 2\pi/a(\hat{\mathbf{x}}-\hat{\mathbf{y}})$ and $-2\pi/a < k \le 2\pi/a$. The volume of the IZ is the same as that of the BZ.

To solve the complex band-structure problem, it is convenient to rewrite Eq. (2.13) in the form

$$\bar{H}_{GG'}(\mathbf{k})=H^2_{GG'}k^2+H^1_{GG'}k+H^0_{GG'} , \tag{2.28}$$

where

$$H^2_{GG'}=\frac{\hbar^2}{2m}\delta_{GG'} , \tag{2.29}$$

$$H^1_{GG'}=\frac{\hbar^2}{m}G_{\perp}\delta_{GG'} , \tag{2.30}$$

and

$$H^0_{GG'}=\left[\frac{\hbar^2}{2m}(k_{\parallel}^2+2\mathbf{k}_{\parallel}\cdot\mathbf{G}_{\parallel}+G^2)-\varepsilon\right]\delta_{GG'}+V(\mathbf{G}-\mathbf{G}') . \tag{2.31}$$

This form explicitly displays the k dependence of H. Transformation to the zone-center Bloch-function basis is straightforward. It is important to notice that this transformation does not depend on k, so that the quadratic dependence on k of Eq. (2.28) is maintained by the transformation. Because of the relatively simple dependence of $H_{GG'}(\mathbf{k})$ on k, Eq. (2.16) can be cast as a linear eigenvalue equation for k (Pendry, 1969; Chang and Schulman, 1982a) by

$$\begin{bmatrix} 0 & 1 \\ -(H^2)^{-1}H^0 & -(H^2)^{-1}H^1 \end{bmatrix}\begin{bmatrix} C \\ kC \end{bmatrix}=k\begin{bmatrix} C \\ kC \end{bmatrix} . \tag{2.32}$$

The matrix in Eq. (2.32) is non-Hermitian. Therefore the eigenvalues can be complex numbers. These complex values correspond to evanescent solutions. The form of Eq. (2.32) is not modified if the transformation to the zone-center Bloch-function basis is made.

Solving the eigenvalue equation (2.32) for fixed $\mathbf{k}_{\parallel}$ and ε determines the possible values of k and the expansion coefficients $C_{G\mathbf{k}}$. It is clear from the form of Eq. (2.32) that solutions for $\mathbf{k}$ will not satisfy periodicity conditions for a finite basis set. In Fig. 2 we show results of a calculation of k for $\mathbf{k}_{\parallel}=0$ at various values of ε in (001) GaAs. A basis set of 113 plane waves was used to construct the zone-center Bloch functions. Fifteen zone-center Bloch functions were used. Hamiltonian matrix elements were found from Eqs. (2.21)–(2.23). (The reference potential was chosen to describe GaAs/AlAs superlattices.) The eigenvalue equation (2.32) was solved to find k for fixed ε. For each value of ε, 30 possible values of k were found. As we shall show below if k is an eigenvalue, k^*, $-k$, and $-k^*$ are also eigenvalues. In the figure only one of this set of eigenvalues is shown. Within the first zone, the dispersion relations are fairly well described. However, for larger values of k, the periodicity conditions fail completely. If a larger basis set is used (calculations were also done with 27 zone-center states), periodicity conditions are maintained to somewhat larger values of k. However, they eventually break down completely. The out-of-zone solutions shown in Fig. 2 are obviously spurious and cannot play any role in an interface theory. We also see evanescent solutions in Fig. 2 with extremely short decay constants. These solutions do not result from truncation of the basis set. Indeed, as the basis set is expanded, even more such solutions occur. However, solutions corresponding to decay lengths much shorter than an atomic radius cannot be considered physically significant and cannot play an important role in an interface theory.

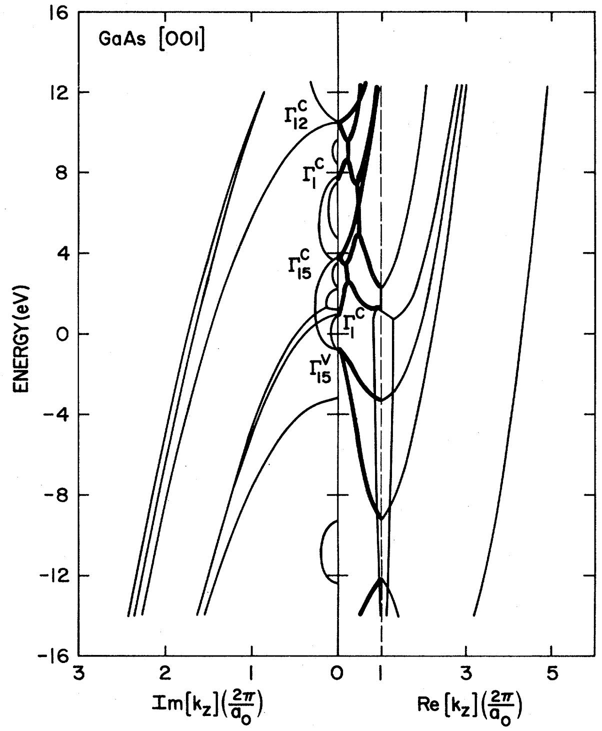

FIG. 2. Complex band structure of GaAs along the [001] direction. The results are for $\mathbf{k}_{\parallel}=0$.

The eigenvalues k and eigenvectors C satisfy Eq. (2.16). Thus the eigenvalues k are determined by

$$\det(H^2k^2+H^1k+H^0)=0 . \tag{2.33}$$

Because the H matrices are Hermitian, if k satisfies Eq. (2.33) so does k^*. We thus have the important result that complex eigenvalues occur in pairs, k and k^*. That is, evanescent states come in growing and decaying pairs with the same real part of k and imaginary parts of k

with opposite signs. The right eigenvector associated with k^* is the conjugate of the left eigenvector associated with k. That is, if the row vector L_j satisfies

$$L_j(H^2k_j^2+H^1k_j+H^0)=0 , \tag{2.34}$$

then taking the Hermitian adjoint gives

$$[H^2(k_j^*)^2+H^1k_j^*+H^0]L_j^+=0 . \tag{2.35}$$

Since C_j^* satisfies this same equation, to within a phase, one has

$$C_{j^*}=L_j^\dagger . \tag{2.36}$$

If the label j refers to the eigenvalue k_j, the label j^* is taken to refer to the eigenvalue $(k_j)^*$ [i.e., $k_j^*\equiv(k_j)^*$].

The fact that if k is an eigenvalue k^* is also an eigenvalue follows from the Hamiltonian's being Hermitian and not from a spatial symmetry. For zinc-blende heterojunctions with a [001] growth direction (and, of course, also for the bulk material), a twofold rotation about the growth axis is a symmetry operator. Calling this operator R and the time-reversal operator T, it is useful to consider the operator RT. When operating on the plane-wave $\exp[i(\mathbf{k}+\mathbf{G})\cdot\mathbf{r}]$, this operator gives $\exp[-i(k^*+G_\perp)\mathbf{z}+i(\mathbf{k}_\parallel+\mathbf{G}_\parallel)\cdot\mathbf{r}_\parallel]$. Notice, in particular, that it does not change $\mathbf{k}_\parallel$. Defining $(-G_\perp,\mathbf{G}_\parallel)$ as $\tilde{\mathbf{G}}$, and using the fact that RT commutes with the Hamiltonian, one finds

$$\begin{aligned}H^2_{\mathbf{G}\mathbf{G}'}k^2+H^1_{\mathbf{G}\mathbf{G}'}k+H^0_{\mathbf{G}\mathbf{G}'}\\ =[H^2_{\tilde{\mathbf{G}}\tilde{\mathbf{G}}'}(-k^*)^2+H^1_{\tilde{\mathbf{G}}\tilde{\mathbf{G}}'}(-k^*)+H^0_{\tilde{\mathbf{G}}\tilde{\mathbf{G}}'}]^* .\end{aligned} \tag{2.37}$$

Since the eigenvalues k can be found by setting the determinant of the matrix in Eq. (2.37) to zero, one sees that if k is an eigenvalue, $-k^*$ must also be an eigenvalue. The eigenvectors associated with the eigenvalues k and $-k^*$ are related (to within a phase) by

$$C_{\mathbf{G}\tilde{\mathbf{k}}}=(C_{\tilde{\mathbf{G}}\mathbf{k}})^* , \tag{2.38a}$$

where

$$\tilde{\mathbf{k}}\equiv(-k^*,\mathbf{k}_\parallel) . \tag{2.38b}$$

Combining with the previous result, we see that, if k is an eigenvalue, k^*, $-k^*$, and $-k$ are also eigenvalues.

Orthogonality and completeness relations for the eigenvalue equation are particularly important in an interface theory. The orthogonality condition is found by considering two eigenvalues k_j and k_i^*, writing the two eigenvector equations, taking the Hermitian adjoint of the second equation, overlapping each equation with the other's eigenvector, and subtracting. This procedure gives

$$(k_j-k_i)\{C_{i^*}^+[H^2(k_i+k_j)+H^1]C_j\}=0 . \tag{2.39}$$

Thus k_j equals k_i, or else the vector product vanishes. If k_j and k_i do not differ by a nonzero $G_\perp$ (that is, if k_j and k_i do not refer to different, but redundant, solutions), the vector product has a simple physical interpretation. It is the z component of the current-density operator averaged over a unit cell,

$$\langle\Psi_{i^*}|J_z(r)|\Psi_j\rangle_A\equiv J_{i^*j}=\frac{1}{\hbar\Omega}C_{i^*}^+[H^2(k_i+k_j)+H^1]C_j , \tag{2.40}$$

where the subscript A indicates an average over a unit cell. It is easy to show that, if the matrix element $\langle\Psi_{i^*}|J_z(r)|\Psi_i\rangle$ is integrated along the interface plane (xy plane), the resulting integral is independent of z. Thus the average in Eq. (2.40) really only has to be over a cross section of the unit cell in the xy plane. If k_j and k_i do differ by a nonzero $G_\perp$, Eq. (2.39) is still valid, but the vector product is not a matrix element of the current-density operator. When an eigenvector is replaced by an equivalent eigenvector, the value of a current-density matrix element does not change.

The derivation of the completeness relations proceeds in the usual way. An arbitrary vector is expanded in terms of the eigenvectors of Eq. (2.32):

$$\begin{bmatrix} S_G \\ (KS)_G \end{bmatrix}=\sum_j B_j\begin{bmatrix} C_{Gj} \\ k_jC_{Gj} \end{bmatrix} . \tag{2.41}$$

The orthogonality relation is used to find B_j in terms of the components of the arbitrary vector. The result is substituted back into Eq. (2.41) and various possibilities for the vector are considered. As a result, one finds that the following relations are satisfied for all $\mathbf{G}$ and $\mathbf{G}'$:

$$0=\sum_{j,G_1}\frac{1}{\hbar\Omega J_{j^*j}}(C_{G_1j^*})^*H^2_{G_1G}C_{G'j} , \tag{2.42}$$

$$0=\sum_{j,G_1}\frac{1}{\hbar\Omega J_{j^*j}}(C_{G_1j^*})^*H^1_{G_1G}C_{G'j} , \tag{2.43}$$

$$0=\sum_{j,G_1}\frac{1}{\hbar\Omega J_{j^*j}}(C_{G_1j^*})^*(k_j^2H^2_{G_1G}+k_jH^1_{G_1G})C_{G'j} , \tag{2.44}$$

and

$$\delta_{GG'}=\sum_{j,G_1}\frac{1}{\hbar\Omega J_{j^*j}}(C_{G_1j^*})^*k_jH^2_{G_1G}C_{G'j} . \tag{2.45}$$

These equations can be interpreted in two ways. If they are viewed as completeness relations for the truncated-basis-set problem, then obviously spurious out-of-zone states (such states are apparent in Fig. 2) must be included in the sum of states labeled by j. Such states are clearly unphysical and cannot play a role in an interface theory. However, these equations can also be viewed as completeness relations for the complete-basis-set problem. In this case, the sum on states must include the repeated-zone solutions. These solutions are redundant but not spurious. They can be constructed from in-zone solutions using periodicity conditions. Viewed in this second way, these equations play an important role in the interface theory.

In earlier work (Mailhiot and Smith, 1986a; Smith and Mailhiot, 1986), we developed a $\mathbf{k}\cdot\mathbf{p}$ theory of superlattices in which four zone-center spatial states were combined with spinors and explicitly treated. Other zone-center spatial states were included in Löwdin perturbation theory. This theory was used to describe superlattice states near the zone center. Within this framework several results similar to those of this section were derived. Spurious out-of-zone solutions could be eliminated from the complex band structure of the constituent materials that appeared in that theory. This was a major simplifying feature of the model. If one wishes to extend the $\mathbf{k}\cdot\mathbf{p}$ theory so as to describe states well away from the zone center, it is necessary to treat a complex band structure of the constituent materials that has the spurious out-of-zone solutions. The interface theory must be formulated so that these spurious out-of-zone solutions do not enter. It is possible to construct such a theory by considering the complete-basis-set problem and using translational symmetry properties to describe the repeated-zone solutions.

2. Interface description

We consider an abrupt interface between two materials labeled a and b. The interface plane is defined by $z=z_0$ and the Hamiltonian is

$$H=H_a\theta(-z+z_0)+H_b\theta(z-z_0)\ , \tag{2.46}$$

where H_a (H_b) is the Hamiltonian in material a (b). The wave function has the form

$$\Psi=\Psi_a\theta(-z+z_0)+\Psi_b\theta(z-z_0)\ , \tag{2.47}$$

where Ψ_a (Ψ_b) is the wave function in a (b). The wave functions Ψ_a,Ψ_b are expanded in terms of bulk eigenstates with fixed $\mathbf{k}_\parallel$ and ε (solutions to the complex band-structure problem)

$$\Psi_a=\sum_j A_j\Psi_j^a=\sum_j A_j\sum_G C^a_{Gj}\exp[i(\mathbf{k}^a_j+\mathbf{G})\cdot\mathbf{r}]\ . \tag{2.48}$$

(In this subsection we consider the plane-wave basis set. Equivalent results can be written in the zone-center Bloch-function basis by unitary transformation.) Only states in the first zone are included in the sum over eigenstates.

The expansion coefficients A_j are determined by the boundary conditions. For a single-interface problem, boundary conditions at $z\pm\infty$ must be specified. Because of the form of the Hamiltonian [Eqs. (2.2) and (2.46)], the wave function and its derivative must be continuous at the interface. Although these conditions are certainly correct, they are awkward to use directly for this problem. It is much more convenient to work in terms of the z component of the current-density operator

$$\begin{aligned}J_z(\mathbf{R})&=\frac{1}{2m}[\delta(\mathbf{r}-\mathbf{R})p_z+p_z\delta(\mathbf{r}-\mathbf{R})]\\&=\frac{1}{2m}\left[2\delta(\mathbf{r}-\mathbf{R})p_z+\left[-i\hbar\frac{\partial}{\partial z}\delta(\mathbf{r}-\mathbf{R})\right]\right]\ .\end{aligned} \tag{2.49}$$

[Altarelli (1983) has also advocated expressing interface matching conditions in terms of the current-density operator.] Because $\delta(\mathbf{r}-\mathbf{R})$ and $\partial\delta(\mathbf{r}-\mathbf{R})/\partial z$ are linearly independent, the interface matching conditions can be written as

$$J_z(x,y,z_0)\Psi_a=J_z(x,y,z_0)\Psi_b\ . \tag{2.50}$$

Equation (2.50) is equivalent to requiring the continuity of the wave function and its derivative, but it is more convenient to use.

We wish to convert Eq. (2.50) into a matrix equation relating the expansion coefficients A_j and B_i defined in Eq. (2.48) and in an analogous equation for material b. To do this, we substitute Eq. (2.48) and its analog into Eq. (2.50), overlap with Ψ^a_{j*}, and average over the xy plane,

$$\begin{aligned}&\sum_{j'}\frac{1}{A}\int dx\,dy\,\langle\Psi^a_{j*}|J_z(x,y,z_0)|\Psi^a_{j'}\rangle A_{j'}\\&\qquad=\sum_i\frac{1}{A}\int dx\,dy\,\langle\Psi^a_{j*}|J_z(x,y,z_0)|\Psi^b_i\rangle B_i\ ,\end{aligned} \tag{2.51}$$

where A is the sample area in the xy plane. Substituting the form of Eq. (2.15) for the bulk eigenstates gives

$$\frac{1}{A}\int dx\,dy\,\langle\Psi^a_{j*}|J_z(x,y,z_0)|\Psi^a_{j'}\rangle=\exp[i(k^a_{j'}-k^a_j)z_0]\sum_{g_\perp}\exp(ig_\perp z_0) \tag{2.52a}$$

$$\times\frac{1}{\hbar\Omega}(C^a_{j*})^+[H^2(k^a_j+k^a_{j'g_\perp})+H^1]C^a_{j'g_\perp}=\delta_{jj'}J^a_{j*j}\ . \tag{2.52b}$$

Here $g_\perp$ is a reciprocal lattice vector normal to the xy plane and $jg_\perp$ refers to a repeated-zone solution ($k_j+g_\perp$). The orthogonality condition for the complex band-structure problem, Eq. (2.39), has been used to deduce Eq. (2.52b). Substituting the form of Eq. (2.15) for the bulk eigenstates also gives

$$\frac{1}{A}\int dx\,dy\,\langle\Psi^a_{j*}|J_z(x,y,z_0)|\Psi^b_i\rangle=\exp[i(k^b_i-k^a_j)z_0]\sum_{g_\perp}\exp(ig_\perp z_0) \tag{2.53a}$$

$$\times\frac{1}{\hbar\Omega}(C^a_{j*})^+[H^2(k^a_j+k^b_{ig_\perp})+H^1]C^b_{ig_\perp}\equiv\exp[i(k^b_i-k^a_j)z_0]J^{ab}_{j*i}(z_0)\ , \tag{2.53b}$$

where Eq. (2.53b) defines $J^{ab}_{j^{*}i}(z_0)$. Thus Eq. (2.50) becomes

$$\exp(ik^a_j z_0)A_j=\frac{1}{J^a_{j^{*}j}}\sum_i J^{ab}_{j^{*}i}(z_0)\exp(ik^b_i z_0)B_i \ . \tag{2.54}$$

In Eq. (2.53a), it is necessary to evaluate a "nonbulk" matrix element of the current-density operator between a wave function in each material. There is no ambiguity in calculating this matrix element because delta functions in the current-density operator restrict the integration to the interface [see Eq. (2.49)], both wave functions are defined at the interface, and they are expressed in the same basis set.

For a [001] superlattice in which the constituent materials do not have a common atom, two physically distinct interfaces can occur. For example, in the InAs/GaSb superlattice, an interface can occur between an In plane and an Sb plane or between a Ga plane and an As plane. The matching conditions will be different for these two distinct interfaces. This difference is described by the phase factor $\exp(ig_\perp z_0)$ in Eqs. (2.53). The possible values of z_0 are different for these two interfaces. (The value of z_0 for a given interface is not arbitrary because a particular origin of coordinates was chosen in the bulk pseudopotential calculations.) In a zone-center interface theory, in which only the $g_\perp=0$ term is retained, the difference between these two interfaces cannot be described.

It is clear that the argument used to give Eq. (2.54) could equally well be applied in a different order to give

$$\exp(ik^b_i z_0)B_i=\frac{1}{J^b_{i^{*}i}}\sum_j J^{ba}_{i^{*}j}(z_0)\exp(ik^a_j z_0)A_i \ . \tag{2.55}$$

For these relations to be consistent, we must have

$$\sum_i \frac{1}{J^a_{j^{*}j}}J^{ab}_{j^{*}i}(z_0)\frac{1}{J^b_{i^{*}i}}J^{ba}_{i^{*}j'}(z_0)=\delta_{jj'} \tag{2.56}$$

and

$$\sum_j \frac{1}{J^b_{i^{*}i}}J^{ba}_{i^{*}j}(z_0)\frac{1}{J^a_{j^{*}j}}J^{ab}_{j^{*}i'}(z_0)=\delta_{ii'} \ . \tag{2.57}$$

These conditions imply flux conservation. To see this, note that flux conservation requires

$$\sum_j (A_{j^{*}})^{*}J^a_{j^{*}j}A_j=\sum_i (B_{i^{*}})^{*}J^b_{i^{*}i}B_i \ . \tag{2.58}$$

Cross terms in Eq. (2.58) do not occur because $j^a_{j^{*}j'}$ vanishes unless $j=j'$. Using Eq. (2.54) to eliminate A_j gives

$$\sum_{i',i,j}(B_{i^{*}})^{*}\exp[i(k^b_{i'}-k^b_i)z_0]J^{ba}_{i^{*}j}(z_0)\frac{1}{J^a_{j^{*}j}}J^{ab}_{j^{*}i'}(z_0)B_{i'}$$
$$=\sum_i (B_{i^{*}})^{*}J^b_{i^{*}i}B_i \ . \tag{2.59}$$

Equation (2.57) then establishes the result. Using Eq. (2.55) to eliminate B_i, Eq. (2.56) will also establish the flux-conservation condition.

From their form, one expects that Eqs. (2.56) and (2.57) should follow from the eigenvalue-equation completeness conditions, Eqs. (2.42)–(2.45). This is indeed the case, as is demonstrated by straightforward calculation. Note that in the sum on eigenstates in Eqs. (2.56) and (2.57) only states in the first zone are included (sums on periodic solutions are explicitly written by the sum over $g_\perp$), whereas in the sums on eigenstates in Eqs. (2.42)–(2.45) periodic solutions are also included. To make the notation consistent one can make the replacements

$$\sum_j \to \sum_j \sum_{g_\perp} \quad \text{and} \quad j\to jg_\perp$$

in Eqs. (2.42)–(2.45).

Transforming to the zone-center Bloch-function basis, the interface wave function has the form of Eq. (2.47) with

$$\Psi_a=\sum_{j,\beta} A_j C^a_{\beta j}\frac{1}{\sqrt{N}}\exp(i\mathbf{k}^a_j\cdot\mathbf{r})u_\beta(\mathbf{r}) \tag{2.60}$$

and

$$\Psi_b=\sum_{i,\beta} B_i C^b_{\beta i}\frac{1}{\sqrt{N}}\exp(i\mathbf{k}^b_i\cdot\mathbf{r})u_\beta(\mathbf{r}) \ . \tag{2.61}$$

Equations (2.61) and (2.62) can be rewritten as

$$\Psi_a=\sum_\beta F^a_\beta(z)\frac{1}{\sqrt{N}}\exp(i\mathbf{k}_\parallel\cdot\mathbf{r}_\parallel)u_\beta(\mathbf{r}) \ , \tag{2.62}$$

where

$$F^a_\beta(z)=\sum_j A_j C^a_{\beta j}\exp(ik^a_j z) \ . \tag{2.63}$$

Here $F^a_\beta(z)$ plays the role of an envelope function modulating the zone-center Bloch functions that satisfy Eq. (2.19). For a full-zone theory, such as we have been discussing, the envelope functions are rapidly varying and we do not expect the boundary conditions to give simple relations for the envelope function. However, for a theory that considers only states near the zone center, all k_j's are small and the envelope functions are slowly varying. Thus for a zone-center theory one might expect that the envelope functions should be approximately continuous and have approximately continuous derivatives. Such boundary conditions, or modifications thereof, have often been used in zone-center theories. To see how such boundary conditions arise, we multiply the matching condition, Eq. (2.54), by $C^a_{\beta j}$, sum on j, and write out the matrix $J^{ab}_{j^{*}i}$ explicitly (for $z_0=0$),

$$\sum_j A_j C^a_{\beta j}=\sum_j \frac{1}{\hbar\Omega J^a_{j^{*}j}}\sum_i \left[\sum_{g_\perp}\sum_{d,d'}(C^a_{d'j^{*}})^{*}C^a_{\beta j}[H^2_{d'd}(k^a_j+k^b_{ig_\perp})+H^1_{d'd}]C^b_{dig_\perp}B_i\right] \ . \tag{2.64}$$

For the general case, this equation does not simplify to anything of interest. But for zone-center theories, the coupling to periodic out-of-zone solutions is small, and only the $g_\perp = 0$ terms need be kept. In this case one can use the completeness relations, Eqs. (2.42)–(2.45), and drop the contribution from periodic solutions, to find

$$\sum_j A_j C^a_{\beta j} = \sum_i B_i C^b_{\beta i} \ . \tag{2.65}$$

Equation (2.65) is the condition for continuity of the envelope function (for $z_0 = 0$). An equation for continuous derivatives of the envelope function can be derived in the same way, with the same limitations, by multiplying the matching condition, Eq. (2.54), by $k^a_j C^a_{\beta j}$ and summing on j.

In previous work (Mailhiot and Smith, 1986a; Smith and Mailhiot, 1986) we considered a zone-center theory and in that context derived results similar to those presented here. The results here are more generally valid in that the envelope functions are not required to be slowly varying. The two results differ because of the contributions from the periodic out-of-zone solutions (sums on $g_\perp$) that appear in the matrix $J^{ab}_{j^* i}$ and in the completeness relations. These terms are small in the zone-center theory. Another difference is that in our previous work, because only four spatial states were explicitly considered, we used Löwdin perturbation theory to include mixing of the higher level states. This led to a different form for the matrices H^i. It also caused the results concerning continuity of the envelope functions to be correct only to zeroth order in the perturbation theory.

3. Superlattice description

For the single-interface problem, the matching conditions of Eq. (2.54) [or, equivalently, Eq. (2.55)] and boundary conditions at $z = \pm\infty$ determine the coefficients A_j and B_i. For the superlattice problem, the wave function is expanded in the form of Eq. (2.47) in each layer, and the matching conditions are imposed at each interface. Because of the superlattice translational symmetry, the superlattice wave function must satisfy

$$\Psi(\mathbf{r}+\mathbf{D}) = \exp(i\mathbf{Q}\cdot\mathbf{D})\Psi(\mathbf{r}) \ , \tag{2.66}$$

where $\mathbf{D}$ is any superlattice translation vector and $\mathbf{Q}$ is the superlattice wave vector. For a superlattice of two zinc-blende-structure materials grown along the [100] axis and having M_a layers of material a and N_b layers of material b, the primitive superlattice translation vectors are

$$\boldsymbol{\alpha} = \begin{cases} (M_a + N_b)\dfrac{a_0}{2}\hat{\mathbf{z}}, & M_a + N_b = \text{even} \ , \\[2ex] (M_a + N_b)\dfrac{a_0}{2}\hat{\mathbf{z}} + \dfrac{a_0}{2}\hat{\mathbf{x}}, & M_a + N_b = \text{odd} \ , \end{cases} \tag{2.67}$$

$$\boldsymbol{\beta} = \frac{a_0}{2}(\hat{\mathbf{x}} + \hat{\mathbf{y}}) \ , \tag{2.68}$$

$$\boldsymbol{\gamma} = \frac{a_0}{2}(\hat{\mathbf{x}} - \hat{\mathbf{y}}) \ , \tag{2.69}$$

where a_0 is the lattice constant.

We expand the superlattice wave function in the nth superlattice cycle, $\Psi_{a,n}$ and $\Psi_{b,n}$, in terms of the eigenstates in the individual materials with a given ε and $\mathbf{k}_\parallel$,

$$\Psi_{a,n} = \sum_j A^n_j \Psi^a_j \ , \tag{2.70}$$

$$\Psi_{b,n} = \sum_i B^n_i \Psi^b_i \ . \tag{2.71}$$

Because of the translational symmetry property of Eq. (2.66), the coefficients can be related by

$$A^n_j = A_j \exp(-ik^a_j z_0)\exp[i(Q - k^a_j)\alpha n] \tag{2.72}$$

and

$$B^n_i = B_i \exp(-ik^b_i z_0)\exp[i(Q - k^b_i)\alpha n] \ , \tag{2.73}$$

where α is the projection of $\boldsymbol{\alpha}$ along the z axis. The matching condition, applied to the interface between materials a and b in the nth superlattice cycle, requires

$$A^n_j \exp[ik^a_j(z_0 + \alpha n)] = \frac{1}{J^a_{j^* j}} \sum_i J^{ab}_{j^* i}(z_0) B^n_i \exp[ik^b_i(z_0 + \alpha n)] \ . \tag{2.74}$$

[Note that $J^{ab}_{j^* i}(z_0 + \alpha n) = J^{ab}_{j^* i}(z_0)$.] Using Eqs. (2.72) and (2.73), we can satisfy all these conditions if

$$A_j = \frac{1}{J^a_{j^* j}} \sum_i J^{ab}_{j^* i}(z_0) B_i \ . \tag{2.75}$$

In the same way, the interface matching condition is applied to the interface between material b in the nth superlattice cycle and material a in the $(n+1)$th cycle:

$$A^{n+1}_j \exp[ik^a_j(z_0 + b + \alpha n)] = \frac{1}{J^a_{j^* j}} \sum_i J^{ab}_{j^* i}(z_0 + b) B^n_i \exp[ik^b_i(z_0 + \alpha n + b)] \ , \tag{2.76}$$

where b is the layer thickness of material b. Using the symmetry conditions, Eqs. (2.72) and (2.73), ensures that Eq. (2.76) is satisfied if

$$A_j \exp[iQ(a+b)]\exp(-ik^a_j a) = \frac{1}{J^a_{j^* j}} \sum_i J^{ab}_{j^* i}(z_0 + b) B_i \exp(ik^b_i b) \ . \tag{2.77}$$

Equations (2.75) and (2.77) specify the expansion coefficients and give possible values for the superlattice wave vector Q. They can be converted into an eigenvalue equation by eliminating B_j in Eq. (2.77):

$$\sum_{j'} M_{jj'} A_{j'} = \exp[iQ(a+b)] A_j \ , \tag{2.78}$$

where

$$M_{jj'}=\sum_i \exp(ik_j^a a)\frac{1}{J^a_{j^*j}}J^{ab}_{j^*i}(z_0+b)$$

$$\times\exp(ik_i^b b)\frac{1}{J^b_{i^*i}}J^{ba}_{i^*j'}(z_0)\ . \tag{2.79}$$

This eigenvalue equation can be solved for the eigenvalue $\exp[iQ(a+b)]$ and the eigenvector A_j. The expansion coefficients in material b are then found by inverting Eq. (2.75). Once these eigenvalues and expansion coefficients have been found, the complete superlattice complex band structure has been determined. Clearly, an equivalent result can be obtained by eliminating A_j.

The coefficients A_j and B_i determine the superlattice wave function, which can be written (for $z_0=0$) as

$$\Psi=\sum_\beta\left[\sum_n\left[\sum_j A_j\exp[i(Q-k_j^a)\alpha n]C^a_{j\beta}\exp(ik_j^a z)\Theta_{an}+\sum_i B_i\exp[i(Q-k_i^b)\alpha n]C^b_{i\beta}\exp(ik_i^b z)\Theta_{bn}\right]\right]\exp(i\mathbf{k}_\parallel\cdot\mathbf{r}_\parallel)u_\beta(\mathbf{r})\ , \tag{2.80}$$

where n labels superlattice cycles and Θ_{an} is equal to unity if $\mathbf{r}$ is in material a in the nth cycle and zero otherwise. Defining the quantity in brackets as $F_\beta(z)$, we can write the superlattice wave function as

$$\Psi=\sum_\beta F_\beta(z)\exp(i\mathbf{k}_\parallel\cdot\mathbf{r}_\parallel)u_\beta\ . \tag{2.81}$$

If one considers only states near the superlattice zone center, the envelope functions $F_\beta(z)$ will be slowly varying on an atomic scale. [For the large terms in Eq. (2.80), k_j^a and k_i^b are near the zinc-blende zone center.] Substituting Eq. (2.81) into the one-electron Schrödinger equation and assuming slowly varying envelope functions gives

$$\sum_{\beta'}\left[\left[\varepsilon_\beta+\frac{\hbar^2k_\parallel^2}{2m}-\varepsilon\right]\delta_{\beta\beta'}+\frac{p_z^2}{2m}+\frac{\hbar\mathbf{k}_\parallel}{m}\cdot\langle u_\beta|\mathbf{p}_\parallel|u_{\beta'}\rangle+\frac{1}{m}\langle u_\beta|p_z|u_{\beta'}\rangle p_z+\Delta V^a_{\beta\beta'}\right]F^a_{\beta'}(z)=0\ , \tag{2.82}$$

where F_β has been written as a piecewise function and F^a_β is the piece in material a. An analogous equation is written for F^b_β. Pieces of the envelope functions in different cycles are related by superlattice periodicity. Equation (2.82) implies that $F_\beta(z)$ and its derivative are continuous at the superlattice interfaces. This conclusion is the same as that drawn using Eq. (2.64) for the zone-center case. The differential equation (2.82) can be solved in each superlattice lattice layer and the envelope functions and their derivatives matched at the interfaces. Some care needs to be used in interpreting equations like Eq. (2.82). They are valid only for slowly varying envelope functions and thus describe only the region near the superlattice zone center. This is often the region of greatest interest, however.

The two-band envelope-function model of Bastard (1981, 1982) follows from a line of reasoning similar to that of Eq. (2.82). The spin-orbit interaction is included. (This just changes the values of ε_β and the momentum matrix elements input to the calculation.) The $\mathbf{k}_\parallel=0$ case is considered and two values for β, describing the conduction- and light-hole bands, are included. Because F is taken to be slowly varying, only the first derivative is kept. In this model F—but not its derivative—is continuous. White and Sham (1981) derived an equivalent model using the complex band-structure expansion method. They made essentially the same approximations as Bastard and arrived at essentially the same conclusions.

Löwdin perturbation theory is often applied to Eq. (2.82) in order to include the effects of bands other than just the lowest conduction band and highest valence bands. It is necessary to do something along these lines if the heavy-hole bands for $\mathbf{k}_\parallel=0$ or any valence bands for $\mathbf{k}_\parallel\neq0$ are to be described, because admixture of higher-lying conduction bands plays an essential role in the description of such states. (In principle, one could include these conduction bands explicitly, of course, but this would lead to a complex multiband problem, which would be difficult to solve numerically.) There are various possible perturbation schemes that can be envisioned. For example, in the multiband envelope-function approach of Altarelli (1983), the $\mathbf{k}\cdot\mathbf{p}$ terms in Eq. (2.82) are treated as the perturbation mixing the higher-lying bands. The mixing is included to first order in the wave functions. Mixing by ΔV is not included. After this state mixing, the equation for the envelope function becomes (Altarelli includes the spin-orbit interaction in his theory, whereas, for illustrative purposes, we have not included it here)

$$\sum_{\beta'}\left[\left[\varepsilon_\beta+\frac{\hbar^2K^2}{2m}-\varepsilon\right]\delta_{\beta\beta'}+\frac{\hbar}{m}\langle u_\beta|\mathbf{K}\cdot\mathbf{p}|u_{\beta'}\rangle+\left[\frac{\hbar}{m}\right]^2\sum_d\frac{\langle u_\beta|\mathbf{K}\cdot\mathbf{p}|u_d\rangle\langle u_d|\mathbf{K}\cdot\mathbf{p}|u_{\beta'}\rangle}{(\varepsilon_\beta+\varepsilon_{\beta'})/2-\varepsilon_d}+\Delta V^a_{\beta\beta'}\right]F^a_{\beta'}(z)=0\ . \tag{2.83}$$

For brevity, we use the notation that $\hbar\mathbf{K}_\parallel=\hbar\mathbf{k}_\parallel$ and $\hbar\mathbf{K}_\perp=p_z$. The sum on β is over the explicitly included zone-center states, and the sum on d includes only the higher-lying states that have not been included in the sum on β. Notice that the first- and second-order momentum matrix elements that appear in Eq. (2.83) are the same in the two materials. Only the ΔV term depends on the material. Because the momentum matrix elements, which multiply p_z operating on $F_{\beta'}$ are the same, F_β and its derivatives are continuous at the superlattice interfaces. The equation that determines the envelope functions is different when Löwdin perturbation theory is used. [That is, Eq. (2.83) is different from Eq. (2.82).] The meaning of the envelope function is also different when Löwdin perturbation theory is used because there are perturbative changes in the zone-center Bloch functions which the envelope function multiplies. When perturbation theory is not used, the superlattice wave function has the form of Eq. (2.62) in material a. When Löwdin perturbation theory, in the form just described, is used, the superlattice wave function in material a has the form

$$\Psi_a=\frac{1}{\sqrt{N}}\exp(i\mathbf{k}_\parallel\cdot\mathbf{r}_\parallel)\sum_\beta\left[F^a_\beta(z)\left[u_\beta+\frac{\hbar}{m}\sum_d\frac{\langle u_\beta|\mathbf{k}_\parallel\cdot\mathbf{p}|u_d\rangle u_d}{\varepsilon_d-\varepsilon_\beta}\right]+\frac{1}{m}\sum_d\frac{\langle u_\beta|p_z|u_d\rangle}{\varepsilon_d-\varepsilon_\beta}(p_zF^a_\beta)u_d\right]\ . \qquad (2.84)$$

One sees that if F_β and its derivative are continuous,the total superlattice wave function will also be continuous.

In our previous work (Smith and Mailhiot, 1986; Mailhiot and Smith, 1986a), we used a somewhat different form of Löwdin perturbation theory. We allowed both the $\mathbf{k}\cdot\mathbf{p}$ terms and ΔV to mix higher bands to first order. That is, these two perturbations were considered to be of the same magnitude and they were treated to the same order. In this case, the equation for the envelope function becomes (we included spin-orbit and strain interactions in our previous work, whereas, for illustrative purposes, we have not included them here)

$$\sum_{\beta'}\left[\left[\varepsilon_\beta+\frac{\hbar^2K^2}{2m}-\varepsilon\right]\delta_{\beta\beta'}+\frac{\hbar}{m}\langle u_\beta|\mathbf{K}\cdot\mathbf{p}|u_{\beta'}\rangle+\sum_d\frac{\left[\Delta V^a_{\beta d}+\frac{\hbar}{m}\langle u_\beta|\mathbf{K}\cdot\mathbf{p}|u_d\rangle\right]\left[\Delta V^a_{d\beta'}+\frac{\hbar}{m}\langle u_d|\mathbf{K}\cdot\mathbf{p}|u_{\beta'}\rangle\right]}{(\varepsilon_\beta+\varepsilon_{\beta'})/2-\varepsilon_d}+\Delta V^a_{\beta\beta'}\right]F^a_{\beta'}(z)=0\ . \qquad (2.85)$$

Notice that the second-order momentum matrix elements (that is, those terms multiplying p_z^2 operating on F_β) are the same in the two materials, but the first-order momentum matrix elements (that is, those terms multiplying p_z operating on F_β) are different in the two materials because of the first-order correction ΔV^a (ΔV^b). As a result neither the envelope functions nor their derivatives are continuous at the interfaces in this theory. The discontinuities are first order in ΔV. (To zeroth order both the envelope functions and their derivatives are continuous in this theory.) Because the envelope functions satisfy somewhat more complex boundary conditions in this theory, we did not explicitly solve Eq. (2.85). Instead we used the complex band-structure expansion approach and solved Eq. (2.78). When this form of Löwdin perturbation theory is used, the superlattice wave function in material a has the form

$$\Psi_a=\frac{1}{\sqrt{N}}\exp(i\mathbf{k}_\parallel\cdot\mathbf{r}_\parallel)\sum_\beta\left[F^a_\beta(z)\left[u_\beta+\sum_d\frac{\langle u_\beta|\Delta V^a+\hbar/m\,\mathbf{k}_\parallel\cdot\mathbf{p}|u_d\rangle u_d}{\varepsilon_d-\varepsilon_\beta}\right]+\frac{1}{m}\sum_d\frac{\langle u_\beta|p_z|u_d\rangle}{\varepsilon_d-\varepsilon_\beta}(p_zF^a_\beta)u_d\right]\ . \qquad (2.86)$$

One sees that F_β and its derivative cannot be continuous, because that would introduce a first-order discontinuity in the total wave function through the term containing ΔV^a.

Envelope-function approaches are appropriate to describe only regions near the superlattice zone center, where the envelope functions are slowly varying compared to the atomic length scale. In principle, one could describe another small region of the superlattice zone by expanding in terms of Bloch functions of the zinc-blende constituents that map into that point of the superlattice zone. However, the zone center is usually the point of greatest interest. The interface matching conditions that the envelope functions satisfy, the differential equation that they solve, and the significance of the envelope functions depend on the order of the perturbation theory used in formulating the envelope-function theory. Often models have been written down in which momentum matrix elements and valence-band parameters are empirically given for the constituent materials. Great care should be used in such cases to ensure that the model can be interpreted within a consistent theoretical framework. For example, if the valence-to-conduction-band momentum matrix element is different in the constituent materials, one must say that the perturbing potential ΔV has been included through at least first order in the wave function. If the second-order valence-band parameters are different in the constituent materials, one must say that the perturbing potential ΔV has been included through at least second order in the wave function. Envelope functions are not continuous if the perturbing potential mixes higher-order bands into the wave function (that is, if it is included to more than zeroth order). Thus models in which momentum matrix elements and second-order valence-band parameters are different in the constituents but that assume that envelope functions are continuous at the interfaces are internally inconsistent. It is important that envelope-function models be based on a consistent perturbation theory.

C. Tight-binding methods

With the tight-binding basis of Eq. (2.9), the Hamiltonian matrix elements, Eq. (2.6), are

$$\bar{H}_{bb'}(\mathbf{k})=\sum_j \exp(i\mathbf{k}\cdot\mathbf{R}_j)\times\langle f_b(\mathbf{r}-\tau_b)|H-\varepsilon|f_{b'}(\mathbf{r}-\mathbf{R}_j-\tau_{b'})\rangle \; . \tag{2.87}$$

It is immediately clear that the individual matrix elements satisfy Eq. (2.11). This form of the Hamiltonian can be related to that used in the plane-wave method, Eq. (2.13), by expanding

$$\Phi_{b\mathbf{k}}=\frac{\exp(i\mathbf{k}\cdot\mathbf{r})}{\sqrt{V}}\sum_{\mathbf{G}}\alpha_b(\mathbf{k}+\mathbf{G})\exp(i\mathbf{G}\cdot\mathbf{r}) \; , \tag{2.88}$$

where

$$\alpha_b(\mathbf{k}+\mathbf{G})=\frac{1}{\sqrt{\Omega}}\int \exp[-i(\mathbf{k}+\mathbf{G})\cdot\mathbf{r}]f_b(\mathbf{r}-\tau_b)d^3\mathbf{r} \; . \tag{2.89}$$

The Hamiltonian then takes the form

$$\bar{H}_{bb'}(\mathbf{k})=\sum_{\mathbf{G},\mathbf{G}'}\alpha_b^*(\mathbf{k}+\mathbf{G})\alpha_{b'}(\mathbf{k}+\mathbf{G}')\bar{H}_{GG'}(\mathbf{k}) \; , \tag{2.90}$$

where $H_{GG'}(\mathbf{k})$ is given by Eq. (2.13). The transformation of Eq. (2.88) appears to play a role similar to that of Eq. (2.20), which relates the plane-wave and zone-center Bloch-function bases. For our purposes, however, there is a major difference between these two transformations. In the transformation of Eq. (2.20), $R_{\mathbf{G}\beta}$ is independent of k, whereas in the transformation of Eq. (2.88), $\alpha_b(\mathbf{k}+\mathbf{G})$ explicitly depends on k. As a result, in the zone-center Bloch-function basis, the Hamiltonian [Eq. (2.21)] maintains the simple quadratic dependence on k. In the tight-binding basis, the Hamiltonian [Eq. (2.90)] has a more complex dependence on k. It is possible to choose explicit forms for the localized functions f_b, evaluate the expansion coefficients [Eq. (2.89)] and Hamiltonian matrix elements [Eq. (2.90)], and solve the usual band-structure problem of fixing $\mathbf{k}$ and finding ε as an eigenvalue. If the localized functions are properly chosen, the results of such a calculation are essentially the same as solving the problem in the plane-wave basis (Chadi, 1977b). A second difference between the transformation of Eq. (2.20) and the transformation of Eq. (2.88) is that Eq. (2.20) is strictly a unitary transformation, whereas there is no way to choose the functions f_b and a finite set of reciprocal-lattice vectors so that Eq. (2.88) is unitary. Therefore it is not immediately obvious that the localized functions can be chosen so that the results of a converged plane-wave calculation are reproduced.

For the complex band-structure problem, the simple quadratic dependence of the Hamiltonian in the plane-wave and zone-center Bloch-function bases allows one to derive an eigenvalue equation [Eq. (2.32)] for k. Solution of this eigenvalue equation provides a numerically efficient method for solving the complex band-structure problem in these basis sets. The more complex functional dependence of Eq. (2.90) on k has thwarted efforts to find a numerically efficient method of solving the complex band-structure problem using this equation. It is conceivable that for a particular form of the f_b functions, such as Slater or Gaussian orbitals, an efficient method could be found. No one has succeeded in doing this, however.

In all applications of tight-binding methods to superlattice electronic structure, the Hamiltonian has been written in the form of Eq. (2.87). A fixed number of local orbitals centered at each atomic position is chosen. The Hamiltonian matrix elements between the local orbitals and the overlap of the local orbitals fall off as the distance increases between the sites at which the orbitals are centered. The sum on j in Eq. (2.87) is truncated to a finite number of nearest neighbors, and the Hamiltonian matrix elements and the overlaps are taken as parameters. The functions f_b are not actually specified. Usually the local functions are assumed orthonormal. In one common tight-binding model for zinc-blende-structure materials (model I), four local functions, one s function and three p functions, are centered at each atom. The functions are taken to be orthonormal, and Hamiltonian matrix elements are included between local functions out to second nearest neighbors. The matrix $H_{bb'}(\mathbf{k})$ is 8×8 in this model if the spin-orbit interaction is ignored and 16×16 if it is included. Neglecting the spin-orbit interaction, there are 18 distinct Hamiltonian matrix elements that enter as empirical parameters. These parameters are usually chosen by fitting the bulk band structure. The spin-orbit interaction adds two more empirical parameters. In a second common tight-binding model for zinc-blende-structure materials (model II), five local functions, two s functions and three p functions, are centered at each atom. The functions are taken to be orthonormal, and Hamiltonian matrix elements are included between local functions out to first nearest neighbors. The matrix $H_{bb'}(\mathbf{k})$ is 10×10 in this model if the spin-orbit interaction is ignored and 20×20 if the spin-orbit interaction is included. Neglecting the spin-orbit interaction, there are 13 distinct Hamiltonian matrix elements that enter as empirical parameters. (Usually, one of these parameters involving the high-energy s functions is set to zero.) The spin-orbit interaction adds two more empirical parameters.

In the complex band-structure problem, $\mathbf{k}_{\parallel}$ and ε are fixed and possible values of k are sought. The possible values of k correspond to solutions of

$$\det|\bar{H}_{bb'}(\mathbf{k})|=0 \; . \tag{2.91}$$

From the functional form of $H_{bb'}(\mathbf{k})$, Eq. (2.87), we see that Eq. (2.91) is a polynomial equation for the variable

$\exp(ikR_0)$, where R_0 is the distance along the growth axis between the nearest planes of atoms. [To be specific, we consider a (001) growth axis. The general case has been discussed by Schulman and Chang (1983).] The order of the polynomial is (nm), where m is the number of parallel planes of atoms normal to the growth axis that interact with a chosen plane of atoms normal to the growth axis (not including the chosen plane itself) and n is the number of orbitals per atom. In model I, without including the spin-orbit interaction, both m and n equal 4. In model II, without including the spin-orbit interaction, m equals 2 and n equals 5. (Note that m is necessarily even.) Including the spin-orbit interaction doubles the value of n. Thus in model I, without spin-orbit coupling, there are 16 possible values of k (32 including spin-orbit coupling), and in model II, without spin-orbit coupling, there are 10 possible values of k (20 including spin-orbit coupling). From Eq. (2.91) and the fact that the Hamiltonian is Hermitian, one see that if k is a solution so is k^*. (This result is general and does not depend either on the basis set chosen or on the material and growth axis considered.) For the particular case of a zinc-blende crystal structure and a (001) growth axis, the symmetry operator RT, where R is a twofold rotation about the growth axis and T is the time-reversal operator (RT commutes with the Hamiltonian and leaves $\mathbf{k}_{\parallel}$ unchanged in this case), ensures that if k is a solution, so is $-k^*$. Thus if k is a solution, k^*, $-k$, and $-k^*$ are also solutions. These conclusions are the same as in the plane-wave basis. Because they follow from the Hamiltonian's being Hermitian and from symmetry considerations, they must not depend on basis set. Because Eq. (2.91) is an equation for $\exp(ikR_0)$, the solutions will satisfy the proper periodicity conditions (i.e., if $\mathbf{k}$ is allowed, $\mathbf{k}+\mathbf{G}$ is also allowed for all reciprocal-lattice vectors $\mathbf{G}$). Unlike the formalism in the plane-wave and zone-center Bloch-function basis sets, no spurious out-of-zone solutions occur. The bulk eigenstates have the form

$$\Psi_{\mathbf{k}} = \sum_b C_b(\mathbf{k}) \Phi_{b\mathbf{k}} \,, \tag{2.92}$$

where $C_b(\mathbf{k})$ satisfies

$$\sum_{b'} \bar{H}_{bb'}(\mathbf{k}) C_{b'}(\mathbf{k}) = 0 \,. \tag{2.93}$$

In the interface problem, the complete wave function is expanded in terms of the local functions

$$\Psi = \sum_{jb} G_{jb} f_{jb} \,, \tag{2.94}$$

where, for notational simplicity, we write f_{jb} for $f_b(\mathbf{r}-\mathbf{R}_j-\tau_b)$ and G_{jb} is an expansion coefficient. The local functions may be different in the two constituent materials. The expansion coefficients must satisfy

$$\sum_{j'b'} \langle f_{jb} | \bar{H} | f_{j'b'} \rangle G_{j'b'} = 0 \tag{2.95}$$

for all j and b. Because of translational symmetry parallel to the interface plane, the matrix elements in Eq. (2.95) do not depend on $\mathbf{R}_{j\parallel}$ and $\mathbf{R}_{j'\parallel}$ separately, but only on the difference, $(\mathbf{R}_{j\parallel}-\mathbf{R}_{j'\parallel})$. As a result Eq. (2.95) simplifies to

$$\sum_{j'_{\perp}b'} \left[\sum_{j'_{\parallel}} \langle f_{j_{\perp}b} | \bar{H} | f_{j'b'} \rangle \exp(i\mathbf{k}_{\parallel}\cdot\mathbf{R}_{j'_{\parallel}}) \right] G_{j'_{\perp}b'} = 0 \,, \tag{2.96}$$

where

$$G_{jb} = \exp(i\mathbf{k}_{\parallel}\cdot\mathbf{R}_{j\parallel}) G_{j_{\perp}b} \,. \tag{2.97}$$

Here we use $j_{\perp}$ and $j_{\parallel}$ to label the perpendicular and parallel components of $\mathbf{R}_j$, respectively. Equation (2.96) must be satisfied for all values of $j_{\perp}$ and b.

Let the interface be between materials $C_{\alpha}A_{\alpha}$ and $C_{\beta}A_{\beta}$ (C_{α} and A_{α} represent the cation and anion of material α). Let the interface occur between an A_{α} atomic layer and a C_{β} atomic layer. [The (001) surface of a zinc-blende material consists of atoms of one type.] In material α, expand the wave function as

$$\begin{aligned}\Psi^{\alpha} &= \sum_l A_l \Psi_l^{\alpha} = \sum_l A_l \left[\sum_b C_{bl}^{\alpha} \Phi_{bl} \right] \\ &= \sum_{jb} \left[\sum_l A_l C_{bl}^{\alpha} \frac{\exp(i\mathbf{k}_l^{\alpha}\cdot\mathbf{R}_j)}{\sqrt{N}} \right] f_{jb} \,,\end{aligned} \tag{2.98}$$

where C_{bl}^{α} satisfies Eq. (2.93) in material α for the wave vector $\mathbf{k}_l^{\alpha}$ and l labels the possible values of k for $\mathbf{k}_{\parallel}$ and ε fixed. An analogous expansion is made in material β. Thus for $j_{\perp}$ in material α, one has

$$G_{j_{\perp}b} = \sum_l A_l C_{bl}^{\alpha} \frac{\exp(ik_l^{\alpha}R_{j\perp})}{\sqrt{N}} \tag{2.99}$$

and an analogous expression for $j_{\perp}$ in material β. Because the C_{bl}^{α} satisfy Eq. (2.93), Eq. (2.96) is satisfied automatically for all values of $j_{\perp}$ corresponding to atomic planes that do not interact with atoms on the other side of the interface. The expansion coefficients A_l and B_m are determined by Eq. (2.96) for values of $j_{\perp}$ corresponding to atomic planes that do interact with atoms on the other side of the interface and by boundary conditions at $z=\pm\infty$. We are assuming that any local function far enough from the interface that it does not interact with functions on the other side of the interface has bulk values for all its Hamiltonian matrix elements. That is, nonbulk Hamiltonian matrix elements between two local functions occur only if both functions interact with local functions on the other side of the interface. If the interface model, which specifies the Hamiltonian matrix elements for the local functions near the interface, does not have this property, it will be necessary to define an "interface region" and solve for coefficients of the local functions in this region explicitly, without reference to the bulk eigenstate expansion coefficients.

The nonbulk Hamiltonian matrix elements that define the interface model in the tight-binding method are not determined by the bulk band-structure fits. In fact, there is no really unambiguous way to determine the values of these parameters within the empirical tight-binding method. In actual calculations, they are often taken to be averages of appropriate bulk matrix elements or as corresponding bulk matrix elements from a material that is not a constituent of the structure. For example, interface matrix elements between local functions centered on In and Sb that appear at the InAs/GaSb interface may be chosen from a bulk band-structure fit of InSb.

Consider, for example, model II without the spin-orbit interaction. There are ten eigenstates in each material (ten possible values of k) and thus twenty expansion coefficients. Half of these coefficients are given by conditions at $z=\pm\infty$ and half are determined by the interface matching conditions. In this case Eq. (2.96) is automatically satisfied for all values of $j_\perp$ except those corresponding to the A_α and C_β atomic planes at the interface. There are five orbitals on each of these two atomic planes. Thus there are ten independent equations from Eq. (2.96) that are not automatically satisfied. These equations provide the ten interface conditions required to determine the coefficients A_l and B_m. Notice that it is not necessary for on-site energies of the interface atoms to equal those of the bulk atoms. The off-diagonal matrix elements between atoms on the two interface planes do not correspond to bulk matrix elements. It is necessary, however, that off-diagonal matrix elements between an interface plane and atoms on the same side of the interface be the same as bulk values.

In many cases, the materials making up the interface have a common atom, such as in the GaAs/AlAs system. Formally, the interface must be chosen between atomic planes so that it lies either between a Ga plane and the central As plane or between an Al plane and the central As plane. That is, the expansion coefficients A_l and B_m are determined by Eq. (2.96) for the central As plane and either the adjacent Ga plane or the adjacent Al plane. This would appear to introduce an asymmetry into the problem. However, it is not necessary to do so. For example, if Eq. (2.96) on the central As plane and the adjacent Al plane is used to determine the expansion coefficients, the Al on-site energies on this plane and the Al-As interactions could, formally, be chosen different from bulk AlAs values. The corresponding Ga on-site energies and Ga-As interactions, however, must be bulk GaAs values. However, no asymmetry is introduced if corresponding bulk values are chosen for all of these matrix elements. (The on-site energies of the central As plane need not be either bulk value.)

The interface conditions resulting from Eq. (2.96) give a linear relation between the expansion coefficients which can be written as

$$\sum_l Z^a_{j_\perp b;l} A_l + \sum_m Z^b_{j_\perp b;m} B_m = 0 \ , \tag{2.100}$$

where

$$Z^a_{j_\perp b;l} = \sum_{j'b'} \langle f_{j_\perp b} | \bar{H} | f_{j'b'} \rangle \frac{\exp(i\mathbf{k}^\alpha_l \cdot \mathbf{R}_{j'})}{\sqrt{N}} C^\alpha_{b'l} \ . \tag{2.101}$$

Here the sum on j' is for $\mathbf{R}_{j'}$ in material α, and there is an analogous result for Z^b. In Eq. (2.100) $j_\perp b$ runs over those orbitals near the interface for which Eq. (2.96) is not automatically satisfied. They take on the same values in Z^a and Z^b. The labels $j_\perp b$, l, and m have the same number of values, so that the Z matrices are square. We can rewrite Eq. (2.100) as

$$A_l = \sum_m W^{ab}_{lm} B_m \ , \tag{2.102}$$

where

$$W^{ab} = -(Z^a)^{-1} Z^b \ . \tag{2.103}$$

Phase factors enter into W^{ab} if the interface does not contain the origin. From the form of Eq. (2.101) we see that if W^{ab} describes an interface that contains the origin and $W^{ab}_{lm}(z_0)$ describes an identical interface at the $z=z_0$ plane, we have

$$W^{ab}_{lm}(z_0) = \exp[i(k^b_m - k^a_l) z_0] W^{ab}_{lm} \ . \tag{2.104}$$

The linear interface relation, Eq. (2.102), in the tight-binding basis has the same structure as the matching condition, Eq. (2.54), in the plane-wave and zone-center Bloch-function bases. Therefore Eq. (2.102) can be used to derive a superlattice eigenvalue equation analogous to Eqs. (2.78) and (2.79). Indeed, the derivation parallels that of Eqs. (2.78) and (2.79) almost exactly. The superlattice wave function is written as a piecewise expansion:

$$\Psi_{\alpha,n} = \sum_l A^n_l \Psi^\alpha_l \ , \tag{2.105}$$

$$\Psi_{\beta,n} = \sum_m B^n_m \Psi^\beta_m \ . \tag{2.106}$$

The superlattice translational symmetry requires that Eq. (2.66) be satisfied. From this symmetry condition one finds that the coefficients A^n_l and B^n_m must satisfy the analogs of Eqs. (2.72) and (2.73). The interface matching condition applied to the interface between materials α and β in the nth superlattice gives the analog of Eq. (2.75). Applying the interface matching condition between material β in the nth superlattice cycle and material α in the $(n+1)$th cycle gives the analog of Eq. (2.77). Combining these results gives the superlattice eigenvalue equation as

$$\sum_{l'} M_{ll'} A_{l'} = \exp[iQ(a+b)] A_l \ , \tag{2.107}$$

where

$$M_{ll'} = \sum_m \exp(ik^\alpha_l a) W^{ab}_{lm} \exp(ik^\beta_m b) W^{ba}_{ml'} \ . \tag{2.108}$$

If the superlattice interface between materials α and β in the nth cycle and between β in the nth cycle and α in the

$(n+1)$th cycle are physically identical, W^{ab} and W^{ba} are inverses of each other [see Eq. (2.103)].

The complex band-structure problem was first solved for a realistic tight-binding model by Osbourn and Smith (1979a), who used the results to describe a single interface. The polynomial equation (2.91) was solved by an energy-scan method. The eigenvectors were then found by solving Eq. (2.93). More recently Chang and Schulman (1982a) derived a more efficient method to solve the complex band-structure problem in the tight-binding basis. They converted Eq. (2.93), with $\mathbf{k}_{\parallel}$ and ε fixed, into an eigenvalue equation with $\exp(ikR_0)$ as the eigenvalue. The eigenvector for this equation gave the expansion coefficients $C_b(\mathbf{k})$. To treat superlattice problems, Schulman and Chang (1981, 1983) and Chang and Schulman (1982b) used a reduced-Hamiltonian method rather than Eqs. (2.107) and (2.108). In this method, values of $\mathbf{k}_{\parallel}$ and ε are chosen and the complex band-structure problem is solved in the constituent materials. The superlattice wave function is expanded as in Eqs. (2.105) and (2.106). A superlattice wave vector is fixed, and the expansion coefficients A_l^n and B_m^n are required to satisfy the analog of Eqs. (2.72) and (2.73). The eigenvalue equation

$$(H-\varepsilon')\Psi=0 \tag{2.109}$$

is projected onto each of the bulk solutions in each constituent material. The resulting algebraic eigenvalue equation is solved for the eigenvalue ε'. The eigenvector gives the expansion coefficients A_l and B_m. (One can also view this as a variational result, where the variation is taken with respect to the expansion coefficients.) Most probably no eigenvalue ε' will agree with the value ε used to construct the bulk constituent-material eigenstates. Therefore the procedure must be iterated until one of the eigenvalues ε' does agree with the input value of ε. Rather good convergence of this iteration procedure has been reported (Schulman and Chang, 1983).

To date, superlattice tight-binding calculations have been performed using the reduced-Hamiltonian method rather than the superlattice eigenvalue equation (2.107). Zone-center Bloch-function calculations have been performed using the superlattice eigenvalue equation (2.78) rather than the reduced-Hamiltonian method. (It is straightforward to derive the analog of the tight-binding reduced-Hamiltonian method in the zone-center Bloch-function basis.) In principle, both methods are valid. The choice between them is a question of numerical efficiency. The superlattice eigenvalue-equation approach has the advantage that iteration is unnecessary. The disadvantage is that the entire superlattice complex band structure must be calculated, even though one is most probably interested only in the real band structure. At a given energy one may well find only evanescent superlattice states in which one is not interested. The reduced-Hamiltonian method has the advantage that only the real superlattice band structure need be calculated. The disadvantage is that an iterative procedure is required.

III. APPLICATIONS TO III-V SEMICONDUCTOR SUPERLATTICES

A. Introduction

In this section we apply a boundary-condition approach to the calculation of the electronic structure and optical properties of semiconductor superlattices. We illustrate these applications using the $\mathbf{k}\cdot\mathbf{p}$ method. In the following section, we compare results obtained by the $\mathbf{k}\cdot\mathbf{p}$ and tight-binding formalisms. We restrict our discussion to semiconductor superlattices grown from III-V zinc-blende-structure compound semiconductors. Semiconductor superlattices are also currently being grown from various II-VI (for a review, see Faurie, Sivananthan, and Reno, 1986), and column IV (People *et al.*, 1984; Bean, 1985) semiconductors.

A central theme in the following discussion is the qualitatively different behavior that can arise in various superlattice systems because of different energy-band lineups, strain conditions, and growth orientations. We compare the electronic structure of type-I and type-II superlattices. The effects of lattice-mismatch-induced strain on the electronic structure of strained-layer superlattices is considered. The case in which the superlattice quantum wells are in biaxial tension is compared with that in which they are in biaxial compression. Until recently, most semiconductor superlattices have been grown along the [001] axis. However, the epitaxial growth of III-V superlattices along other crystallographic axes has recently been demonstrated (Wang, Kuan, and Mendez, 1985; Elcess, Liévin, and Fonstad, 1988; Hayakawa, Takahashi, *et al.*, 1988a, 1988b). Here the electronic structure and optical properties of superlattices grown along the [001] and [111] axes are compared. For lattice-matched superlattices, orientation dependence arises because of anisotropies in properties such as effective masses. For strained-layer superlattices, electric fields are generated in [111]-oriented superlattices, but not in [001]-oriented superlattices, by the piezoelectric effect (Smith, 1986). For very-thin-layer superlattices ($\lesssim 20$ Å), these fields do not significantly change the electronic structure or optical properties. For thick-layer superlattices, however, they are important.

For illustrative purposes, we consider $\mathrm{Ga}_{1-x}\mathrm{In}_x\mathrm{As}/\mathrm{Al}_{1-y}\mathrm{In}_y\mathrm{As}$ as a generic III-V semiconductor superlattice. For the alloy composition $x=0.53$ and $y=0.52$, this superlattice is lattice matched to an InP substrate. It is a type-I superlattice in which the quantum wells for electrons and holes are the $\mathrm{Ga}_{1-x}\mathrm{In}_x\mathrm{As}$ layers and the barriers are the $\mathrm{Al}_{1-y}\mathrm{In}_y\mathrm{As}$ layers. The $\mathrm{Ga}_{1-x}\mathrm{In}_x\mathrm{As}$ layers can be subjected to either tensile or compressive strain by proper choice of the alloy compositions. $\mathrm{Ga}_{1-x}\mathrm{In}_x\mathrm{As}/\mathrm{Al}_{1-y}\mathrm{In}_y\mathrm{As}$ superlattices are currently being epitaxially grown along the [001] orientation at the lattice-matched composition on InP substrates (People *et al.*, 1983; Capasso *et al.*, 1985a, 1985b; Shum *et al.*, 1985; Stolz *et al.*, 1985; Weiner *et al.*, 1985).

We also consider the electronic structure of [001]- and [111]-oriented InAs/GaSb superlattices. This system is a type-II superlattice in which the conduction-band minimum of InAs lies at an energy below the valence-band maximum of GaSb. At small superlattice-layer thicknesses, the electrons are localized within the InAs layers, whereas the holes are localized within the GaSb layers. For thick-layer superlattices, the InAs/GaSb superlattice undergoes a semiconductor-to-semimetal transition, and charge transfer occurs at the superlattice interfaces (Sai-Halasz, Tsu, and Esaki, 1977; Sai-Halasz, Esaki, and Harrison, 1978; Chang *et al.*, 1981). We restrict our discussion to thin layer InAs/GaSb superlattices with semiconducting electronic properties.

The section is organized as follows: In Sec. III.B we consider lattice-matched superlattices and indicate the point-group differences between [001]- and [111]-growth axis superlattices. In Sec. III.C we treat [001]- and [111]-growth-axis strained-layer superlattices in cases in which internal piezoelectric field effects are small. In Sec. III.D we discuss the effects of internal strain-induced piezoelectric fields on the electronic structure of [111]-oriented strained-layer superlattices. Optical properties of semiconductor superlattices are presented in Sec. III.E. Effects of external uniaxial stress are discussed in Sec. III.F.

B. Lattice-matched superlattices

In this section, we discuss the electronic structure of lattice-matched $Ga_{0.47}In_{0.53}As/Al_{0.48}In_{0.52}As$ superlattices grown along the [001] or the [111] axis. We emphasize the differences in electronic structure arising from the different point-group symmetries between [001]- and [111]-growth-axis superlattices.

Figure 3 shows the energy-band diagram of a lattice-matched superlattice consisting of 70 Å of $Ga_{0.47}In_{0.53}As$ (quantum wells) alternating with 30 Å of $Al_{0.48}In_{0.52}As$ (barriers). Since the constituent materials have the same lattice constant, there is no internal strain within the layers and the valence-band maxima of $Ga_{0.47}In_{0.53}As$ and $Al_{0.48}In_{0.52}As$ are each fourfold degenerate. In the absence of strain-induced valence-band splittings, the energy-band diagrams for [001]- and [111]-oriented superlattices are identical. The valence-band offset has a value of 230 meV and is assumed to be independent of growth orientation (Van de Walle and Martin, 1986b).

Figure 4 shows the electronic band structure of a [001]-growth-axis superlattice consisting of 70 Å of $Ga_{0.47}In_{0.53}As$ alternating with 30 Å of $Al_{0.48}In_{0.52}As$. The energy-band diagram of this superlattice is indicated in Fig. 3. Superlattice subband dispersion is shown for superlattice wave vectors both parallel ($Q \sim [001]$) and perpendicular ($k_x \sim [100]$) to the [001] growth axis. Subbands are labeled according to their dominant bulk-state component: conduction (C), heavy-hole (HH), and light-hole (LH). Spin split-off hole (SOH) subbands are not shown here.

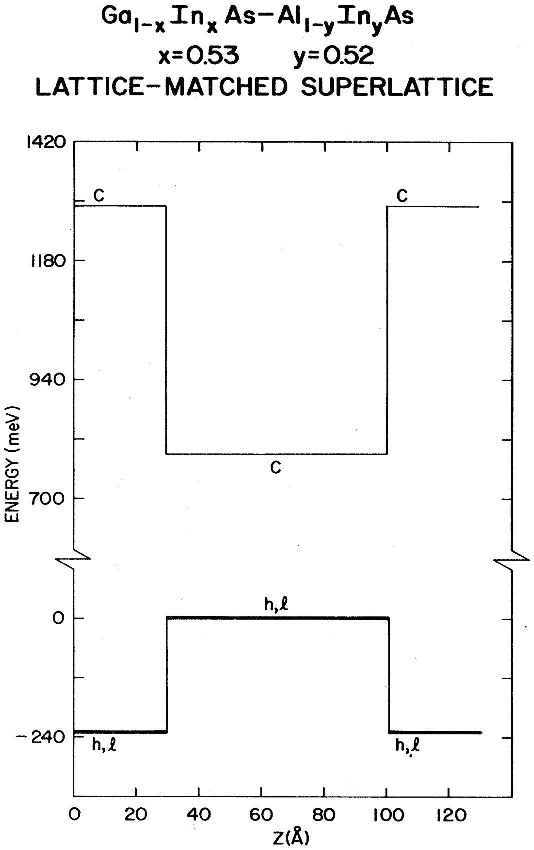

FIG. 3. Energy-band diagram of a lattice-matched superlattice consisting of 70 Å of $Ga_{0.47}In_{0.53}As$ (quantum wells) alternating with 30 Å of $Al_{0.48}In_{0.52}As$ (barriers). The superlattice is lattice matched and, consequently, the energy-band diagrams for [001]- and [111]-oriented superlattices are identical. There is no internal strain within the layers, and therefore the valence-band maxima of $Ga_{0.47}In_{0.53}As$ and $Al_{0.48}In_{0.52}As$ are each fourfold degenerate. The labels *c*, *l*, and *h* identify the conduction, light-hole, and heavy-hole band edges, respectively, at the center of the bulk Brillouin zone. The zero of energy is the valence-band maximum in the $Ga_{0.47}In_{0.53}As$ quantum wells.

In [001]-growth-axis superlattices, the T_d-point-group symmetry associated with bulk zinc-blende-structure compound semiconductors is reduced to D_{2d}. Without the presence of the common anion (As in this case), the bulk T_d point group would be reduced to C_{2v} in the superlattice. The symmetry elements that survive consist of a fourfold rotoinversion axis ($Q \sim [001]$), two twofold rotation axes ($k_x \sim [100]$ and $k_y \sim [010]$), and two mirror planes containing the fourfold axis and bisecting the angles between the twofold axes. There are two twofold irreducible representations of D_{2d} compatible with spin: Γ_6 and Γ_7 (Koster *et al.*, 1963). The odd-numbered conduction-band states ($C_1, C_3, \ldots$), the odd-numbered heavy-hole band states ($HH_1, HH_3, \ldots$), and the even-

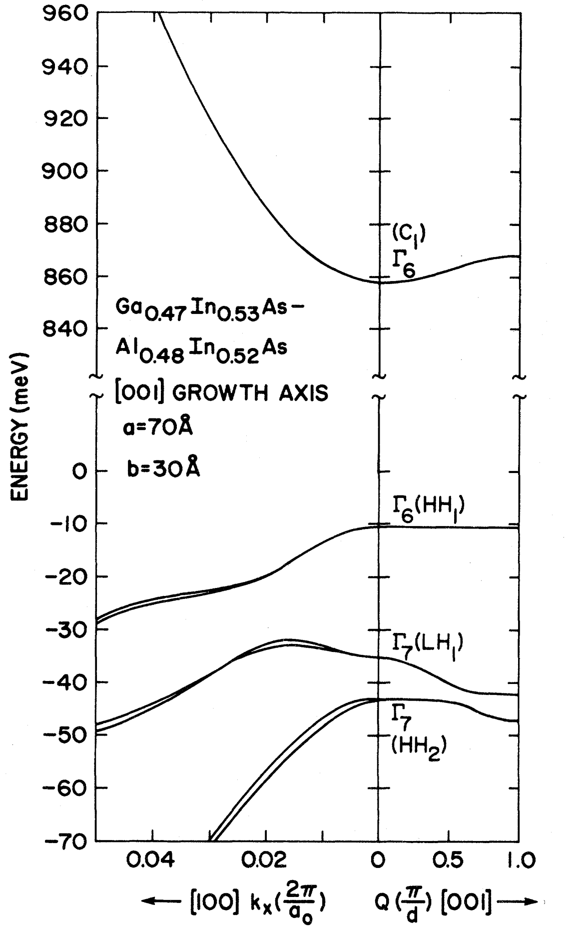

FIG. 4. Electronic energy-band structure of a [001] lattice-matched superlattice consisting of 70 Å of $Ga_{0.47}In_{0.53}As$ alternating with 30 Å of $Al_{0.48}In_{0.52}As$. The energy zero coincides with the valence-band maximum of the bulk $Ga_{0.47}In_{0.53}As$ alloy.

numbered light-hole band states (LH_2,LH_4,. . .) transform like Γ_6, whereas the even-numbered conduction-band states and heavy-hole band states and the odd-numbered light-hole band states transform like Γ_7.

For superlattice wave vectors directed along the [001] growth axis ($\mathbf{k}_{\parallel}=\mathbf{0}$; $Q\neq 0$), the factor group is C_{2v}. The double group contains a single two-dimensional representation: Γ_5 (Koster *et al.*, 1963). Therefore all bands are twofold degenerate, and crossing of superlattice subbands is forbidden along this direction. This symmetry-induced anticrossing behavior along the [001] growth axis is clearly shown in Fig. 4 for the hole subbands LH_1 and HH_2. The results of Fig. 4 are are calculated in a **k**·**p** model that includes mixing of zone-center states by ΔV through first order in Löwdin perturbation theory. In **k**·**p** models in which the zone-center states in the two constituent materials are assumed to be the same, the bands LH_1 and HH_2 would cross.

When the superlattice wave vector lies in the plane of the interface along one of the twofold axes, the factor group is reduced to C_2. The group C_2 contains two one-dimensional representations compatible with spin: Γ_3 and Γ_4 (Koster *et al.*, 1963). Subband crossing is allowed in this direction for superlattice subbands belonging to different irreducible representations. For $\mathbf{k}_{\parallel}$ in the [110] and [1$\bar{1}$0] directions, the factor group is C_s. For $\mathbf{k}_{\parallel}$ in other directions, all spatial symmetry is lost. The lack of inversion symmetry in [001]-growth-axis superlattices made from zinc-blende-structure compound semiconductors produces a splitting of the Kramers doublet throughout the superlattice Brillouin zone, except along the [001] growth axis. This splitting is proportional to the second-order matrix element coupling the *s* state of the conduction-band minimum to the *p* states of the valence-band maximum. If such a matrix element were zero, as is the case for diamond-structure semiconductors with a center of inversion, a twofold Kramers degeneracy would exist throughout the superlattice Brillouin zone by a combination of time-reversal and inversion symmetries.

Figure 5 shows subband dispersions for a [111]-

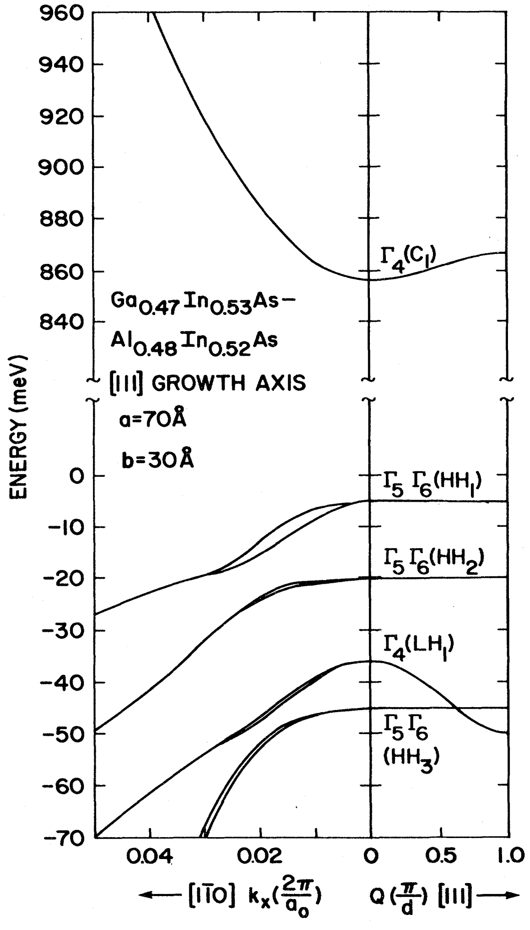

FIG. 5. Electronic energy-band structure of a [111] lattice-matched superlattice consisting of 70 Å of $Ga_{0.47}In_{0.53}As$ alternating with 30 Å of $Al_{0.48}In_{0.52}As$. The energy zero coincides with the valence-band maximum of the bulk $Ga_{0.47}In_{0.53}As$ alloy.

growth-axis superlattice consisting of 70 Å of $Ga_{0.47}In_{0.53}As$ alternating with 30 Å of $Al_{0.48}In_{0.52}As$. The energy-band diagram of this superlattice is the same as that for the [001] superlattice and is shown in Fig. 3. We consider superlattice wave vectors with components parallel ($Q \sim [111]$) and perpendicular ($k_x \sim [1\bar{1}0]$) to the [111] growth direction.

When superlattices consisting of zinc-blende-structure compound semiconductors are grown along the [111] axis, the bulk T_d-point-group symmetry is reduced to C_{3v}. Thus, for [111]-growth-axis superlattices, the symmetry elements that persist are a threefold rotation axis ($Q \sim [111]$), a mirror plane containing the threefold axis and perpendicular to the $[1\bar{1}0]$ direction ($k_x \sim [1\bar{1}0]$), and two other mirror planes generated by the rotation acting on the first mirror plane. There are three irreducible representations of C_{3v} compatible with spin: Γ_4, Γ_5, and Γ_6 (Koster *et al.*, 1963). The irreducible Γ_4 representation is twofold degenerate, whereas Γ_5 and Γ_6 are one dimensional. At the zone center, Γ_5 and Γ_6 are degenerate by time reversal. The conduction-band states ($C_1, C_2, C_3, \ldots$) and light-hole states ($LH_1, LH_2, LH_3, \ldots$) transform like Γ_4, and the heavy-hole states ($HH_1, HH_2, HH_3, \ldots$) transform like (Γ_5, Γ_6).

For superlattice wave vectors directed along the [111] growth axis ($\mathbf{k}_\parallel = \mathbf{0}; Q \neq 0$), the factor group remains the entire C_{3v} point group. While time-reversal symmetry requires that the one-dimensional irreducible representations Γ_5 and Γ_6 be degenerate at the center of the superlattice Brillouin zone ($\mathbf{k}_\parallel = \mathbf{0}$; $Q = 0$), these states should in principle split away from the center of the Brillouin zone. However, the interactions that lead to this splitting, **k**-dependent spin-orbit interactions, are very small. We have not included these very small terms in the calculation (although it is easy to do so), and therefore the Γ_5 and Γ_6 bands do not split away from $Q = 0$ in the calculation. States belonging to the two-dimensional irreducible representation Γ_4 do not mix with those belonging to the (Γ_5, Γ_6) irreducible representations, and crossing is allowed for superlattice wave vectors along the [111] growth axis. Such a crossing behavior is reproduced by the $\mathbf{k}\cdot\mathbf{p}$ model, as is evident in Fig. 5 for the case of the hole subbands HH_3 and LH_1.

When the superlattice wave vector lies in the plane of the interface and is in one of the mirror planes ($\mathbf{k}_\parallel \sim [112]$, [121], or [211] and $Q = 0$), the factor group is C_s. The group C_s contains two nondegenerate representations compatible with spin. Subband crossing is allowed in these directions for superlattice subbands belonging to different representations. For other directions of $\mathbf{k}_\parallel$, all spatial symmetry is lost. In all cases with $k_\parallel \neq \mathbf{0}$, the subbands are nondegenerate.

Comparing Figs. 4 and 5, one sees many similarities. The conduction and light-hole subbands have very nearly the same zone-center energies for the two growth directions. However, the zone-center energies of the heavy-hole bands are significantly higher for the [111]-growth-axis material. That is, the quantum confinement energy is much less for heavy holes in [111]-growth-axis material than for [001]-growth-axis material. These results occur because the electron and light-hole effective masses in zinc-blende materials are nearly isotropic, whereas the heavy-hole effective mass is larger in the [111] direction than the [001] direction. The electron dispersion is very similar for the two growth-direction materials. Hole dispersion in $\mathbf{k}_\parallel$ directions are not similar. Light-hole dispersion along the growth axis ($Q \neq 0$) is similar for the two growth-axis materials except for cases in which the light- and heavy-band energies become close and the bands mix and repel each other for [001]-growth-axis material but do not mix and cross each other for [111]-growth-axis material.

We now discuss the character of the superlattice wave functions at the center of the Brillouin zone ($\mathbf{k}_\parallel = \mathbf{0}$; $Q = 0$). At the center of the superlattice Brillouin zone, the factor group is equivalent to the entire superlattice point group. We consider, in turn, [001]- and [111]-growth-axis superlattices, and we illustrate our discussion by focusing on the first and second light-hole subbands (LH_1 and LH_2).

In the case of superlattices grown along a [001] axis and having a common anion, the point group is D_{2d}, which contains two two-dimensional irreducible representations compatible with spin: Γ_6 and Γ_7. From the zinc-blende periodic basis functions $|s\rangle$, $|x\rangle$, $|y\rangle$, $|z\rangle$ and the two-component spinor ($\uparrow, \downarrow$), we construct basis functions transforming according to these irreducible representations:

$$u({}^1\Gamma_6^{1/2}) = |s\uparrow\rangle , \tag{3.1a}$$

$$u({}^1\Gamma_6^{-1/2}) = |s\downarrow\rangle , \tag{3.1b}$$

$$u({}^2\Gamma_6^{1/2}) = |i(x - iy)\downarrow\rangle/\sqrt{2} , \tag{3.1c}$$

$$u({}^2\Gamma_6^{-1/2}) = |i(x + iy)\uparrow\rangle/\sqrt{2} , \tag{3.1d}$$

$$u({}^1\Gamma_7^{1/2}) = |z\uparrow\rangle , \tag{3.1e}$$

$$u({}^1\Gamma_7^{-1/2}) = |z\downarrow\rangle , \tag{3.1f}$$

$$u({}^2\Gamma_7^{1/2}) = |(x + iy)\downarrow\rangle/\sqrt{2} , \tag{3.1g}$$

$$u({}^2\Gamma_7^{-1/2}) = |-(x - iy)\uparrow\rangle/\sqrt{2} , \tag{3.1h}$$

where $x \sim [100]$, $y \sim [010]$, and z is along the [001] growth axis.

The symmetry point group of superlattices grown along the [111] axis is C_{3v}. The point group C_{3v} contains three irreducible representations compatible with spin. One of the irreducible representations is two dimensional (Γ_4), whereas the other two are one dimensional (Γ_5, Γ_6). In constructing basis functions transforming according to these irreducible representations, it is convenient to define mutually orthogonal functions referenced with respect to the [111] growth axis:

$$|\Phi_1\rangle \equiv \frac{1}{(2)^{1/2}}(|x\rangle - |y\rangle)\ , \qquad (3.2a)$$

$$|\Phi_2\rangle \equiv \frac{1}{(6)^{1/2}}(|x\rangle + |y\rangle - 2|z\rangle)\ , \qquad (3.2b)$$

$$|\Phi_3\rangle \equiv \frac{1}{(3)^{1/2}}(|x\rangle + |y\rangle + |z\rangle)\ , \qquad (3.2c)$$

where $|x\rangle$, $|y\rangle$, and $|z\rangle$ are oriented along the axes [100], [010], and [001], respectively. The functions $|\Phi_1\rangle$, $|\Phi_2\rangle$, $|\Phi_3\rangle$ are oriented along the axes [110], [112], and [111], respectively. We quantize spin along [111]. Spins quantized along the [111] direction are related to those quantized along the [001] axis by the spin-$\frac{1}{2}$ transformation matrix. With the above transformations, we construct basis functions transforming according to the Γ_4, Γ_5, and Γ_6 irreducible representations of the C_{3v} point group:

$$u({}^1\Gamma_4^{1/2}) = |s\uparrow\rangle\ , \qquad (3.3a)$$

$$u({}^1\Gamma_4^{-1/2}) = |s\downarrow\rangle\ , \qquad (3.3b)$$

$$u({}^2\Gamma_4^{1/2}) = |(\Phi_1 + i\Phi_2)\downarrow\rangle/\sqrt{2}\ , \qquad (3.3c)$$

$$u({}^2\Gamma_4^{-1/2}) = |-(\Phi_1 - i\Phi_2)\uparrow\rangle/\sqrt{2}\ , \qquad (3.3d)$$

$$u({}^3\Gamma_4^{1/2}) = |\Phi_3\uparrow\rangle\ , \qquad (3.3e)$$

$$u({}^3\Gamma_4^{-1/2}) = |\Phi_3\downarrow\rangle\ , \qquad (3.3f)$$

$$u(\Gamma_5) = (|(\Phi_1 + i\Phi_2)\uparrow\rangle + |(\Phi_1 - i\Phi_2)\downarrow\rangle)/2\ , \qquad (3.3g)$$

$$u(\Gamma_6) = (|(\Phi_1 + i\Phi_2)\uparrow\rangle - |(\Phi_1 - i\Phi_2)\downarrow\rangle)/2\ , \qquad (3.3h)$$

where $\uparrow \equiv \uparrow_{111}$ and $\downarrow \equiv \downarrow_{111}$.

The superlattice wave functions can be written as

$$\Psi_{Q\alpha}(\mathbf{r}) = \frac{1}{\sqrt{N}}\exp(i\mathbf{Q}\cdot\mathbf{r})\sum_{\beta}\sqrt{l}F_{\beta}^{Q\alpha}(z)u_{\beta}(\mathbf{r})\ , \qquad (3.4)$$

where $Q = \mathbf{k}_{\parallel} + \hat{\mathbf{z}}Q$ is the superlattice wave vector, α is a set of quantum numbers labeling the superlattice solutions, N is the number of superlattice unit cells, l is the length of a zinc-blende unit cell in the growth direction, and $u_\beta(\mathbf{r})$ are the zinc-blende periodic basis functions. The envelope functions $F(z)$ are functions of distance along the growth axis (z) alone because of $\mathbf{k}_{\parallel}$ conservation at the interfaces. They are superlattice periodic functions. Wave-function normalization requires

$$\sum_{d}\int_{-b}^{a}|F_d(z)|^2 dz = 1\ , \qquad (3.5)$$

where only the eight explicitly included states are kept in the sum and the integration is across one superlattice unit cell along the growth direction. The superlattice period is $(a+b)$.

At the zone center, the superlattice wave function transforms like one of the irreducible representations of the superlattice point group that is compatible with spin. The zinc-blende periodic functions $u_\beta(\mathbf{r})$ can be written as basis functions of these representations. The envelope functions $F_\beta(\mathbf{z})$ are functions of z alone. For the D_{2d} point group of a [001]-growth-axis superlattice, a function of z alone can only transform like Γ_1 or Γ_4. The envelope function $F(z)$ is an even function of z through the center of each material layer if it transforms like Γ_1 and an odd function of z through the center of each material layer if it transforms like Γ_4. Superlattice translational symmetry ensures that if a function of z is even (odd) through the center of one material layer, it is even (odd) through the center of the other. Since the direct product of Γ_1 with Γ_6 (Γ_7) is Γ_6 (Γ_7) and the direct product of Γ_4 with Γ_6 (Γ_7) is Γ_7 (Γ_6), a zone-center [001]-superlattice wave function that transforms like Γ_6 will contain a sum of terms consisting of a Γ_1 envelope function times a Γ_6 zinc-blende periodic function and a Γ_4 envelope function times a Γ_7 zinc-blende periodic function, that is,

$$\Psi_{\Gamma_6}^{[001]} = \sum F_{\Gamma_1}u_{\Gamma_6} + \sum F_{\Gamma_4}u_{\Gamma_7}\ . \qquad (3.6a)$$

Likewise, a zone-center [001]-superlattice wave function that transforms like Γ_7 will contain a sum of terms consisting of a Γ_1 envelope function times a Γ_7 zinc-blende periodic function and a Γ_4 envelope functions times a Γ_6 zinc-blende periodic function, that is,

$$\Psi_{\Gamma_7}^{[001]} = \sum F_{\Gamma_1}u_{\Gamma_7} + \sum F_{\Gamma_4}u_{\Gamma_6}\ . \qquad (3.6b)$$

The two-dimensional representations Γ_6 and Γ_7 can be chosen so that pairs of basis functions can be labeled "spin-up" and "spin-down" and the Clebsch-Gordan coefficients for the direct products in Eq. (3.6) do not mix these labels.

For the C_{3v} point group of a [111] superlattice, any function of z transforms like Γ_1. (The symmetry operators of C_{3v} do not change z.) Therefore a zone-center [111]-superlattice wave function that transforms like Γ_4 (Γ_5 or Γ_6) will contain a sum of terms consisting of an envelope function that transforms like Γ_1 times a zinc-blende periodic function that transforms like Γ_4 (Γ_5 or Γ_6), that is,

$$\Psi_{\Gamma_i}^{[111]} = \sum F_{\Gamma_1}u_{\Gamma_i}\quad (i = 4,\ 5,\ \text{or}\ 6)\ . \qquad (3.7)$$

The two-dimensional representation can be chosen so that pairs of basis functions can be labeled spin-up and spin-down and the sum in Eq. (3.7) will not mix these labels (for $i = 4$).

In Fig. 6 we show the envelope functions multiplying the four explicitly included spin-up basis states for the spin-up LH$_1$ and LH$_2$ hole subband zone-center states for the [001]-growth-axis superlattice whose dispersion curves are indicated in Fig. 4. The LH$_1$ state transforms like Γ_7. The large-amplitude envelope functions that multiply the zinc-blende periodic functions ${}^1\Gamma_7(z\uparrow)$ and ${}^2\Gamma_7[(x+iy)\downarrow]$ are even (transform like Γ_1). The ${}^1\Gamma_7$ and ${}^2\Gamma_7$ periodic functions combine to make up the $k_z \to 0$ light-hole (and split-off hole) states in the bulk material. The smaller-amplitude envelope functions that multiply the zinc-blende periodic functions ${}^1\Gamma_6(s\uparrow)$ and ${}^2\Gamma_6[i(x-iy)\downarrow]$ are odd (transform like Γ_4). The ${}^1\Gamma_6$ and

${}^2\Gamma_6$ periodic functions make up the $k_z \rightarrow 0$ conduction and heavy-hole bands, respectively. The inclusion of the ${}^2\Gamma_6$ periodic-function component in LH_1 is a consequence of the heavy-hole and light-hole mixing that results from the mixing of the zone-center states by $\Delta V^{(i)}(\mathbf{x})$. It is the same interaction that causes the mixing of the LH_1 and HH_2 bands evident in Fig. 4. The LH_2 state transforms like Γ_6. The large-amplitude envelope functions that multiply the ${}^1\Gamma_7$ and ${}^2\Gamma_7$ zinc-blende periodic functions are odd. The small-amplitude envelope functions that multiply the ${}^1\Gamma_6$ and ${}^2\Gamma_6$ zinc-blende periodic functions are even. The inclusion of the periodic ${}^2\Gamma_6$ function components is, again, an example of heavy-hole and light-hole mixing.

In Fig. 7 we show the envelope functions multiplying the explicitly included spin-up Γ_4 basis states for the spin-up LH_1 and LH_2 hole subband zone-center states for the [111]-growth-axis superlattice whose dispersion curves are indicated in Fig. 5. We first notice that there are no Γ_5 or Γ_6 zinc-blende periodic functions mixed into the LH_1 and LH_2 states for the [111] superlattice. The envelope function must transform like Γ_1 for [111] superlattices and therefore cannot mix Γ_5 or Γ_6 periodic functions into a Γ_4 state. The Γ_5 and Γ_6 periodic functions make up the $k_z \rightarrow 0$ heavy-hole states in the bulk material. The nonmixing of these functions into the LH_1 and LH_2 states seen in Fig. 7 corresponds to the nonmixing and band crossing of the LH_1 and HH_3 seen in the dispersion curves of Fig. 5. The ${}^1\Gamma_4$ function of the [111] superlattice is analogous to the ${}^1\Gamma_6$ function of the [001] superlattice, the ${}^2\Gamma_4$ function is analogous to the ${}^2\Gamma_7$

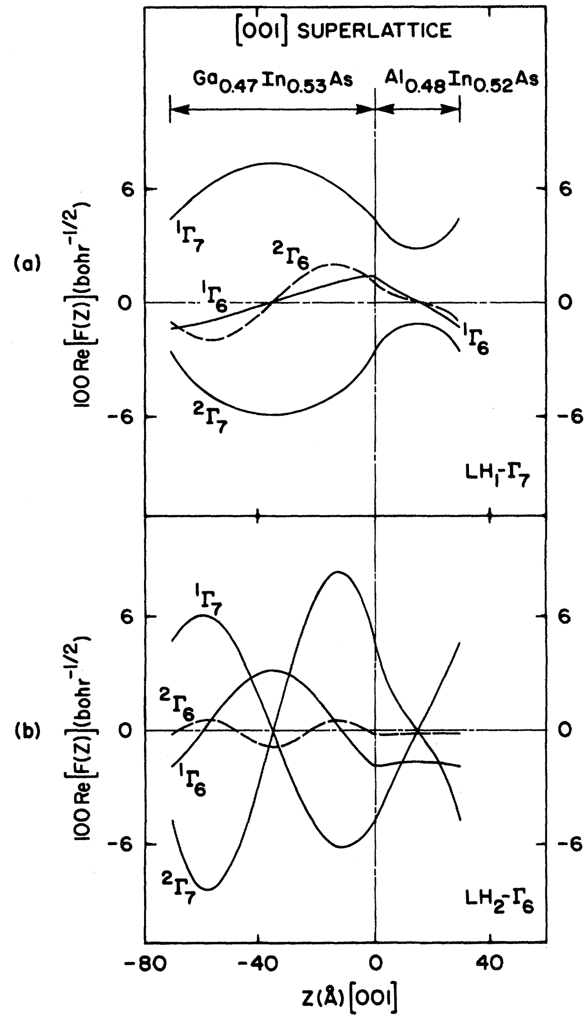

FIG. 6. Symmetry-resolved light-hole envelope functions for a [001]-growth-axis superlattice consisting of 70 Å of $\mathrm{Ga}_{0.47}\mathrm{In}_{0.53}\mathrm{As}$ alternating with 30 Å of $\mathrm{Al}_{0.48}\mathrm{In}_{0.52}\mathrm{As}$: (a) first light-hole state, LH_1; (b) second light-hole state, LH_2. The energy-band structure of this superlattice is shown in Fig. 4. The spin-up component (quantized along the [001] growth axis) is shown. Wave function symmetries are defined in the text.

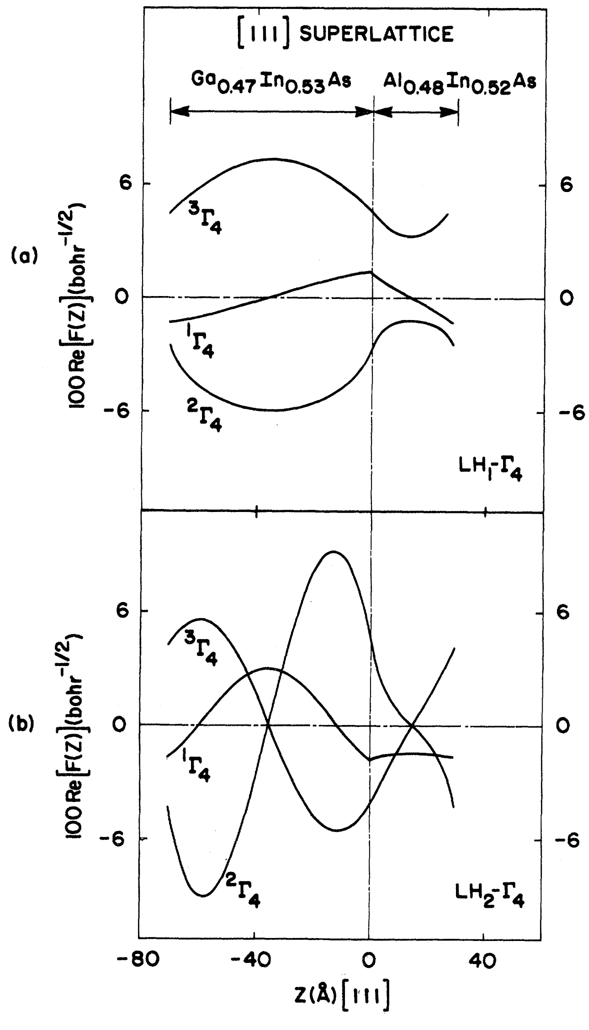

FIG. 7. Symmetry-resolved light-hole envelope functions for a [111]-growth-axis superlattice consisting of 70 Å of $\mathrm{Ga}_{0.47}\mathrm{In}_{0.53}\mathrm{As}$ alternating with 30 Å of $\mathrm{Al}_{0.48}\mathrm{In}_{0.52}\mathrm{As}$: (a) first light-hole state, LH_1; (b) second light-hole state, LH_2. The energy-band structure of this superlattice is shown in Fig. 5. The spin-up component (quantized along the [111] growth axis) is shown. Wave function symmetries are defined in the text.

function, and the $^3\Gamma_4$ function is analogous to the $^1\Gamma_7$ function. From symmetry there are no restrictions on the envelope functions of the [111] superlattice other than that they have superlattice periodicity. However, by comparing Figs. 6 and 7, we see a very close correspondence between analogous envelope functions for the two cases.

We now analyze the electronic structure of [001]- and [111]-oriented InAs/GaSb superlattices. This system is a type-II superlattice in which the conduction-band minimum of InAs lies at an energy below the valence-band maximum of GaSb. At small superlattice layer thicknesses, the electrons are localized within the InAs layers, whereas the holes are localized within the GaSb layers. For thick-layer superlattices, the InAs/GaSb superlattice undergoes a semiconductor-to-semimetal transition, and charge transfer occurs at the superlattice interfaces.

The InAs/GaSb superlattice has a lattice mismatch on the order of $[\Delta a_0/a_0]\approx 0.6\%$. Here we consider the electronic structure of thin-layer superlattices in the semiconductor regime, where internal strain-induced piezoelectric fields are not important and we have neglected their effects in the analysis presented below. We have, however, included the effects of lattice-mismatch-induced internal strains through deformation potential effects. We present our analysis of InAs/GaSb superlattices in the section treating lattice-matched superlattices because of the small differences of lattice constants.

Figure 8 shows the energy-band diagram of a superlattice consisting of $M_a=8$ layers of InAs alternating with $N_b=8$ layers of GaSb. Results are indicated for a [001]-oriented superlattice in Fig. 8(a) and for a [111]-oriented superlattice in Fig. 8(b). There is a very small difference in the two energy-band diagrams because of anisotropy in the strain splittings. The calculated electronic band structures of these superlattices are shown in Figs. 9 and 10, respectively. The energy separation between the valence-band maximum of GaSb and the conduction-band minimum of InAs is 110 meV and is assumed to be independent of growth orientation. Internal strains present within the layers lead to splittings of the valence-band maximum due to deformation-potential effects. These deformation-potential effects depend on the growth orientation, since the strain Hamiltonian depends on the growth orientation. The InAs layers are under biaxial tension, and the light-hole states are split up from the heavy-hole states at the center of the bulk Brillouin zone. The GaSb layers are under biaxial compression and the heavy-hole states are split up from the light-hole states at the center of the bulk Brillouin zone.

The distinctive symmetry-induced features of [001]- and [111]-oriented InAs/GaSb superlattices are revealed by comparing Figs. 9 and 10. Unlike the $\mathrm{Ga}_{1-x}\mathrm{In}_x\mathrm{As}/\mathrm{Al}_{1-y}\mathrm{In}_y\mathrm{As}$ superlattice, the InAs/GaSb superlattice does not have a common anion (or cation). Consequently, the bulk zinc-blende-structure T_d point group is reduced to C_{2v} in [001]-oriented in InAs/GaSb superlattices. The point group C_{2v} contains one twofold irreducible representation compatible with spin: Γ_5. At the center of the superlattice Brillouin zone ($\mathbf{k}_{\parallel}=0$; $Q=0$), the point group is the entire superlattice point group (C_{2v}), and consequently all states are twofold degenerate and belong to the irreducible representation Γ_5. For su-

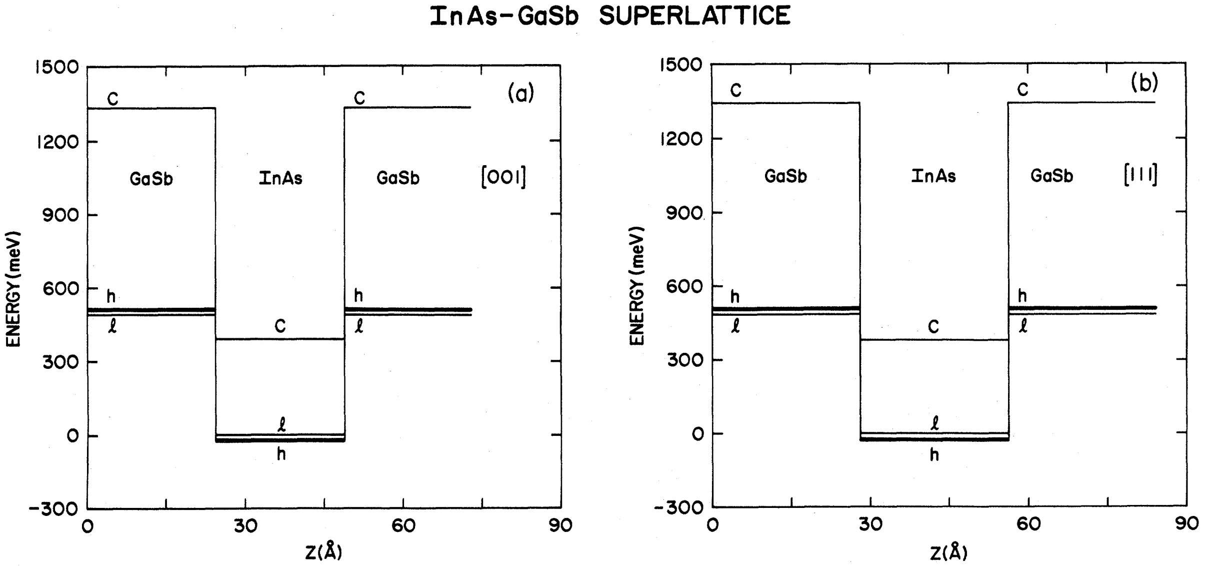

FIG. 8. Energy-band diagram of a superlattice consisting of $M_a=8$ layers of InAs alternating with $N_b=8$ layers of GaSb: (a) [001]-oriented superlattice; (b) [111]-oriented superlattice. The labels *c*, *l*, and *h* identify the conduction, light-hole, and heavy-hole band edges, respectively, at the center of the bulk Brillouin zone. The zero of energy is the valence-band maximum in the strained InAs layers. The two orientations have slightly different diagrams because of anisotropy in the strain splittings.

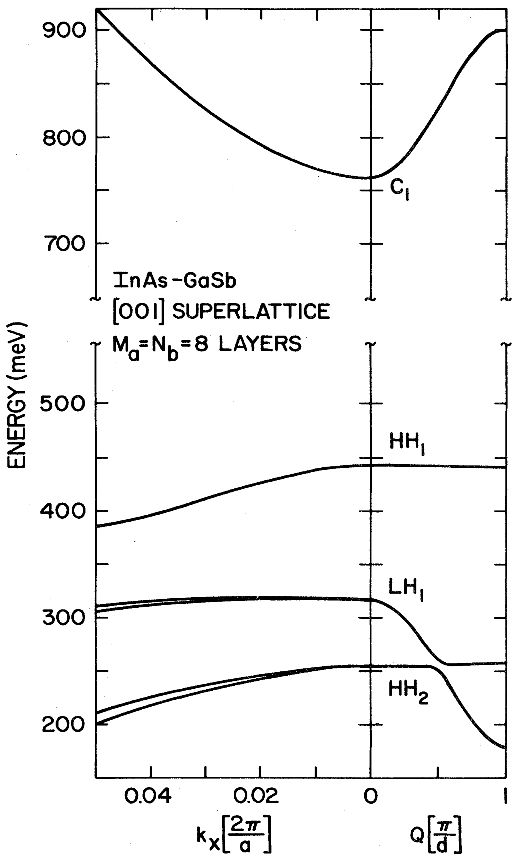

FIG. 9. Electronic energy-band structure of a [001]-growth-axis InAs/GaSb superlattice consisting of $M_a=8$ layers of InAs alternating with $N_b=8$ layers of GaSb. The energy zero coincides with the valence-band maximum of InAs.

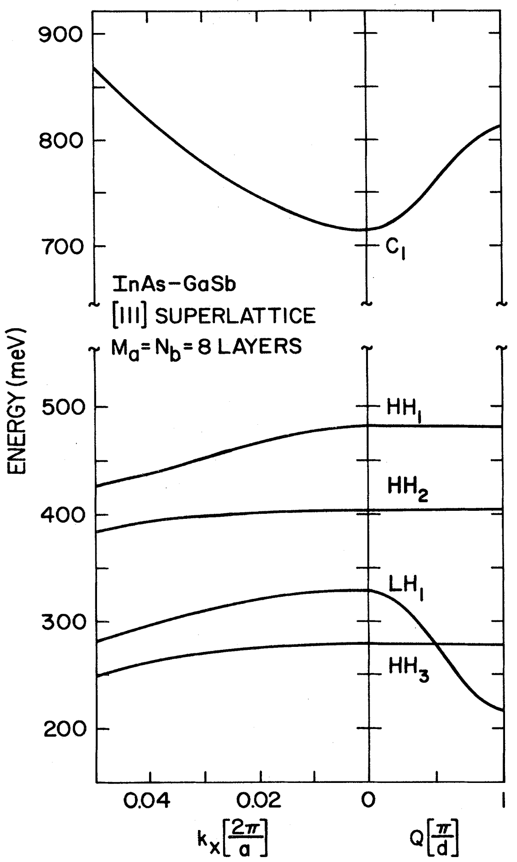

FIG. 10. Electronic energy-band structure of a [111]-growth-axis InAs/GaSb superlattice consisting of $M_a=8$ layers of InAs alternating with $N_b=8$ layers of GaSb. The energy zero coincides with the valence-band maximum of InAs.

perlattice wave vectors oriented along the [001] growth axis ($\mathbf{k}_{\parallel}=0$; $Q\neq 0$) of the superlattice, the point group remains C_{2v}. For a [001]-oriented superlattice, the subbands LH_1 and HH_2 belong to the same irreducible representation, and anticrossing is observed for superlattice wave vectors along the [001] growth axis of the superlattice. In the case of InAs/GaSb superlattices grown along the [111] axis, the point-group analysis is identical to that for the case of $Ga_{1-x}In_xAs/Al_{1-y}In_yAs$ superlattices. The T_d point group associated with bulk zinc-blende-structure compound semiconductors is reduced to C_{3v}. Conduction-band states and light-hole states transform according to Γ_4, whereas heavy-hole states transform according to (Γ_5,Γ_6). For superlattice wave vectors parallel to the [111] growth axis ($\mathbf{k}_{\parallel}=0$; $Q\neq 0$) of the superlattice, the point group remains C_{3v}. Consequently, for a [111]-growth-axis superlattice, the energy subbands LH_1 and HH_3 belong to different irreducible representations and crossing is allowed for superlattice wave vectors directed along the [111] growth axis of the superlattice.

We now discuss the confinement of superlattice wave functions. We consider type-I and type-II superlattices. In type-I superlattices, electrons and holes are both confined within the same layer. In type-II superlattices, electrons and holes are confined in adjacent layers. These features are determined by the energy-band alignment. A type-I superlattice is characterized by an energy-band diagram such as the one shown in Fig. 3 for the $Ga_{0.47}In_{0.53}As/Al_{0.48}In_{0.52}As$ system, whereas a type-II superlattice is characterized by an energy-band diagram such as the one shown in Fig. 8 for the InAs/GaSb system.

Figure 11 shows the squared envelope functions associated with three superlattice states for a [001]-oriented type-I superlattice consisting of 70 Å of $Ga_{0.47}In_{0.53}As$ (quantum wells) alternating with 30 Å of $Al_{0.48}In_{0.52}As$ (barriers). The energy-band diagram of this superlattice is indicated in Fig. 3, and its corresponding energy-band structure is shown in Fig. 4. The squared envelope functions associated with the zone-center superlattice states LH_1, HH_1, and C_1 are shown. Similarly, Fig. 12 shows the squared envelope functions associated with three superlattices states for a [001]-oriented type-II superlattice consisting of $M_a=8$ layers of InAs alternating with $N_b=8$ layers of GaSb. The energy-band diagram of this superlattice is indicated in Fig. 8(a), and its corresponding energy-band structure is shown in Fig. 9. The squared envelope functions associated with the zone-center superlattice states LH_1, HH_1, and C_1 are shown. In the type-I superlattice, the electron and hole states are confined within the $Ga_{0.47}In_{0.53}As$ quantum-well materials. In the type-II superlattice, the electron states are confined within the InAs layers, whereas the hole states are confined within the GaSb layers. In both cases, the envelope functions exhibit a particle-in-a-well character.

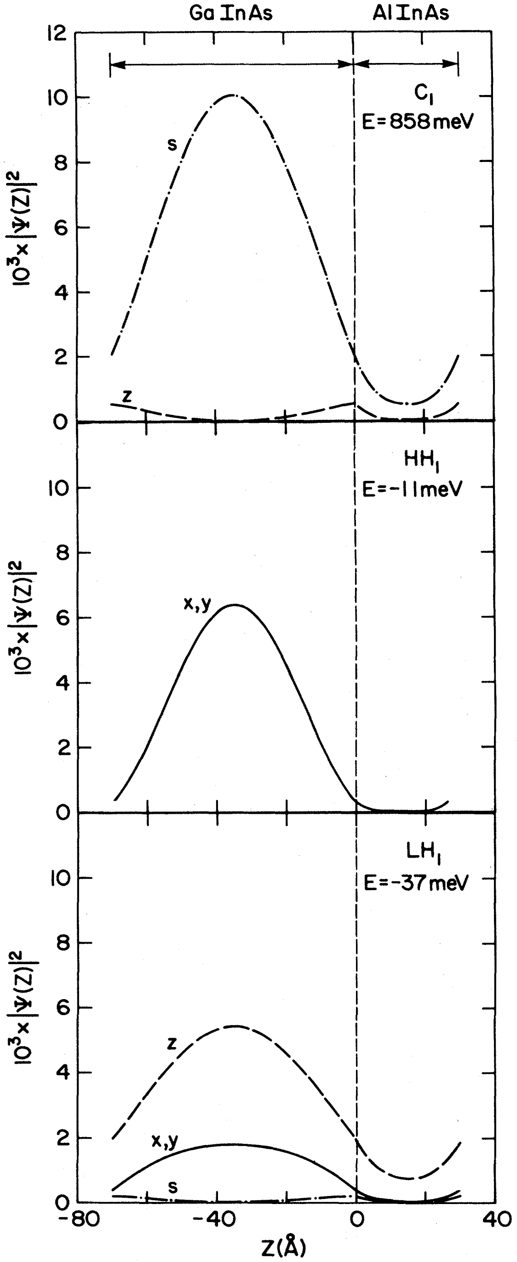

FIG. 11. Symmetry-resolved squared envelope functions associated with various superlattice states for a [001]-oriented type-I superlattice consisting of 70 Å of $Ga_{0.47}In_{0.53}As$ (quantum wells) alternating with 30 Å of $Al_{0.48}In_{0.52}As$ (barriers). The electronic band structure of this superlattice is shown in Fig. 4.

The symmetry character of the envelope functions is indicated by s, x, y, and z, which label the zinc-blende zone-center cell-periodic basis functions belonging to the T_d point group. A summation over spin variables has been performed. Inspection of Figs. 11 and 12 reveals that, in both cases, the state LH_1 contains a large admixture of z and x,y components, that the state HH_1 contains almost uniquely x,y components, and that the C_1 contains mostly an s component.

C. Strained-layer superlattices: No internal piezoelectric field effects

We analyze the differences between [001]- and [111]-growth-axis strained-layer superlattices. In this section, we treat the cases in which the internal piezoelectric field effects are small. In the following section, we consider the cases in which internal field effects dominate the electronic structure and optical response of [111]-oriented strained-layer superlattices.

We first indicate how to calculate the lattice-mismatch-induced strains in the two superlattice constituents. This is accomplished by minimizing the strain energy in the superlattice subject to the constraints imposed by the interfaces' being pseudomorphic. We define the set of orthonormal vectors $\{\hat{\mathbf{N}}_l\}$ so that $\hat{\mathbf{N}}_1$ and $\hat{\mathbf{N}}_2$ lie in the superlattice plane and $\hat{\mathbf{N}}_3$ is orthogonal to this plane. We define the vectors

$$\mathbf{x}_i=(1+\varepsilon_{xx}^i)\hat{\mathbf{x}}+\varepsilon_{xy}^i\hat{\mathbf{y}}+\varepsilon_{xz}^i\hat{\mathbf{z}} , \tag{3.8}$$

where i labels the two constituent materials of the superlattice and we define $\mathbf{y}_i$ and $\mathbf{z}_i$ analogously. The off-diagonal strain components are symmetric ($\varepsilon_{xy}=\varepsilon_{yx}$), so that there are six unknown strain components to be determined in each of the two constituent materials. The zinc-blende primitive lattice translation vectors are

$$\alpha_i=\frac{a_i}{2}(\hat{\mathbf{x}}+\hat{\mathbf{y}}) , \tag{3.9a}$$

$$\beta_i=\frac{a_i}{2}(\hat{\mathbf{y}}+\hat{\mathbf{z}}) , \tag{3.9b}$$

and

$$\gamma_i=\frac{a_i}{2}(\hat{\mathbf{x}}+\hat{\mathbf{z}}) , \tag{3.9c}$$

where a is the lattice constant.

When the crystal is strained, the primitive translation vectors become

$$\alpha_i'=\frac{a_i}{2}(\mathbf{x}_i+\mathbf{y}_i) , \tag{3.10}$$

with analogous expressions for β_i' and γ_i'. The conditions for pseudomorphic interfaces are

$$\boldsymbol{\alpha}_i'\cdot\hat{\mathbf{N}}_1=\boldsymbol{\alpha}_j'\cdot\hat{\mathbf{N}}_1\ , \tag{3.11a}$$

$$\boldsymbol{\alpha}_i'\cdot\hat{\mathbf{N}}_2=\boldsymbol{\alpha}_j'\cdot\hat{\mathbf{N}}_2\ , \tag{3.11b}$$

with analogous conditions on $\boldsymbol{\beta}_i'$ and $\boldsymbol{\gamma}_i'$. These constraint equations are linearized in the lattice-constant difference. Only five of the constraint equations are linearly independent. Thus the constraint equations reduce the number of unknowns, which are determined by minimizing the superlattice strain energy density, from 12 to 7.

The strain energy density of a zinc-blende-structure material is

$$\begin{aligned}U_i=\tfrac{1}{2}C_{11}^i[(\varepsilon_{xx}^i)^2+(\varepsilon_{yy}^i)^2+(\varepsilon_{zz}^i)^2]\\ +2C_{44}^i[(\varepsilon_{xy}^i)^2+(\varepsilon_{xz}^i)^2+(\varepsilon_{yz}^i)^2]\\ +C_{12}^i(\varepsilon_{yy}^i\varepsilon_{zz}^i+\varepsilon_{xx}^i\varepsilon_{zz}^i+\varepsilon_{xx}^i\varepsilon_{yy}^i)\ ,\end{aligned} \tag{3.12}$$

where C's are the elastic constants. For a strained-layer superlattice made up of two zinc-blende-structure materials, the strain energy density is

$$U_{ab}=(U_a h_a+U_b h_b)/(h_a+h_b)\ , \tag{3.13}$$

where h_a (h_b) is the layer thickness of material a (b) in the superlattice. It is a straightforward algebraic exercise to minimize Eq. (3.13) subject to the constraints of Eq. (3.11) and thus to determine the constituent-material strain components.

We consider the cases in which the alloy composition in $\mathrm{Ga}_{1-x}\mathrm{In}_x\mathrm{As}$ is fixed at the value $x=0.53$, whereas the alloy composition in $\mathrm{Al}_{1-y}\mathrm{In}_y\mathrm{As}$ is varied to produce a relative lattice mismatch of $\Delta a_0/a_0=1\%$ ($y=0.67$) and $\Delta a_0/a_0=-1\%$ ($y=0.37$). The material with the smaller lattice constant expands in the interface plane as a result of biaxial tensile stress, whereas the material with the larger lattice constant contracts in the interface plane due to a biaxial compressive stress.

For a superlattice made of two zinc-blende-structure materials and with a [001] growth axis, only diagonal strain components are introduced (i.e., $\varepsilon_{xy}=0$, etc.) by lattice mismatch. The diagonal components are (Osbourn, 1982a)

$$\varepsilon_{zz}^i=-\frac{2C_{12}^i}{C_{11}^i}\varepsilon_{xx}^i\ , \tag{3.14a}$$

$$\varepsilon_{xx}^a=\varepsilon_{yy}^a=\frac{-\Delta a_0}{a_0}\,\frac{G^b b}{G^a a+G^b b}\ , \tag{3.14b}$$

$$\varepsilon_{xx}^b=\varepsilon_{yy}^b=\frac{\Delta a_0}{a_0}\,\frac{G^a a}{G^a a+G^b b}\ , \tag{3.14c}$$

where

$$\Delta a_0=a_0^a-a_0^b\ , \tag{3.14d}$$

$$a_0=\frac{a_0^a+a_0^b}{2}\ , \tag{3.14e}$$

$$G^i=2\left[C_{11}^i+C_{12}^i-\frac{2(C_{12}^i)^2}{C_{11}^i}\right]\ , \tag{3.14f}$$

and a_0 refers to a lattice constant and the C's are the elastic constants. We neglect the spin dependence of the stress interaction. Then, the strain Hamiltonian is independent of spin and has nonzero matrix elements (Bir and Pikus, 1974):

$$\langle s|H_{\mathrm{st}}^{[001]}|s\rangle=c^i(2\varepsilon_{xx}^i+\varepsilon_{zz}^i)\ , \tag{3.15a}$$

$$\langle x|H_{\mathrm{st}}^{[001]}|x\rangle=\langle y|H_{\mathrm{st}}^{[001]}|y\rangle=(l^i+m^i)\varepsilon_{xx}^i+m^i\varepsilon_{zz}^i\ , \tag{3.15b}$$

$$\langle z|H_{\mathrm{st}}^{[001]}|z\rangle=2m^i\varepsilon_{xx}^i+l^i\varepsilon_{zz}^i\ , \tag{3.15c}$$

where c, l, and m are deformation-potential constants.

Figure 13 shows the energy-band diagram of a [001]-oriented strained-layer superlattice consisting of $M_a=12$ layers of $\mathrm{Ga}_{0.47}\mathrm{In}_{0.53}\mathrm{As}$ (quantum wells) alternating with $N_b=12$ layers of $\mathrm{Al}_{1-x}\mathrm{In}_x\mathrm{As}$ (barriers). Results are shown for $y=0.67$ in Fig. 13(a) and for $y=0.37$ in Fig. 13(b). The period of these superlattices is about 70 Å. The calculated electronic band structures of these superlattices are shown in Figs. 14 and 15, respectively. In both cases, the lattice mismatch between the two materials is 1%. In the case of the $\mathrm{Ga}_{0.47}\mathrm{In}_{0.53}\mathrm{As}/\mathrm{Al}_{0.33}\mathrm{In}_{0.67}\mathrm{As}$ superlattice [Fig. 13(a)], the $\mathrm{Ga}_{0.47}\mathrm{In}_{0.53}\mathrm{As}$ layers are under biaxial tension. In the case of the $\mathrm{Ga}_{0.47}\mathrm{In}_{0.53}\mathrm{As}/\mathrm{Al}_{0.63}\mathrm{In}_{0.37}\mathrm{As}$ superlattice [Fig. 13(b)], the $\mathrm{Ga}_{0.47}\mathrm{In}_{0.53}\mathrm{As}$ layers are under biaxial compression. As a result of the internal strain present within the layers, the two materials' valence-band maxima are split due to deformation-potential effects. The average valence-band offset ΔE_v^{av}, where $E_v^{\mathrm{av}}=(E_{\mathrm{HH}}+E_{\mathrm{LH}}+E_{\mathrm{SOH}})/3$, is taken to be independent of orientation and of strain on the basis of *ab initio* pseudopotential calculations (Van de Walle and Martin, 1986b). The ratio $\Delta E_v^{\mathrm{av}}/\Delta Eg$ is taken to be independent of alloy composition and determined from measurements on the lattice-matched system (People *et al.*, 1983). The valence-band offset has a value of 105 meV for the $\mathrm{Ga}_{0.47}\mathrm{In}_{0.53}\mathrm{As}/\mathrm{Al}_{0.33}\mathrm{In}_{0.67}\mathrm{As}$ superlattice and 364 meV for the $\mathrm{Ga}_{0.47}\mathrm{In}_{0.53}\mathrm{As}/\mathrm{Al}_{0.63}\mathrm{In}_{0.37}\mathrm{As}$ superlattice.

Electronic band structures of $\mathrm{Ga}_{0.47}\mathrm{In}_{0.53}\mathrm{As}$(35 Å)/$\mathrm{Al}_{1-y}\mathrm{In}_y\mathrm{As}$(35 Å) strained-layer superlattices are indicated in panel (a) of Figs. 14 and 15 for $y=0.67$ ($\Delta a_0/a_0=1\%$) and $y=0.37$ ($\Delta a_0/a_0=-1\%$), respectively. The presence of a uniaxial stress can induce a reversal in the ordering of the superlattice subbands HH_1 and LH_1 by lowering the first heavy-hole subband (HH_1) below the first light-hole subband (LH_1) (Schirber, Fritz, and Dawson, 1985). However, the cases illustrated in Figs. 14 and 15 correspond to rather-thin-layer superlattices, and such a reversal is not observed. The $\mathbf{k}_\parallel=0$ portion of the band structure, in the case in which stress-induced effects are neglected, is also shown in panel (b) of Figs. 14 and 15. Comparison between panels (a) and (b) of Figs. 14 and 15 shows the significance of stress-induced effects in the electronic band structure of semiconductor superlattices.

In Fig. 14, where the smaller-band-gap $\mathrm{Ga}_{0.47}\mathrm{In}_{0.53}\mathrm{As}$

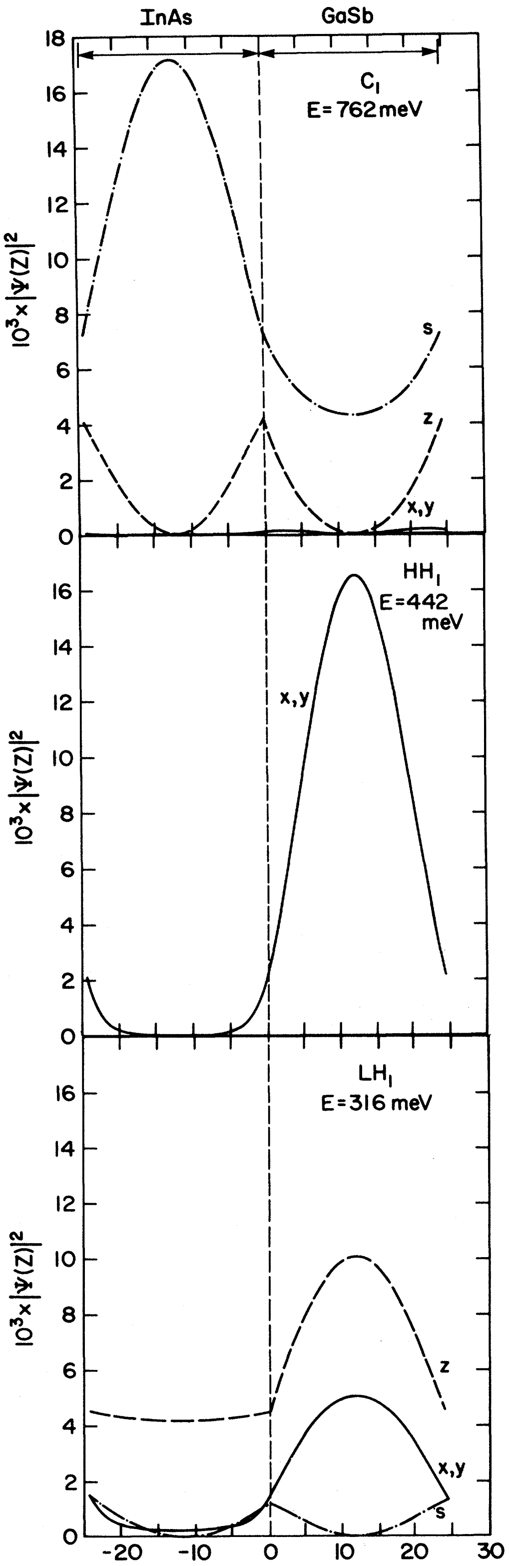

FIG. 12. Symmetry-resolved squared envelope functions associated with various superlattice states for a [001]-oriented type-II superlattice consisting of $M_a = 8$ layers of InAs alternating with $N_b = 8$ layers of GaSb. The electronic band structure of this superlattice is shown in Fig. 9.

is under biaxial tension, the splitting between the HH_1 and LH_1 states is reduced by strain. When higher-strain cases are considered, a reversal in energy position of these states occurs for thick-layer superlattices. In Fig. 15, where the smaller-band-gap $Ga_{0.47}In_{0.53}As$ is under biaxial compression, the splitting between the HH_1 and LH_1 states is increased by strain. The symmetry-induced features of the electronic band structure discussed in Sec. III.B are also observed for strained-layer superlattices, as suggested by comparison of Figs. 4, 5, 14, and 15. The strong hybridization of the hole subbands for $\mathbf{k}_{\parallel} \neq 0$ results in highly nonparabolic subband dispersion and, in some instances, in a positive value of the in-plane hole effective mass at the center of the superlattice Brillouin zone.

We consider the electronic structure of strained-layer superlattices grown along the [111] axis. Internal strains generate large piezoelectric fields in [111]-oriented strained-layer superlattices. The effects of the internal piezoelectric fields on the properties of [111]-growth-axis strained-layer superlattices are larger for thick-layer superlattices. In the present section, we restrict our analysis to thin-layer superlattices in which internal field effects are small, and therefore we focus on deformation-potential effects. In Sec. III.D we treat cases in which internal field effects dominate the electronic structure and optical properties of [111]-oriented strained-layer superlattices.

Lattice-mismatch-induced strains do not change the symmetry of a strained-layer superlattice compared to the lattice-matched case. These strains do, however, lead to local energy-level splittings in each constituent material forming the superlattice. These energy-level splittings are described by bulk deformation potentials for the constituent materials. The orientation of the strains for [111] superlattices is different from that for [001] superlattices; hence the strain interaction is different for the two cases.

The calculation of lattice-mismatch-induced strain Hamiltonians for [111]-growth-axis strained-layer superlattices proceeds in a manner similar to that of the [001]-growth-axis case. We apply the general procedure outlined above to the case of [111]-oriented strained-layer superlattices. By the symmetry of the problem, the three diagonal strain components are equal in each material. Thus there are four unknowns: a diagonal and an off-diagonal strain component in each material. To first order in the difference in lattice constants, one finds

$$\varepsilon_{xx}^{a} = \frac{1}{(1+A^{a})+(1+A^{b})B(h_a/h_b)} \left[\frac{a^{b}}{a^{a}} - 1 \right] , \tag{3.16a}$$

$$\varepsilon_{xx}^{b} = -\frac{h_a}{h_b} B \varepsilon_{xx}^{a} , \tag{3.16b}$$

$$\varepsilon_{xy}^{a} = -A^{a} \varepsilon_{xx}^{a} , \tag{3.16c}$$

and

$$\varepsilon_{xy}^{b} = -A^{b} \varepsilon_{xx}^{b} , \tag{3.16d}$$

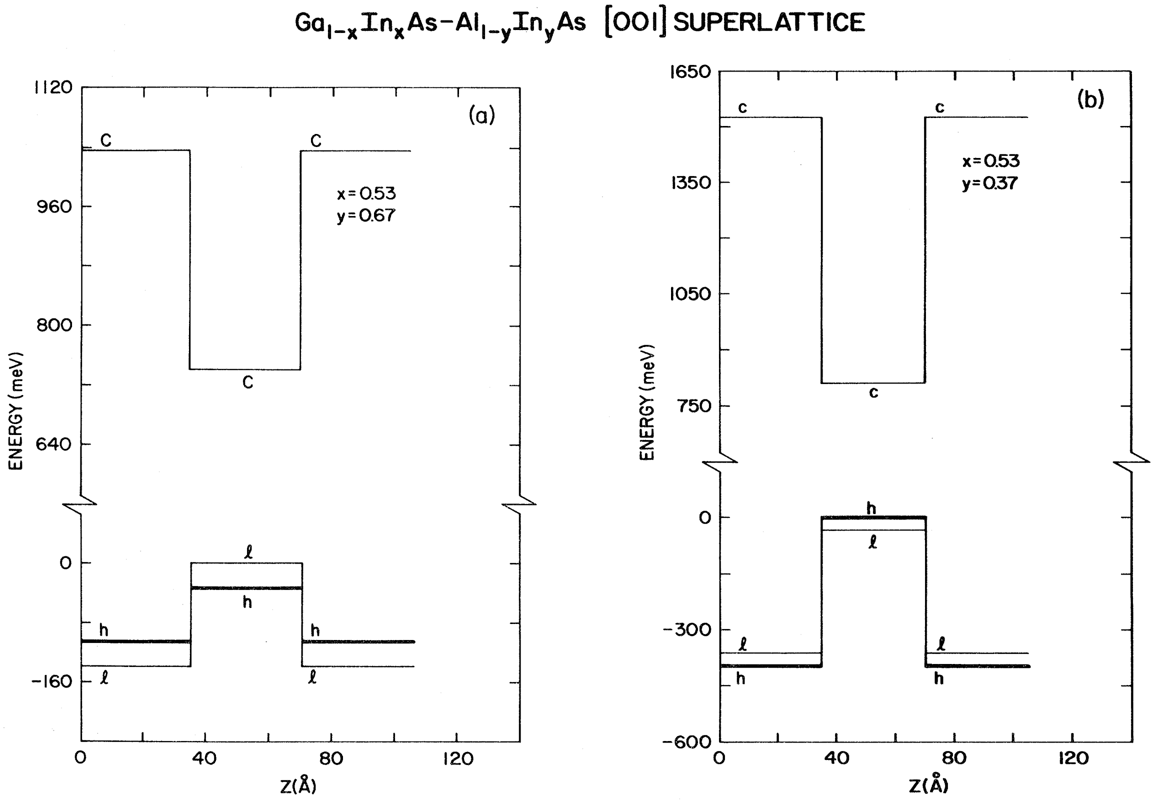

FIG. 13. Energy-band diagram of a [001]-oriented strained-layer superlattice consisting of $M_a = 12$ layers of $Ga_{0.47}In_{0.53}As$ (quantum wells) alternating with $N_b = 12$ layers of $Al_{1-x}In_xAs$ (barriers): (a) results for $y = 0.67$ with the $Ga_{0.47}In_{0.53}As$ well layers under biaxial tension; (b) results for $y = 0.37$ with the $Ga_{0.47}In_{0.53}As$ well layers under biaxial compression. The labels c, l, and h identify the conduction, light-hole, and heavy-hole band edges, respectively, at the center of the bulk Brillouin zone. The zero of energy is the valence-band maximum in the strained $Ga_{0.47}In_{0.53}As$ quantum wells.

where

$$A^i = \frac{C_{11}^i + 2C_{12}^i}{4C_{44}^i} , \tag{3.17a}$$

$$B = \frac{C_{11}^a + 2C_{12}^a}{C_{11}^b + 2C_{12}^b} , \tag{3.17b}$$

and where h_i is the layer thickness of material i and the C's are the elastic constants.

The [111] strain Hamiltonian in material i has upper-triangle nonvanishing matrix elements

$$\langle s|H_{\rm st}^{[111]}|s\rangle = 3c^i\varepsilon_\perp^i , \tag{3.18a}$$

$$\langle x|H_{\rm st}^{[111]}|x\rangle = \langle y|H_{\rm st}^{[111]}|y\rangle = \langle z|H_{\rm st}^{[111]}|z\rangle = (l^i + 2m^i)\varepsilon_\perp^i , \tag{3.18b}$$

$$\langle x|H_{\rm st}^{[111]}|y\rangle = \langle x|H_{\rm st}^{[111]}|z\rangle = \langle y|H_{\rm st}^{[111]}|z\rangle = n^i\varepsilon_\parallel^i , \tag{3.18c}$$

where $\varepsilon_\parallel^i = \varepsilon_{xy}^i = \varepsilon_{yz}^i = \varepsilon_{zx}^i$ and $\varepsilon_\perp^i = \varepsilon_{xx}^i = \varepsilon_{yy}^i = \varepsilon_{zz}^i$. In Eqs. (3.18), the constants c^i, n^i, and m^i are the deformation-potential constants of semiconductor i. In principle, the strains $\varepsilon_\parallel$ couple the $|s\rangle$ and $|x\rangle$, etc., states. However, this coupling is not important, except in very-small-band-gap materials, because of the large energy separation between the states.

Figure 16 shows the energy-band diagram of a [111]-oriented strained-layer superlattice consisting of $M_a = 10$ layers of $Ga_{0.47}In_{0.53}As$ (quantum wells) alternating with $N_b = 10$ layers of $Al_{1-x}In_xAs$ (barriers). Results are shown for $y = 0.67$ in Fig. 16(a) and for $y = 0.37$ in Fig. 16(b). The period of these superlattices is about 68 Å. The calculated electronic band structures of these superlattices are indicated in Figs. 17 and 18, respectively. These alloy compositions are the same as those shown in Fig. 13. Since there is a 1% lattice mismatch between $Ga_{0.47}In_{0.53}As$ and $Al_{1-x}In_xAs$, strain-induced internal piezoelectric fields are present within the layers of [111]-oriented strained-layer superlattices. (Such internal fields vanish for [001]-oriented strained-layer superlattices.) The internal piezoelectric fields are shown as sloping

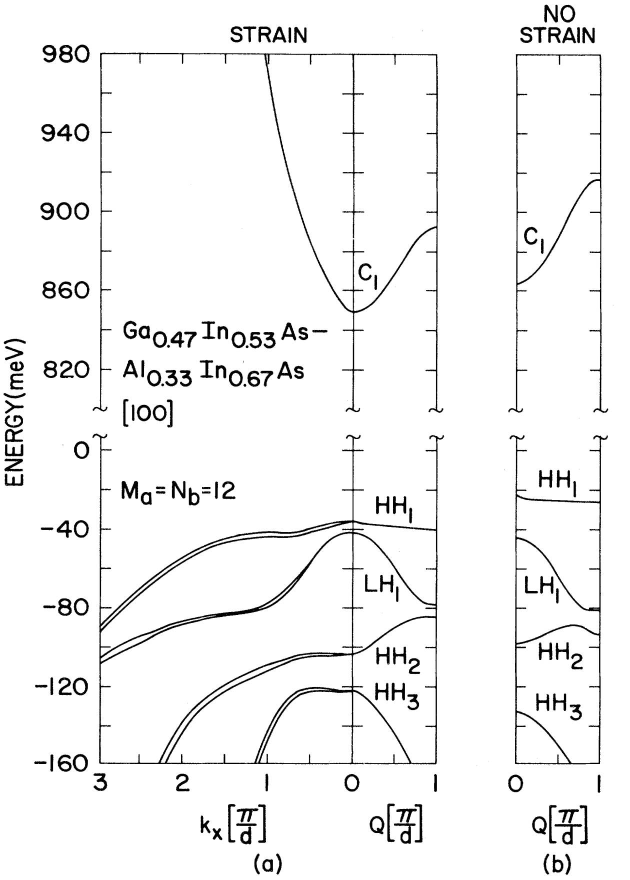

FIG. 14. Electronic energy-band structure of a [001]-growth-axis strained-layer superlattice consisting of 12 layers of $Ga_{0.47}In_{0.53}As$ alternating with 12 layers of $Al_{0.33}In_{0.67}As$: (a) strain effects included; (b) strain effects excluded. The $Ga_{0.47}In_{0.53}As$ quantum wells are in biaxial tension because of a lattice mismatch of 1%. The energy zero coincides with the valence-band maximum of unstrained $Ga_{0.47}In_{0.53}As$.

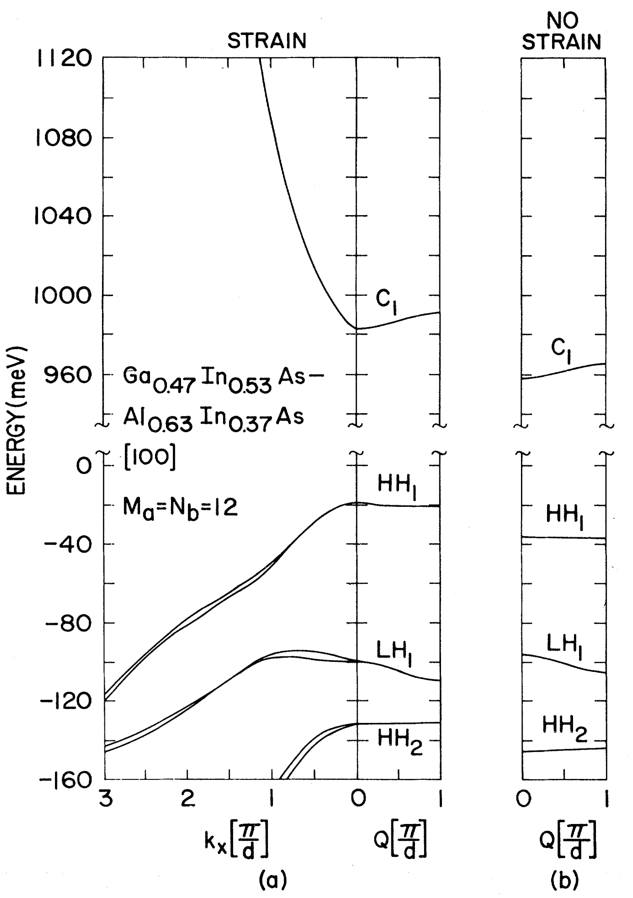

FIG. 15. Electronic energy-band structure of a [001]-growth-axis strained-layer superlattice consisting of 12 layers of $Ga_{0.47}In_{0.53}As$ alternating with 12 layers of $Al_{0.63}In_{0.37}As$: (a) strain effects included; (b) strain effects excluded. The $Ga_{0.47}In_{0.53}As$ quantum wells are in biaxial compression owing to a lattice mismatch of 1%. The energy zero coincides with the valence-band maximum of unstrained $Ga_{0.47}In_{0.53}As$.

band edges in Fig. 16. The effects of these internal piezoelectric fields on the electronic-structure of such thin-layer superlattices are small and are neglected in the electronic-structure calculations presented in Figs. 17 and 18. The effects of strain are included in the calculations shown in panel (a) of Figs. 17 and 18, but they are excluded in panel (b).

Figures 14 and 17 correspond to similar superlattice systems; the electronic band structure is calculated for a [001]-growth-axis strained-layer superlattice in Fig. 14 and a [111]-growth-axis strained-layer superlattice in Fig. 17. Since the components of the strain tensor are different in the two cases, deformation-potential effects are different. The $Ga_{0.47}In_{0.53}As$ quantum wells are under biaxial tension, and the presence of internal strain reduces the energy separation between the subbands HH_1 and LH_1. Therefore the LH_1-HH_1 energy separation is smaller when strain effects are included [panel (a)] than when they are excluded [panel (b)].

Figures 15 and 18 also correspond to similar superlattice systems; the electronic band structure is calculated for a [001]-growth-axis strained-layer superlattice in Fig. 15 and a [111]-growth-axis strained-layer superlattice in Fig. 18. Since the $Ga_{0.47}In_{0.53}As$ quantum wells are under biaxial compression, the presence of internal strain increases the energy separation between the subbands HH_1 and LH_1. Therefore, LH_1-HH_1 energy separation is larger when strain effects are included [panel (a)] than when they are excluded [panel (b)]. Since bulk heavy-hole masses are larger in the [111] direction than in the [001] direction, quantum confinement effects are relatively more important for the heavy-hole states in [111] superlattices than in [001] superlattices.

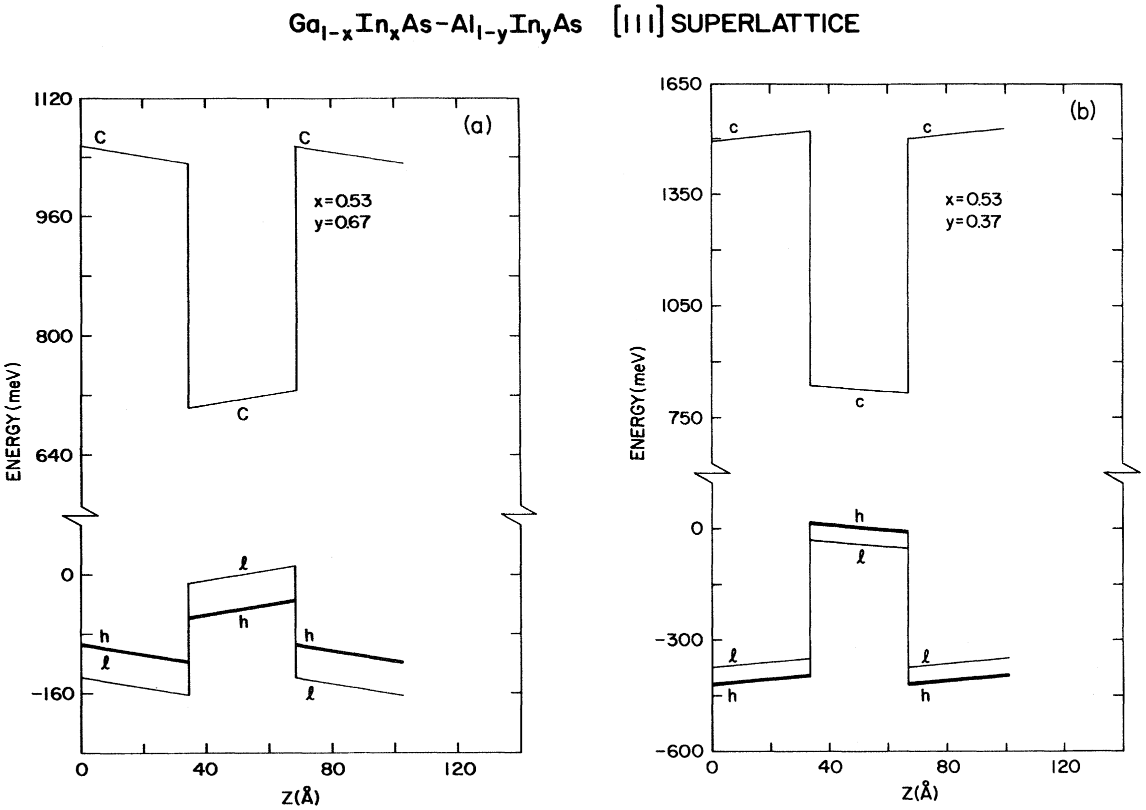

FIG. 16. Energy-band diagram of a [111]-oriented strained-layer superlattice consisting of $M_a = 10$ layers of $Ga_{0.47}In_{0.53}As$ (quantum wells) alternating with $N_b = 10$ layers of $Al_{1-x}In_xAs$ (barriers): (a) results for $y = 0.67$ with the $Ga_{0.47}In_{0.53}As$ well layers under biaxial tension; (b) results for $y = 0.37$ with the $Ga_{0.47}In_{0.53}As$ well layers under biaxial compression. Strain-induced internal piezoelectric fields are present within the layers. The effects of these internal piezoelectric fields on the electronic structure of such thin-layer superlattices is small and is neglected in electronic-structure calculations for this case. The labels c, l, and h identify the conduction, light-hole, and heavy-hole band edges, respectively, at the center of the bulk Brillouin zone. The zero of energy is the valence-band maximum in the strained $Ga_{0.47}In_{0.53}As$ quantum wells.

D. Strained-layer superlattices: Internal piezoelectric field effects

We now consider strained-layer superlattices when the internal piezoelectric field effects dominate the electronic structure and optical response of [111]-oriented strained-layer superlattices. In this section we describe the origin of the piezoelectric fields and indicate how these internal fields modify the superlattice energy levels and wave functions. In the next section we describe how the optical properties of [111]-growth-axis strained-layer superlattices can be modified by modulating the internal piezoelectronic fields.

Zinc-blende-structure semiconductors are piezoelectric materials. Off-diagonal strains induce a polarization given by (Cady, 1946)

$$P_i^s = 2e_{14}\varepsilon_{jk} , \tag{3.19}$$

where P^s is the induced polarization, e_{14} is the piezoelectric constant, and ε_{jk} is a symmetrized strain component. However, diagonal strains (e.g., ε_{xx}) do not induce a polarization (i.e., $e_{11} = 0$) in these materials (Cady, 1946). A strained-layer superlattice with a [001] growth direction will induce only diagonal strains; but, with any other growth direction, off-diagonal strains also occur. Thus [001]-growth axis strained-layer superlattices will not have strain-induced polarization fields, but strained-layer superlattices with any other growth direction will have these polarization fields.

From the strain components, the strain-induced polarization $\mathbf{P}^s$ is determined from Eq. (3.19). The polarization vector is constant in each material layer and changes abruptly at the interfaces. Because one of the constituent materials is in biaxial tension and the other is in biaxial compression, the polarization vector changes sign at the interface. For a [111] growth axis, $\mathbf{P}^s$ is parallel to the growth axis; for a [110] growth axis, $\mathbf{P}^s$ is in the superlattice plane; for a [001] growth axis, $\mathbf{P}^s$ vanishes. For a

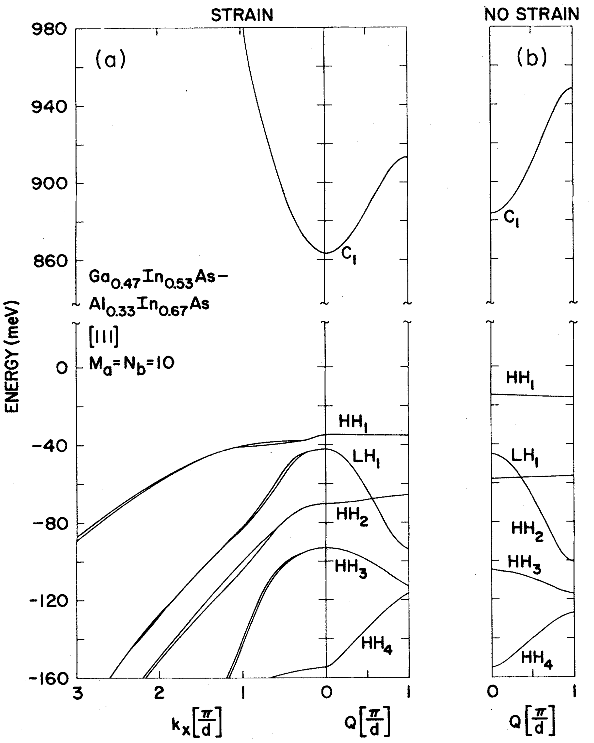

FIG. 17. Electronic energy-band structure of a [111]-growth-axis strained-layer superlattice consisting of 10 layers of $Ga_{0.47}In_{0.53}As$ alternating with 10 layers of $Al_{0.33}In_{0.67}As$: (a) strain effects included; (b) strain effects excluded. The $Ga_{0.47}In_{0.53}As$ quantum wells are in biaxial tension owing to a lattice mismatch of 1%. Internal strain-induced piezoelectric effects are neglected since the superlattice layers are thin. The energy zero coincides with the valence-band maximum of unstrained $Ga_{0.47}In_{0.53}As$.

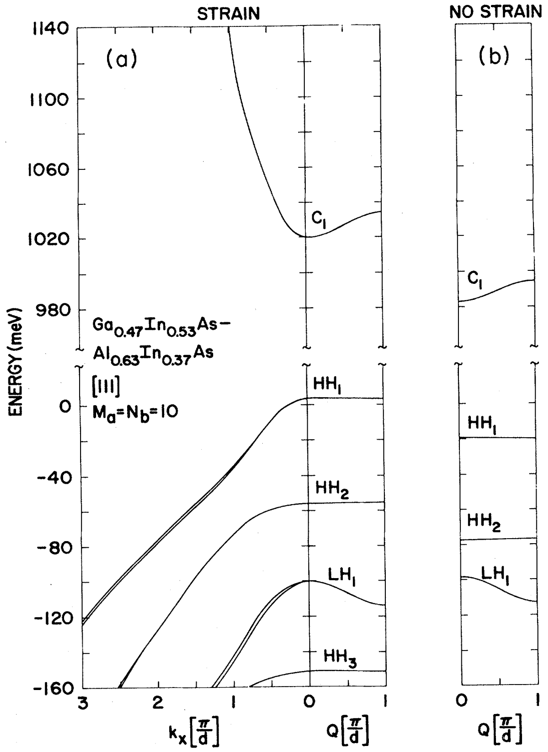

FIG. 18. Electronic energy-band structure of a [111]-growth-axis strained-layer superlattice consisting of 10 layers of $Ga_{0.47}In_{0.53}As$ alternating with 10 layers of $Al_{0.63}In_{0.37}As$: (a) strain effects included; (b) strain effects excluded. The $Ga_{0.47}In_{0.53}As$ quantum wells are in biaxial compression owing to a lattice mismatch of 1%. Internal strain-induced piezoelectric effects are neglected since the superlattice layers are thin. The energy zero coincides with the valence-band maximum of unstrained $Ga_{0.47}In_{0.53}As$.

general growth axis, $\mathbf{P}^s$ has components both parallel and perpendicular to the growth axis. The general result for the induced polarization has been presented elsewhere (Smith and Mailhiot, 1988b).

The strain-induced polarization $\mathbf{P}^s$ can generate electric fields $\mathbf{E}$ and/or displacement fields $\mathbf{D}$. The electrostatic equations are

$$\nabla\cdot\mathbf{D}=4\pi\rho_e\ , \tag{3.20a}$$

$$\nabla\times\mathbf{E}=0\ , \tag{3.20b}$$

$$\mathbf{D}=\mathbf{E}+4\pi\mathbf{P}\ , \tag{3.20c}$$

and

$$\mathbf{P}=\eta\mathbf{E}+\mathbf{P}^s\ , \tag{3.20d}$$

where ρ_e is an external charge density and η is the susceptibility. It is convenient to divide $\mathbf{P}^s$ into longitudinal (perpendicular to the superlattice interface) $\mathbf{P}_\perp^s$ and transverse (parallel to the superlattice interface) $\mathbf{P}_\parallel^s$ components. The electrostatic equations become

$$\nabla\cdot\mathbf{E}=\frac{4\pi(\rho_e-\nabla\cdot\mathbf{P}_\perp^s)-\nabla\kappa\cdot\mathbf{E}}{\kappa}\ , \tag{3.21a}$$

$$\nabla\times\mathbf{E}=0\ , \tag{3.21b}$$

$$\nabla\cdot\mathbf{D}=4\pi\rho_e\ , \tag{3.21c}$$

$$\nabla\times\mathbf{D}=4\pi\nabla\times\mathbf{P}_\parallel^s+\nabla\kappa\times\mathbf{E}\ , \tag{3.21d}$$

and

$$\mathbf{D}=\kappa\mathbf{E}+4\pi\mathbf{P}^s\ , \tag{3.21e}$$

where

$$\kappa=1+4\pi\eta\ . \tag{3.21f}$$

Nonzero values of $\nabla\cdot\mathbf{P}_\perp^s$ and $\nabla\times\mathbf{P}_\parallel^s$ occur at the interfaces and serve as sources of $\mathbf{E}$ and $\mathbf{D}$, respectively. We consider the case in which there is no external charge and neglect the small difference in dielectric constants,

$$E_\perp = -\frac{4\pi P_\perp^s}{\kappa}\ , \tag{3.22a}$$

$$E_\parallel = 0\ , \tag{3.22b}$$

$$D_\perp = 0\ , \tag{3.22c}$$

and

$$D_\parallel = 4\pi P_\parallel^s\ . \tag{3.22d}$$

As a numerical example, we consider a GaAs/$\mathrm{Ga_{0.8}In_{0.2}As}$ superlattice, for which there is a 1.4% lattice-constant mismatch. In Fig. 19 we show $E_\perp$ in the GaInAs layers as a function of growth-axis orientation for superlattices with equally thick constituent layers. We define the growth axis in polar coordinates and show results as a function of the polar angle Θ for the azimuthal angle Φ fixed at $\pi/4$. We see that $E_\perp$ is zero at $\Theta=0$, corresponding to a [100] growth axis. It has a broad maximum at a [111] growth axis and returns to zero for a [011] growth axis. The electric fields shown in Fig. 19 originate from polarization charge at the heterojunction interfaces. The peak of the field in Fig. 19 corresponds to an interface charge of $2\times10^{12}\ e/\mathrm{cm}^2$. In principle, this interface charge could be screened by mobile charge in the superlattice. For a 100-Å superlattice layer thickness, mobile charge densities in excess of $10^{18}\ \mathrm{cm}^{-3}$ would be required to produce this screening. It is possible to grow superlattices with much lower mobile charge densities, and the results described here should not be affected by such screening.

In Fig. 20 we show $P_\parallel^s$ for the same superlattice as a function of Θ for $\Phi=\pi/4$. We see that $P_\parallel^s$ has zeros for [100] and [111] growth axes, a maximum for [011] growth axes, and a subsidiary maximum between [311] and [211]. In Fig. 21 we show $P_\parallel^s$ as a function of Θ for $\Phi=0$. Along this plane, $P_\perp^s$, and hence $E_\perp$, vanishes. We see that $P_\parallel^s$ is zero for a [100] growth axis and that it has a broad maximum for a [110] growth axis.

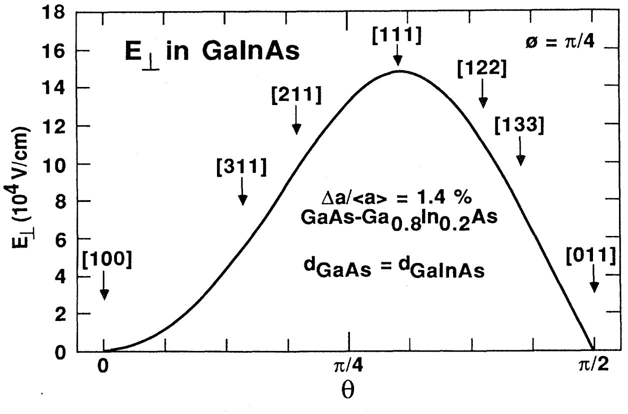

FIG. 19. Strain-generated longitudinal electric field in a GaAs/$\mathrm{Ga_{0.8}In_{0.2}As}$ superlattice as a function of growth direction. The azimuthal angle is fixed as $\pi/4$, and results are shown as a function of the polar angle.

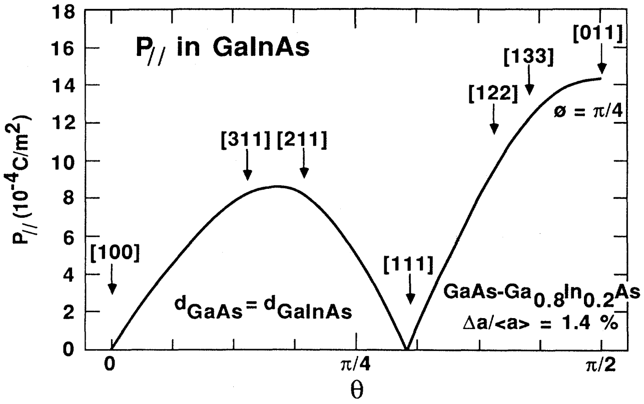

FIG. 20. Strain-generated transverse polarization in a GaAs/$\mathrm{Ga_{0.8}In_{0.2}As}$ superlattice as a function of growth direction. The azimuthal angle is fixed at $\pi/4$, and results are shown as a function of the polar angle.

The electric fields and polarizations indicated in Figs. 19–21 reach rather large values. The polarizations are comparable to the spontaneous polarization in weak ferroelectrics. For comparison, the spontaneous polarization of Rochelle salt is $2.6\times10^{-3}\ \mathrm{C/m^2}$. Electric fields, such as those in Fig. 19, are capable of causing large changes in the electronic structure and the optical properties of strained-layer superlattices. These longitudinal electric fields are largest for a [111] growth axis, but the maximum is broad, and electric fields nearly as large can be reached for other growth orientations. Note that the strain-induced electric fields are purely longitudinal. There is no transverse component of the strain-induced electric field in the superlattice plane, even if the growth axis is off [111]. The transverse polarization fields shown in Fig. 20 do not generate electric fields and do not change the quantum well and confining-barrier energy-band diagrams. Therefore they do not directly change

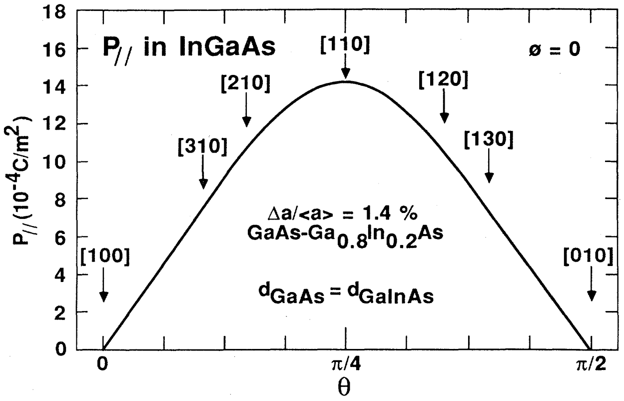

FIG. 21. Strain-generated transverse polarization in a GaAs/$\mathrm{Ga_{0.8}In_{0.2}As}$ superlattice as a function of growth direction. The azimuthal angle is fixed at zero, and results are shown as a function of the polar angle. There are no longitudinal fields generated for this value of the azimuthal angle.

the superlattice electronic structure in the way the longitudinal electric fields do. However, these transverse polarizations lead to birefringence for light propagating along the superlattice growth axis. Finally, we note that the strain-induced polarization effects discussed here are not limited to zinc-blende-structure semiconductors. Similar effects could occur in other materials systems. Indeed, they could be much larger in materials with larger piezoelectric coefficients.

Inspection of Fig. 19 reveals that the internal strain-induced piezoelectric fields are comparable to or larger than those that occur in the depletion region of a *p-n* junction and are approaching breakdown fields (~ 350 kV/cm in GaAs). As one would expect, the fields are larger in the thinner material because the strain is greater in that region. Although the electric fields in the two materials are of opposite sign, they do not, in general, cancel to zero. Thus, in general, the fields described by Eqs. (3.22) consist of an alternating periodic component (that is, the potential returns to zero across a superlattice unit cell) plus a net long-range field. We assume that the long-range field will be canceled by surface charges on the superlattice sample, and we treat only the effects of the periodic component on the superlattice electronic structure. We describe this periodic field by linearly varying potentials in each constituent material of the superlattice.

We now investigate the effects of the strain-induced electric fields on the electronic structure of [111] superlattices. We compare calculations of zone-center subband energies, subband dispersions, and wave functions with and without the electric fields. The superlattice band gap is reduced and subband energy splittings are significantly altered by the electric fields. The subband wave functions and optical matrix elements are also strongly modified by the fields. The wave functions are displaced in space, so that free carriers screen the internal fields. Heavy holes are more effective at screening the fields than electrons or light holes. It requires a density of $\sim 10^{18}$ cm^{-3} heavy holes to reduce the internal fields by a factor of 2.

We first consider the case in which the confining layers are under biaxial compression due to a lattice mismatch of -1.5%. Figure 22 shows the energy-band diagram of a [111]-oriented strained-layer superlattice consisting of $M_a = 20$ layers of $Ga_{0.47}In_{0.53}As$ (quantum wells) alternating with $N_b = 20$ layers of $Al_{0.70}In_{0.30}As$ (barriers). The valence-band offset has a value of 429 meV. As a result

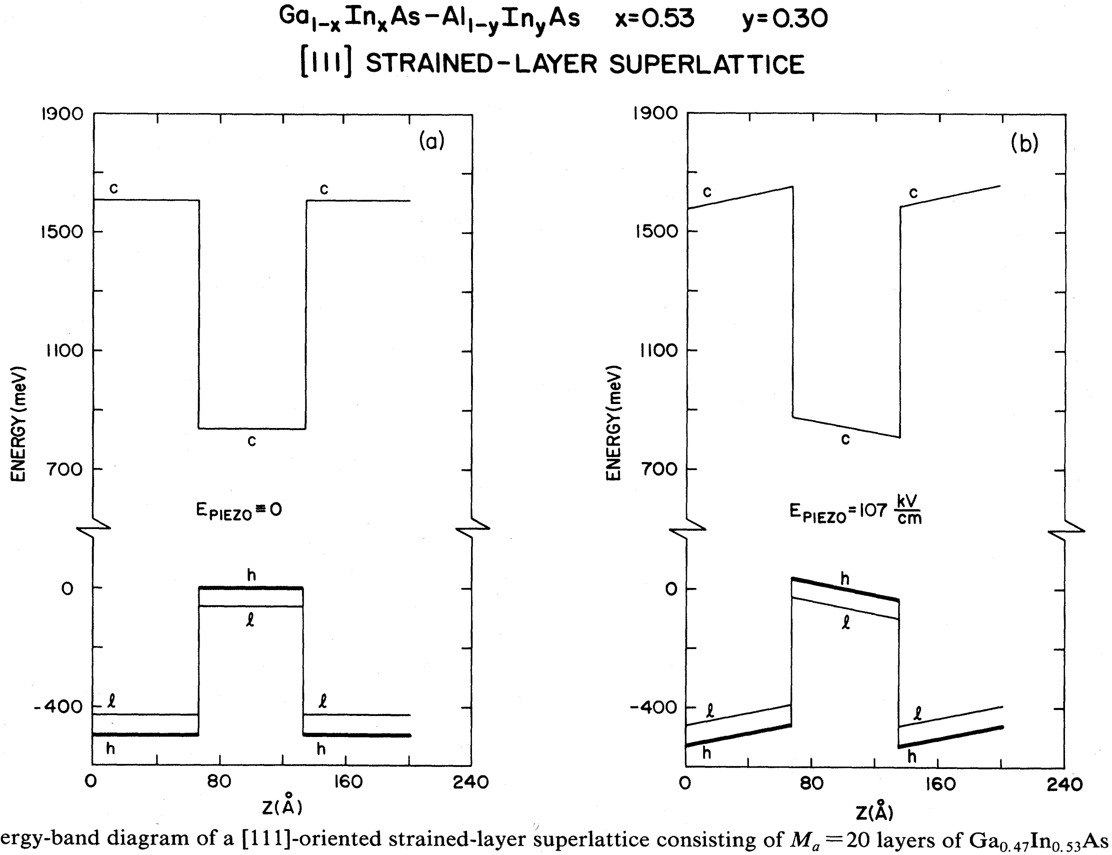

FIG. 22. Energy-band diagram of a [111]-oriented strained-layer superlattice consisting of $M_a = 20$ layers of $Ga_{0.47}In_{0.53}As$ (quantum wells) alternating with $N_b = 20$ layers of $Al_{0.70}In_{0.30}As$ (barriers): (a) energy-band diagram without the internal piezoelectric fields; (b) energy-band diagram with the internal piezoelectric fields. The internal piezoelectric field has a value of $E = 107$ kV/cm in the $Ga_{0.47}In_{0.53}As$ quantum-well layers. The labels *c*, *l*, and *h* identify the conduction, light-hole, and heavy-hole band edges, respectively, at the center of the bulk Brillouin zone. The zero of energy is the valence-band maximum at the center of the strained $Ga_{0.47}In_{0.53}As$ quantum wells.

of the lattice mismatch, strain-induced internal piezoelectric fields are present within the layers. The internal piezoelectric field has a value of $E=107$ kV/cm in the $Ga_{0.47}In_{0.53}As$ quantum-well layers. The energy-band diagram without the internal fields is indicated in Fig. 22(a) and the energy-band diagram with the internal fields is shown in Fig. 22(b). Comparison between Figs. 22(a) and 22(b) reveals that the internal piezoelectric fields substantially modify the energy-band diagram of the superlattice. As a result, the presence of internal strain-induced piezoelectric fields changes the energy levels and wave functions and therefore significantly modifies the electronic structure and optical properties of the superlattices.

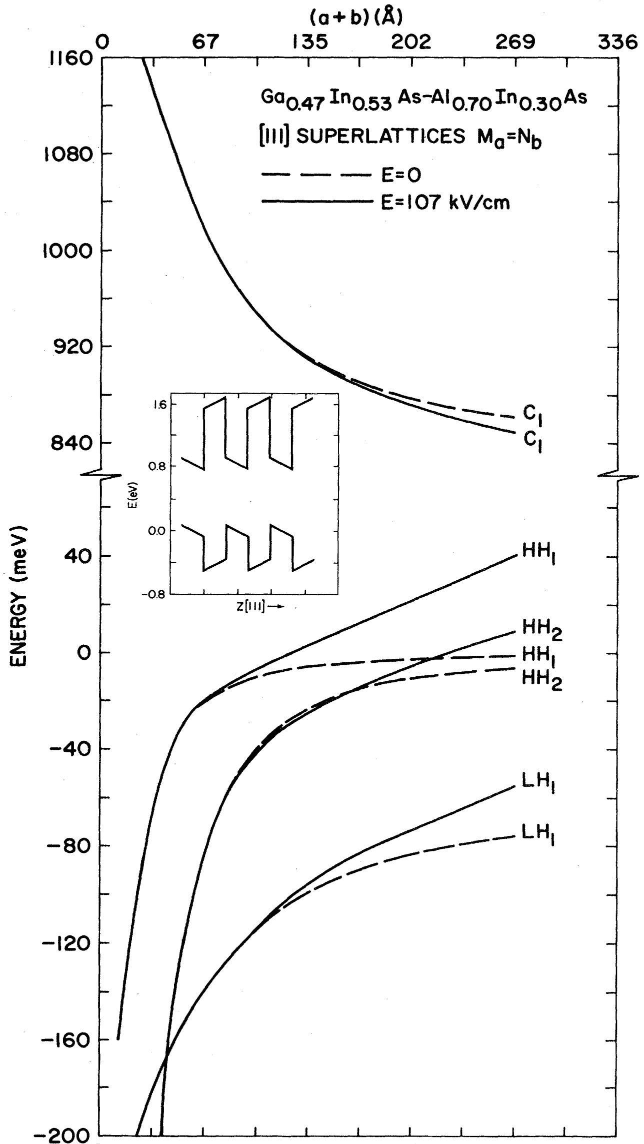

FIG. 23. Energy of zone-center subband levels as a function of superlattice layer thickness for a [111]-growth-axis strained-layer superlattice consisting of M_a layers of $Ga_{0.47}In_{0.53}As$ alternating with N_b layers of $Al_{0.70}In_{0.30}As$ ($N_b/M_a=1$). Calculations are performed with (solid lines) and without (dashed lines) the effects of strain-induced electric fields. Only the superlattice subbands HH_1, HH_2, LH_1, and C_1 are shown. The inset shows the energy-band diagram of the superlattice in the presence of strain-induced electric fields.

In Fig. 23 we show the energy position of the subband levels C_1, HH_1, HH_2, and LH_1 at the center of the superlattice Brillouin zone as a function of superlattice layer thickness for superlattices whose primitive cells contain an equal number of $Ga_{0.47}In_{0.53}As$ (M_a) and $Al_{0.70}In_{0.30}As$ (N_b) layers ($M_a=N_b$). An electric field of 107 kV/cm is induced in each material by the strain. Results are shown both including the strain-induced electric fields and neglecting them. The zero of energy is taken at the valence-band maximum of the strained (biaxial compression) bulk $Ga_{0.47}In_{0.53}As$ alloy at the center of the $Ga_{0.47}In_{0.53}As$ layer. The energy zero, the magnitude of the strain components, and the magnitude of the strain-induced electric field do not change as the superlattice layer thickness is varied.

Figure 23 indicates that Stark shifts are larger for heavier particles. The Stark shifts for the heavy-hole subbands HH_1 and HH_2 have different signs at small thicknesses. These two observations are consistent with a second-order perturbation-theory treatment of the Stark shifts on the bound states of a quantum well. Due to the sign of the energy denominator, the ground-state levels ($n=1$) are Stark-shifted down (towards the bottom of the quantum well), whereas the excited states ($n>1$) are pushed up (away from the bottom of the quantum well) by interaction with the strain-induced internal electric field. Also in agreement with a second-order perturbation analysis is the result that the magnitude of the Stark shift is larger for the $n=1$ ground-state subband levels than for the $n>1$ excited-state subband levels.

The magnitude of the Stark shift increases with superlattice layer thickness, as is clearly shown in Fig. 23. This increase with superlattice layer thickness has its origin in the fact that, for a constant value of the strain-induced electric field, the electrostatic potential drop across the superlattice layers increases linearly with the thickness of the layers. At large superlattice thicknesses, the electrostatic energy (strain-induced electric field times layer thickness) is larger than the confinement energies, and the results derived from a perturbation-theory treatment are no longer applicable. This is seen in Fig. 23 as the sign of the Stark shifts on the heavy-hole subbands HH_1 and HH_2 becomes the same at large superlattice periods [$(M_a+N_b)=2M_a>50$ layers].

We now consider the case in which the confining layers are stressed under biaxial tension due to a lattice mismatch of 0.8%. Figure 24 shows the energy-band diagram of a [111]-oriented strained-layer superlattice consisting of $M_a=20$ layers of $Ga_{0.47}In_{0.53}As$ (quantum wells) alternating with $N_b=3$ $M_a=60$ layers of $Al_{0.36}In_{0.64}As$ (barriers). The valence-band offset has a value of 129 meV. As a result of the lattice mismatch,

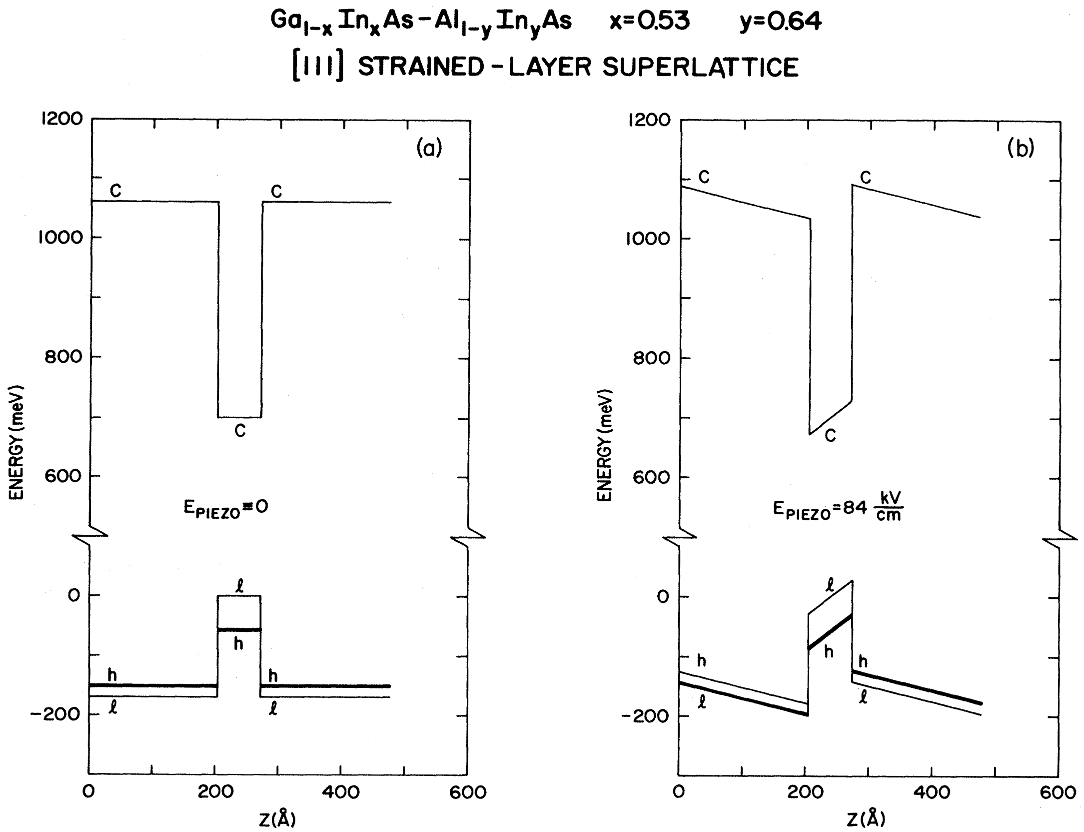

FIG. 24. Energy-band diagram of a [111]-oriented strained-layer superlattice consisting of $M_a=20$ layers of $Ga_{0.47}In_{0.53}As$ (quantum wells) alternating with $N_b=3\ M_a=60$ layers of $Al_{0.36}In_{0.64}As$ (barriers): (a) energy-band diagram without the internal piezoelectric fields; (b) energy-band diagram with the internal piezoelectric fields. The internal piezoelectric field has a value of $E=84$ kV/cm in the $Ga_{0.47}In_{0.53}As$ quantum-well layers. The labels *c*, *l*, and *h* identify the conduction, light-hole, and heavy-hole band edges, respectively, at the center of the bulk Brillouin zone. The zero of energy is the valence-band maximum at the center of the strained $Ga_{0.47}In_{0.53}As$ quantum wells.

strain-induced internal piezoelectric fields are present within the layers. The internal piezoelectric field has a value of $E=84$ kV/cm in the $Ga_{0.47}In_{0.53}As$ quantum-well layers. The energy-band diagram without the internal fields is indicated in Fig. 24(a) and the energy-band diagram with the internal fields is shown in Fig. 24(b). Comparison between Figs. 24(a) and 24(b) reveals that the internal piezoelectric fields substantially modify the energy-band diagram of the superlattice. As a result, the presence of internal strain-induced piezoelectric fields changes the energy levels and wave functions and therefore significantly modifies the electronic structure and optical properties of the superlattices.

Figure 25 shows the energy position of the subband levels C_1, HH_1, HH_2, and LH_1 at the center of the superlattice Brillouin zone as a function of superlattice layer thickness for superlattices whose primitive cells contain three times as many $Al_{0.36}In_{0.64}As$ layers as $Ga_{0.47}In_{0.53}As$ layers ($N_b=3M_a$). An electric field of 84 kV/cm is induced in the thinner-layer material (quantum wells) and a field one-third of this value is induced in the thicker-layer material (barriers). Results are shown both including the strain-induced pizeoelectric fields and neglecting them. The zero of energy coincides with the valence-band maximum of the strained (biaxial tension) bulk $Ga_{0.47}In_{0.53}As$ alloy at the center of the $Ga_{0.47}In_{0.53}As$ layers. A LH_1-HH_1 strain-induced reversal occurs for a superlattice layer thickness greater than approximately $(M_a+N_b)=4M_a>50$ layers. The position of this strain-induced LH_1-HH_1 crossing is weakly dependent on the presence of strain-induced piezoelectric fields, as can be seen by inspection of Fig. 25. Again, heavier particles are more strongly perturbed by the presence of strain-induced piezoelectric fields than are lighter ones, as can be seen by comparing the Stark shifts on the subbands LH_1, C_1, and HH_1.

An illustration of the effects of strain-induced piezoelectric fields on the superlattice wave functions is provided in Fig. 26, where the coarse-grain averaged charge densities associated with the zone-center ($\mathbf{k}_{\parallel}=0$; $Q=0$) states C_1, HH_1, HH_2, and LH_1 are plotted along the [111] growth axis. The superlattice consists of 24 layers of $Ga_{0.47}In_{0.53}As$ alternating with 24 layers of $Ga_{0.70}In_{0.30}As$ grown along the [111] axis (see Fig. 23). Results including and neglecting the strain-induced electric field are compared. The electric field displaces the carrier wave functions in space. The effect is larger for the heavy-hole subbands than for the electron or light-hole subbands owing to the larger effective mass of the heavy hole. The spatial displacement of the electron and hole wave functions leads to a carrier-generated electric field opposing the strain-induced field if both types of carriers are present owing, for example, to photoabsorption. The presence of either type of free carrier alone, owing, for example, to doping, will also lead to screening of the strain-induced field. The heavy holes are much more effective at screening the strain-induced fields than electrons. The extent of the screening depends on the density of electrons and holes. When the electrons and holes are generated by photoabsorption, the extent of screening and thus the photoabsorption profile becomes intensity dependent. Therefore the internal strain-induced electric fields lead to a nonlinear optical response.

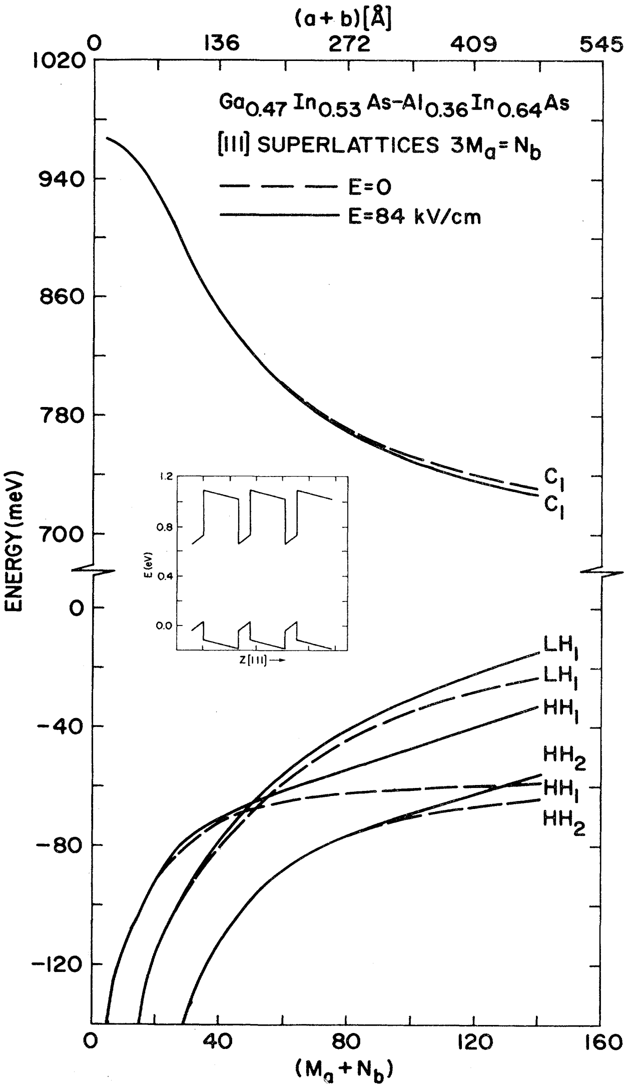

FIG. 25. Energy of zone-center subband levels as a function of superlattice layer thickness for a [111]-growth-axis strained-layer superlattice consisting of M_a layers of $Ga_{0.47}In_{0.53}As$ alternating with N_b layers of $Al_{0.36}In_{0.64}As$ ($N_b/M_a=3$). Calculations are performed with (solid lines) and without (dashed lines) the effects of strain-induced electric fields. Only the superlattice subbands HH_1, HH_2, LH_1, and C_1 are shown. The inset shows the energy-band diagram of the superlattice in the presence of strain-induced electric fields.

E. Optical properties of III-V semiconductor superlattices

In this section we discuss the optical properties of superlattices grown from III-V zinc-blende-structure semiconductors. We consider first lattice-matched superlattices and then we treat strained-layer superlattices. The calculations presented below are performed within the $\mathbf{k}\cdot\mathbf{p}$ formalism.

We have performed calculations of the optical matrix elements at the center of the superlattice Brillouin zone ($\mathbf{k}_{\parallel}=0$; $Q=0$). We calculate the optical matrix elements to zeroth order,

$$\langle n_i|\mathbf{p}|n_{i'}\rangle = \sum_{d,d'} \langle u_d|\mathbf{p}|u_{d'}\rangle \int_{-a}^{b} dz [F_d^{n_i}(z)]^* F_{d'}^{n_{i'}}(z) , \tag{3.23}$$

where the sums run over the eight bulk zone-center basis states belonging to the irreducible representations Γ_7, Γ_8, and Γ_6 of the T_d double group (Mailhiot and Smith, 1986a; Smith and Mailhiot, 1986). We display below the squared optical matrix elements defined as

$$\sum_{ii'} \frac{2}{m} |\langle n_i|\mathbf{p}\cdot\hat{\varepsilon}|n_{i'}\rangle|^2 , \tag{3.24}$$

where $|n_i\rangle$ are superlattice zone-center eigenstates, the sum on i is over the degenerate pair of eigenstates, and $\hat{\varepsilon}$ is a unit polarization vector.

In the following discussion we examine the differences in optical properties of [001]- and [111]-oriented superlattices. In the case of lattice-matched systems, it is found that [001]- and [111]-oriented superlattices have qualitatively similar optical properties. However, the optical response of [111]-growth-axis strained-layer superlattices is qualitatively different from that of [001]-oriented superlattices. These differences arise because of the presence of large internal piezoelectric fields within the layers of [111]-oriented strained-layer superlattices. These fields are absent in [001]-oriented superlattices.

We first consider the optical properties of [001]- and [111]-growth-axis lattice-matched superlattices. Recently, $GaAs/Ga_{0.70}Al_{0.30}As$ lattice-matched superlattices have been grown along the [001] and [111] orientation (Hayakawa, Takahashi, *et al.*, 1988a, 1988b). It has been demonstrated that [111]-oriented $GaAs/Ga_{0.70}Al_{0.30}As$

quantum-well lasers can exhibit better characteristics than conventional [001]-oriented quantum-well lasers (Hayakawa, Suyama, *et al.*, 1988). In Figs. 27 and 28 we show the electronic structure of a [001]- and a [111]-growth-axis GaAs/$Ga_{0.70}Al_{0.30}As$ superlattice, respectively. In both cases, the energy dispersions of the hole subbands HH_1, HH_2, HH_3, LH_1 and electron subbands C_1, C_2, C_3 are shown. The [001]-oriented superlattice (Fig. 27) consists of 35 layers of GaAs. The [111]-oriented superlattice (Fig. 28) consists of 27 layers of GaAs. These layer thicknesses correspond to the experimental situation reported by Hayakawa, Takahashi, *et al.* (1988a). The $Ga_{0.70}Al_{0.30}As$ barriers are sufficiently thick that the results corresponding to isolated quantum wells and the superlattice subbands exhibit essentially no dispersion along the superlattice growth axis.

Calculations of optical absorption coefficients for [111]- and [001]-oriented GaAs/$Ga_{0.7}Al_{0.3}As$ superlattices are shown in Fig. 29. The calculated optical absorption spectra shown in Fig. 29 are in good correspondence with the experimental measurements of these spectra by Hayakawa, Takahashi, *et al.* (1988a). In both, spectra, the three absorption lines correspond to HH_1-C_1, LH_1-C_1, and HH_2-C_2 transitions in order of increasing photon energy. The oscillator strengths of the corresponding transitions are similar in the two spectra. The principal difference is the magnitude of the energy splitting be-

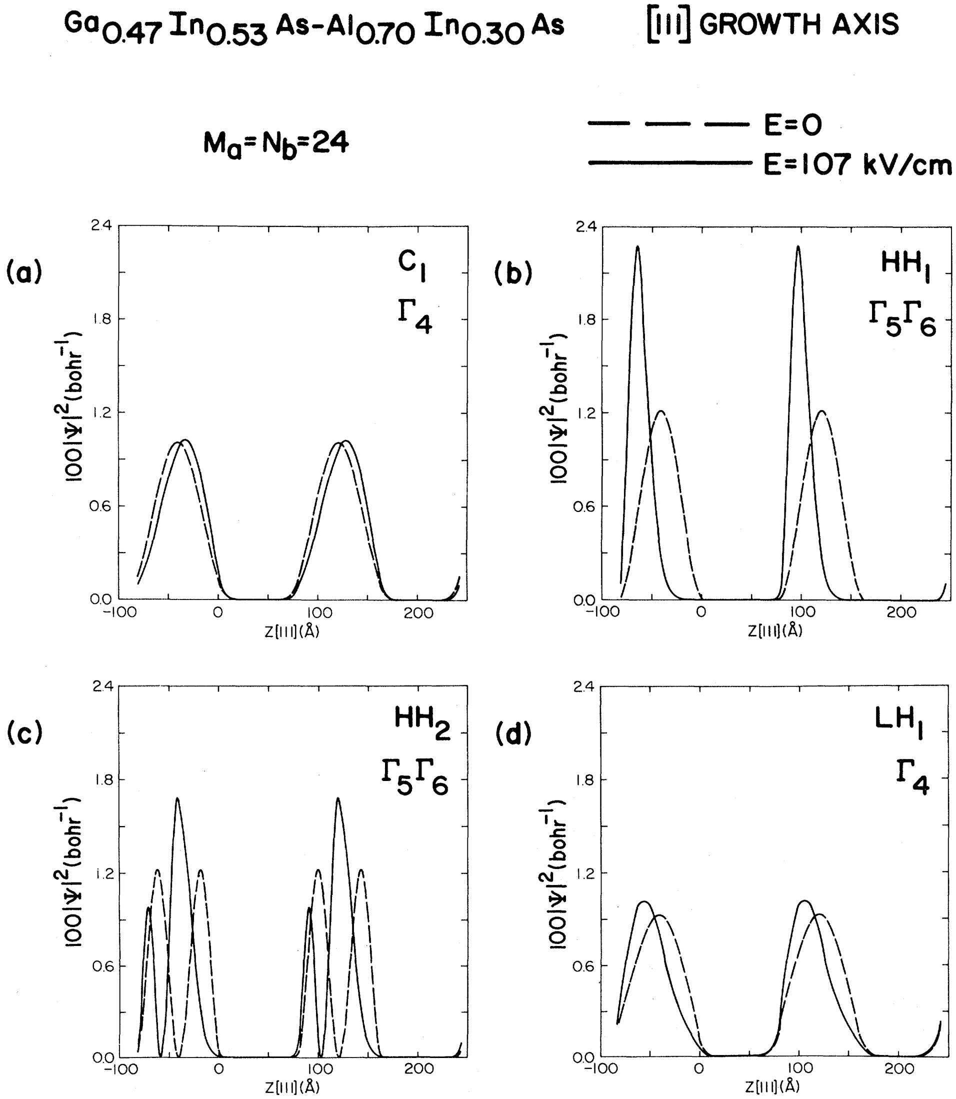

FIG. 26. Electronic charge densities for a [111]-growth-axis strained-layer superlattice consisting of 24 layers of $Ga_{0.47}In_{0.53}As$ alternating with 24 layers of $Al_{0.70}In_{0.30}As$: (a) first conduction state C_1; (b) first heavy-hole state HH_1; (c) second heavy-hole state HH_2; (d) first light-hole state LH_1. Calculations are performed with (solid lines) and without (dashed lines) the effects of strain-induced piezoelectric fields.

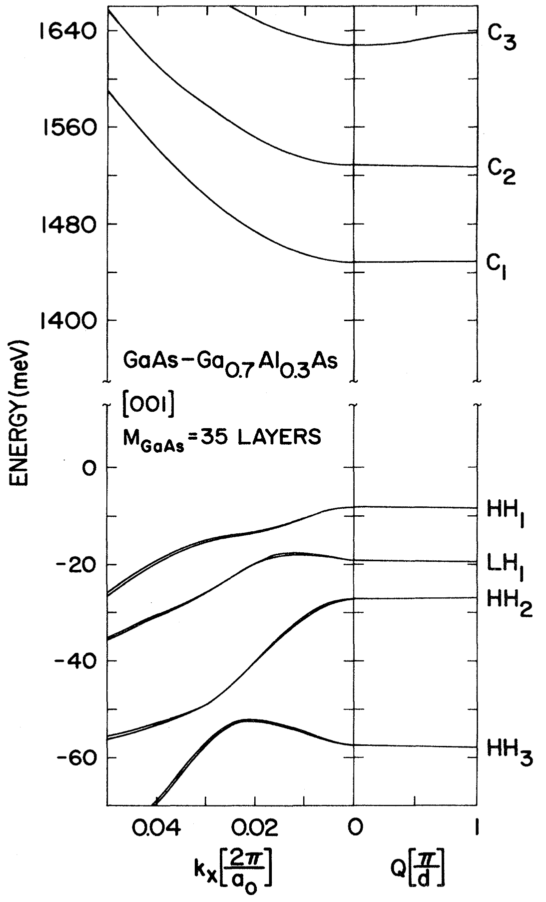

FIG. 27. Electronic energy-band structure of a [001]-growth-axis GaAs/Ga$_{0.7}$Al$_{0.3}$As quantum well consisting of 35 layers of GaAs. The energy zero coincides with the GaAs valence-band maximum.

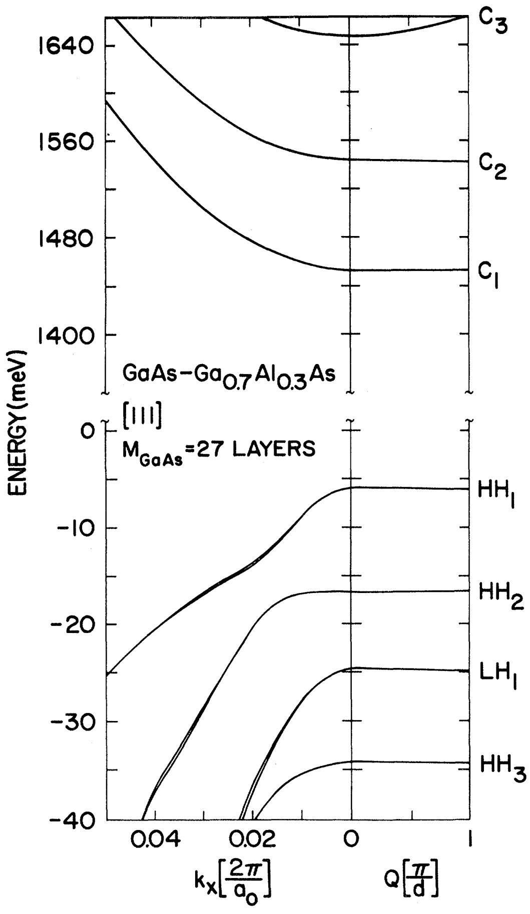

FIG. 28. Electronic energy-band structure of a [111]-growth-axis GaAs/Ga$_{0.7}$Al$_{0.3}$As quantum well consisting of 27 layers of GaAs. The energy zero coincides with the GaAs valence-band maximum.

tween the HH$_1$-C$_1$ and LH$_1$-C$_1$ transitions. The anisotropy of the bulk heavy-hole masses is responsible for this observed difference in energy splitting.

For [001]-growth-axis superlattices, the presence of internal strain does not change qualitatively the optical properties from those seen for lattice-matched superlattices. Consequently, [001]-oriented strained-layer superlattices are expected to exhibit optical properties similar to those of [001]-oriented lattice-matched superlattices. However, in the case of strained-layer superlattices grown along the [111] axis, the presence of internal strain generates large piezoelectric fields. As discussed in Sec. III.D, these internal piezoelectric fields change the energy levels and wave functions of the [111]-oriented strained-layer superlattice. Consequently the optical response of a [111]-growth-axis strained-layer superlattice is qualitatively different from that of a [111] lattice-matched superlattice. In the analysis presented below, we concentrate on the novel optical properties that arise because of the presence of internal piezoelectric fields in [111]-growth-axis strained-layer superlattices. Of particular interest is the fact that these internal piezoelectric fields can be modulated by an external perturbation. Examples of field modulations include screening by photogenerated free carriers, an external electrical bias, or an external stress. These modulations lead to nonlinear optical responses and electro-optical and piezo-optical effects.

A strain-induced internal electric field can significantly change the optical properties of the superlattices. We consider superlattices made from Ga$_{0.47}$In$_{0.53}$As/Al$_{0.70}$In$_{0.30}$As, with the Ga-containing alloy layers half as thick as the Al alloy layers. The lattice-constant mismatch is 1.5%. The strain-induced electric field is 1.4×10^5 V/cm in the Ga alloy and half this value in the Al alloy. As seen in the previous section, both electronic energy levels and wave functions are changed by the internal electric fields. The changes in the wave function lead to changes in optical matrix elements and to a screening of the electric fields by photogenerated

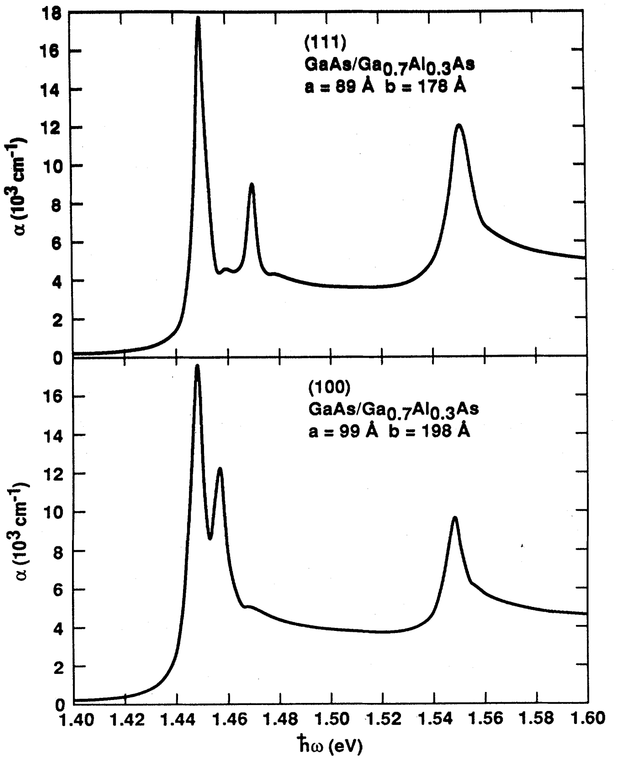

FIG. 29. Optical absorption coefficients for [111]-oriented (top) and [001]-oriented (bottom) lattice-matched GaAs/$Ga_{0.7}Al_{0.3}As$ quantum wells. The electronic energy-band structure of the [001]-oriented quantum well is shown in Fig. 25 and that of the [111]-oriented quantum well is shown in Fig. 26.

electron-hole pairs.

In Fig. 30 we show the effect of the electric fields on electronic energy levels, optical matrix elements, and the dipole moment of an electron-hole pair for the superlattice described above. Figure 30(a) shows the zone-center energy levels of the lowest conduction band and the highest three heavy-hole and highest light-hole energy levels as a function of the superlattice repeat distance (keeping the well-to-barrier length ratio fixed), including and neglecting the electric fields. The fields shift the conduction-band state to lower energy and the valence band to higher energy, thus reducing the band gap. The effect is larger for thicker-layer superlattices and, at a given thickness, is larger for heavy holes than for electrons or light holes. The light-hold bands are split away from the heavy-hole bands by strain. Therefore band-edge optical properties will be dominated by heavy-hole to conduction-band transitions.

In Fig. 30(b) we show the squared optical matrix elements for the first three heavy-hole to conduction-band transitions (labeled HH_j-C_1, $j=1,2,3$) as a function of the internal electric field in the Ga alloy. The superlattice consists of 25 molecular layers of the Ga alloy alternating with 50 molecular layers of the Al alloy. (We refer to this as a 25/50 superlattice.) The light polarization is in the plane of the superlattice interfaces. The maximum field shown (E_0) is the unscreened value of the internal strain-induced field. The HH_1-C_1 transition, which is strongly allowed at zero field, is suppressed by the internal fields. The HH_2-C_1 and HH_3-C_1 transitions are very weak at zero field. The internal fields increase the strength of these transitions so that, at the unscreened value of the fields, the three transitions have comparable oscillator strength.

We now consider the screening polarization fields originating from the spatial separation of free carriers along the [111] growth axis of the strained-layer superlattice. In order to determine the screening polarization field arising from the field-induced spatial separation of carriers within the $Ga_{0.47}In_{0.53}As$ confining layers, we calculate the field-dependent polarization length in quantum wells of thickness a:

$$I_n^{n'}(E)=\int_{-a}^{0} dz\,(z+a/2)\sum_{d}\left(|F_d^n(z)|^2-|F_d^{n'}(z)|^2\right), \tag{3.25}$$

where $F_d^n(z)$ are the superlattice envelope functions, the superscripts n,n' refer to subband indices, and the integration is over the $Ga_{0.47}In_{0.53}As$ layer. The coordinate z is along the [111] growth axis.

The heavy-hole-to-conduction screening polarization field is proportional to $I_{\rm HH}^{\rm C}(E)$ is given by

$$P_{\rm screen}(n,E)=n\frac{a+b}{a}eI_{{\rm HH}_1}^{{\rm C}_1}(E), \tag{3.26}$$

where n is the free-carrier density, $a+b$ is the superlattice period, and e is the electronic charge. The electric field dependence of $P_{\rm screen}$ is included in the polarization length $I_{{\rm HH}_1}^{{\rm C}_1}(E)$. The magnitude of $P_{\rm screen}(n,E)$ increases with electric field strength and superlattice layer thickness. For a given electric field strength, the spatial separation of electrons and holes along the [111] axis is limited by the thickness of the quantum wells. As the width of the $Ga_{0.47}In_{0.53}As$ layers increases, so does the screening polarization length.

In Fig. 30(c) we show the screening polarization length of an electron-hole pair for HH_j-C_1 ($j=1,2,3$) electron-hole pair states as a function of the internal field in the Ga alloy. This screening length is the length of the dipole moment of an electron-hole pair in the indicated quantum states and electric field. The negative sign in Fig. 30(c) indicates a dipole moment that opposes the strain-generated internal field. The screened field in the quantum well is given by

$$E\left[1-\frac{P_{\rm screen}(E)}{\kappa E}\right]=E_0, \tag{3.27}$$

where $P_{\rm screen}(E)$ is defined in Eq. (3.26) and κ is the static dielectric constant in the quantum well. To reduce the unscreened internal field by 10% for the superlattice requires a density of 1.2×10^{17} cm^{-3} electron-hole pairs (holes in the HH_1 state). The screening is predominantly from distortion of the hole wave function.

Because the internal electric fields charge the superlattice energy levels and wave functions, they change the superlattice optical properties. We consider the 25/50 superlattice and present calculations of the resonant contribution to the susceptibility from near-band-edge transitions. Transitions from the first three heavy-hole bands to the lowest conduction band are included. [Transitions from the light-hole bands occur at higher energy; see Fig. 30(a).] The effect of the internal electric fields on the exciton binding energies and wave functions are included, but they are rather small (Brum and Bastard, 1985). A scattering time (T_2), which gives a FWHM of 5 meV, is included.

In Fig. 31 we show the calculated real and imaginary parts of the resonant susceptibility as a function of photon energy for three values of the internal fields: the unscreened value, half the unscreened value, and zero field. At zero field, HH_1-C_1 transitions dominate the spectrum; there is a strong exciton transition and an electron-hole continuum. A small HH_3-C_1 exciton transition is superposed on the HH_1-C_1 continuum. The HH_2-C_1 transitions are too weak to show up. As the internal fields increase, the HH_1-C_1 exciton moves to lower energy and loses oscillator strength. With increasing field, the HH_2-C_1 transitions are turned on. At the unscreened value of the fields, the HH_2-C_1 exciton is the strongest feature in the spectrum. It moves to lower energy with increasing field, but at a slower rate than the HH_1-C_1 exciton does. The HH_3-C_1 exciton gains oscillator strength with increasing field and moves to slightly higher energy.

As seen in Fig. 31, the internal, strain-generated electric fields can significantly change the optical properties of a [111]-growth-axis superlattice. These internal fields can be externally modulated. Here we consider modulation by across-the-band-gap optical absorption. The electron-hole pairs formed by this absorption process screen, and thus reduce, the magnitude of the internal fields. This screening effect gives the superlattice nonlinear optical properties. The size of the optical nonlinearity can be determined by calculating the susceptibility at two slightly different values of the internal fields and finding the carrier density and, hence, the absorbed intensity required to cause that shift in the internal electric fields. The holes will rapidly thermalize to the HH_1 band independent of where they were optically generated. Consequently we take the screening to be caused by HH_1-C_1 electron-hole pairs. We use a value of 10 ns for the electron-hole pair lifetime. The initial electric field is taken as the unscreened value.

In Fig. 32 we show real and imaginary parts of the nonlinear susceptibility χ^3 $(-\omega,\omega,\omega_0,-\omega_0)$ (Jha and Bloemberger, 1968) at a fixed pump frequency ω_0, as a function of probe frequency ω for a 20/40 and a 25/50

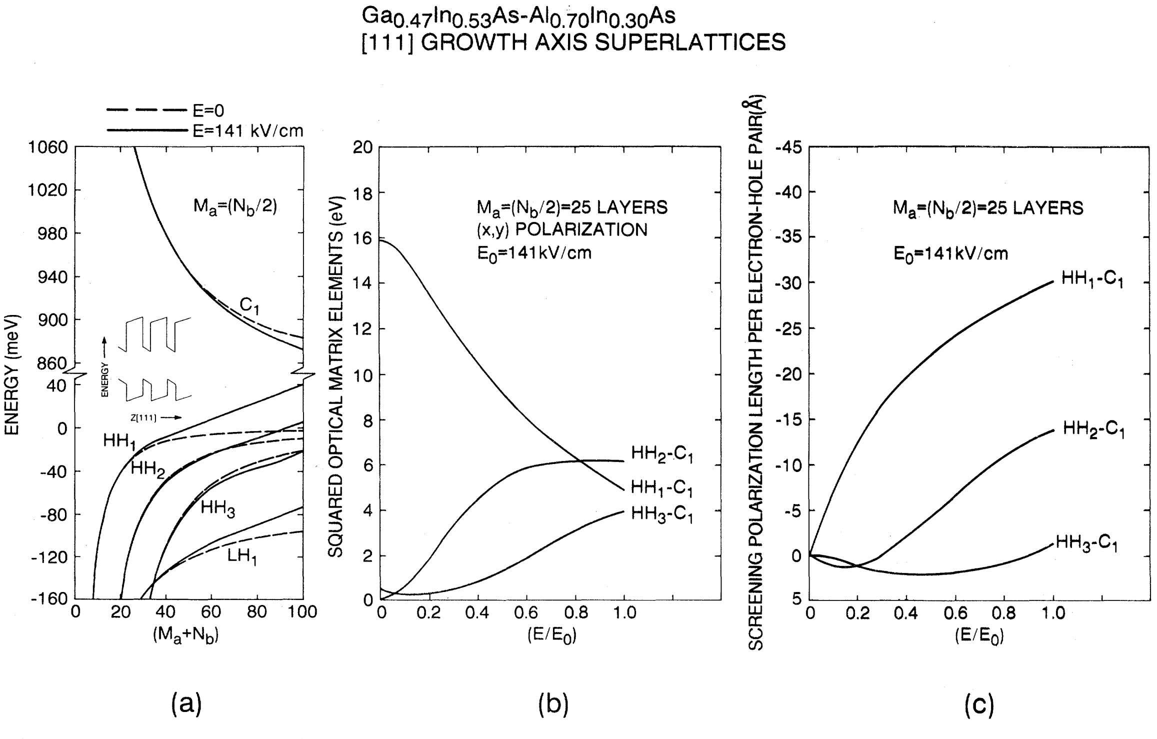

FIG. 30. $Ga_{0.47}In_{0.53}As/Al_{0.70}In_{0.30}As$ [111]-growth-axis superlattice characteristics: (a) superlattice energy levels as a function of repeat distance with (solid line) and without (dashed line) the internal fields; (b) the squared optical matrix elements as a function of the internal field strength for a 25/50 superlattice; (c) electron-hole pair dipole screening length as a function of the internal field strength for a 25/50 superlattice.

superlattice. Very strong features (~ 0.1 esu) occur near the HH_1-C_1 and HH_2-C_1 exciton transitions. Comparing line shapes in Fig. 31 [peak in $\mathrm{Re}(\chi^3)$, derivative of peak in $\mathrm{Im}(\chi^3)$] with Fig. 32, one sees that these features in χ^3 result primarily from shifting the exciton transition energy. The HH_2-C_1 nonlinearity is stronger than the HH_1-C_1 nonlinearity in the 25/50 superlattice, whereas the reverse is true for the 20/40 superlattice. This reversal occurs because the internal fields have caused the HH_2-C_1 oscillator strength to exceed the HH_1-C_1 oscillator strength at the unscreened value of the fields in the 25/50 superlattice. In the 20/40 superlattice, the HH_1-C_1 oscillator strength is larger at the unscreened fields. A smaller feature in χ^3 occurs near the HH_3-C_1 transition. From the line shape one sees that this nonlinearity results primarily from the exciton's oscillator strength changing with field.

We have seen that internal strain-induced electric fields can significantly change the electronic structure and optical properties of a superlattice. For example,

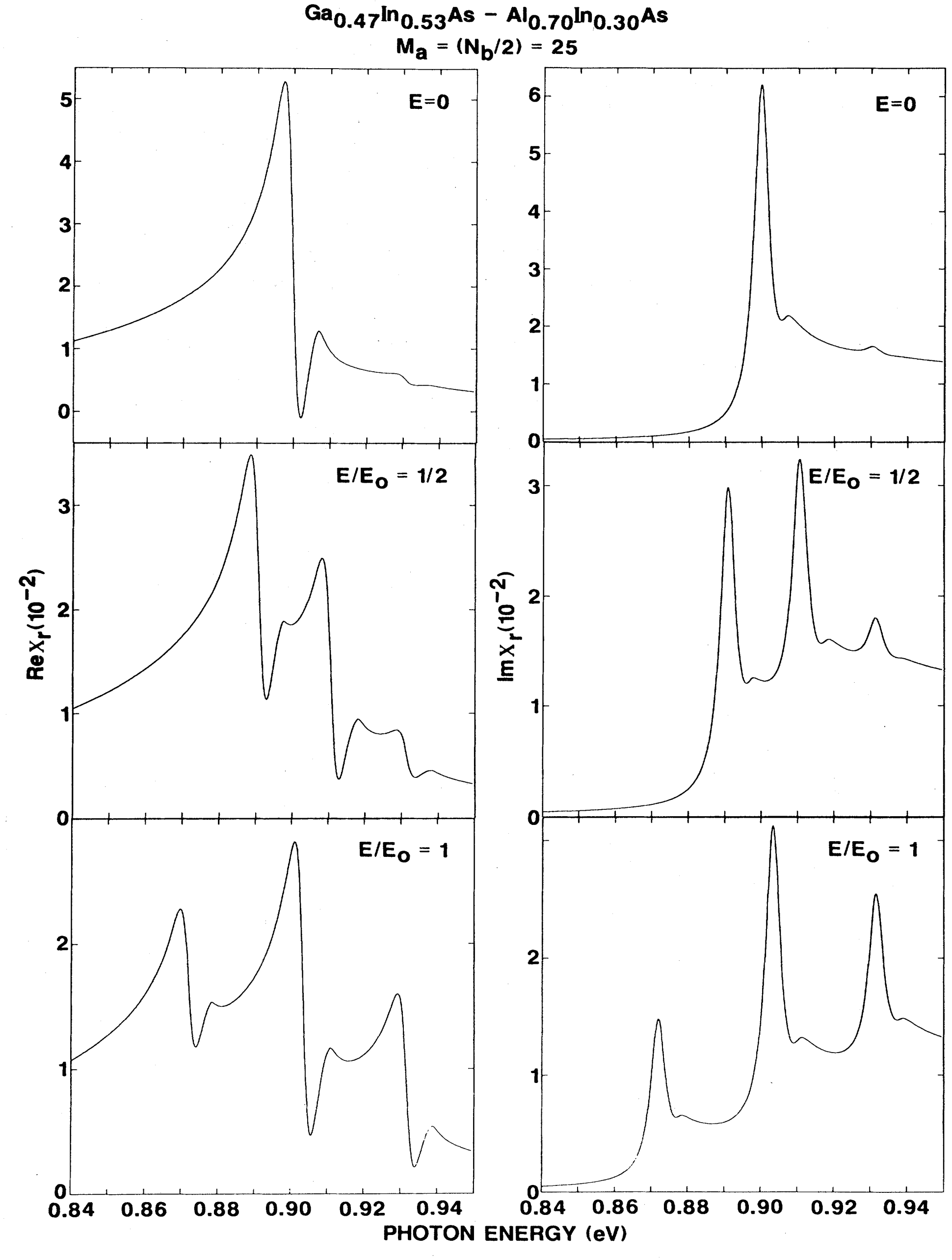

FIG. 31. The resonant susceptibility as a function of photon energy for three values of the internal field for a 25/50 superlattice: left, the real part; right, the imaginary part.

these fields change electronic energy levels and wave functions, and thus optical transition energies and oscillator strengths. As is usual with the Stark effect, these changes are second order in the magnitude of the electric field. Internal, strain-induced electric fields can be modulated by the application of an external electric field. The externally applied field will be essentially uniform, whereas the internal strain-induced electric field reverses polarity in the two constituent materials. Thus the total electric field is increased in one constituent material type and is decreased in the other. In type-I superlattices, the magnitude of the electric field in the confining quantum wells determines the response of the superlattice. If the magnitude of the external field is small compared with that of the internal field, changes in the superlattice electronic structure and optical properties due to the external field will be linear in the magnitude of the external field. This situation corresponds to a second-order effect (Stark effect) being modulated by the applied field about a large bias point because of the strain-generated internal fields. As a result, a linear electro-optic effect is expected in [111]-growth-axis strained-layer superlattices that have large internal electric fields, whereas a quadratic electro-optic effect is expected in [001]-growth-axis superlattices and in [111]-growth-axis lattice-matched superlattices in which those internal electric fields vanish.

We consider lattice-matched $Ga_{0.47}In_{0.53}As$/$Al_{0.48}In_{0.52}As$ and strained-layer $Ga_{0.47}In_{0.53}As$/$Al_{0.7}In_{0.3}As$ superlattices grown along the [111] axis. The strained-layer superlattice has internal electric fields, and the lattice-matched superlattice does not. A [001]-growth-axis superlattice (strained-layer or lattice-matched) would not have internal fields and would be qualitatively similar to the lattice-matched [111] case. We consider superlattices in which the Ga-containing alloy layers are half as thick as the Al alloy layers. Both the lattice-matched and the strained-layer cases are type-I superlattices in which the Ga alloy is the quantum well.

In Fig. 33 the variation of the HH_1-C_1 transition energy at the center of the superlattice Brillouin zone is shown as a function of the magnitude of the externally applied electric field. The external electric field is applied along the [111] growth axis and has the same sign as the internal strain-induced field in the Ga-alloy quantum well. Results are shown for various layer thicknesses. For the lattice-matched superlattice, the external field decreases the transition energy. The effect is greater for

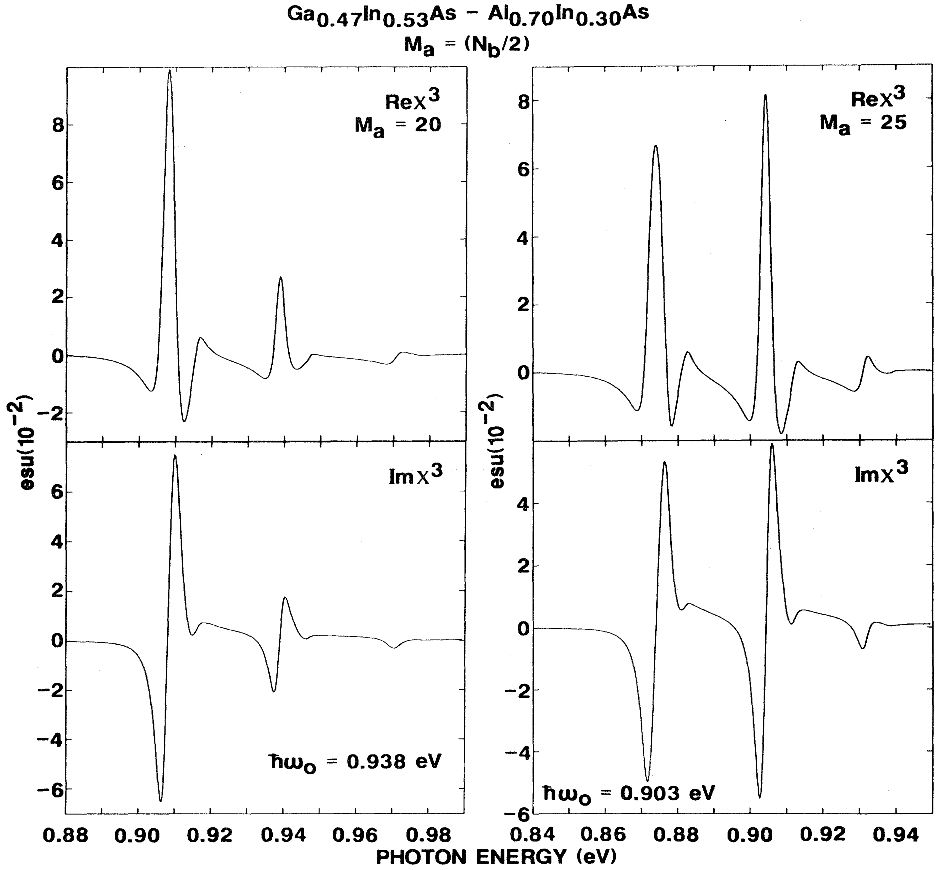

FIG. 32. χ^3 as a function of probe frequency (ω) for fixed pump frequency (ω_0) in 20/40 (left) and 25/50 (right) superlattices: top, the real part; bottom, the imaginary part.

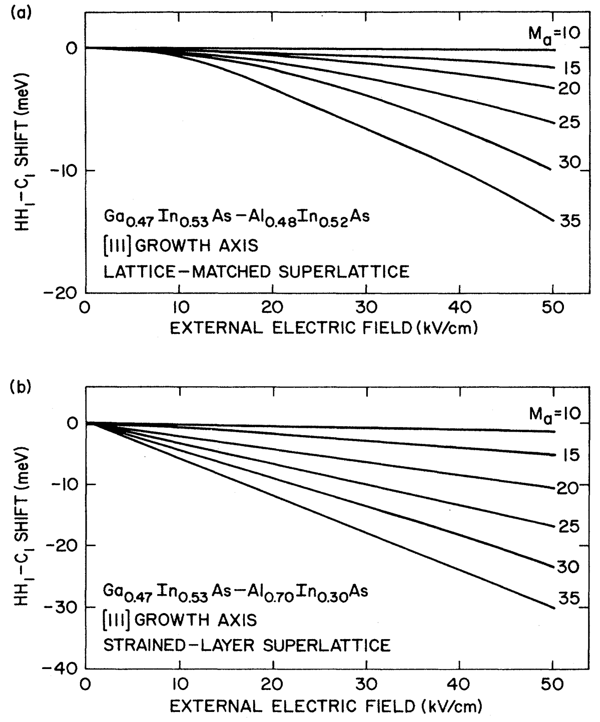

FIG. 33. Variation of the HH_1-C_1 transition energy as a function of the magnitude of the applied field for $Ga_{1-x}In_xAs/Al_{1-y}In_yAs$ superlattices grown along the [111] axis: (a) $x=0.53, y=0.52$; (b) $x=0.53, y=0.30$. The superlattice consists of M_a layers of $Ga_{1-x}In_xAs$ (wells) alternating with $N_b=2M_a$ layers of $Al_{1-y}In_yAs$ (barriers).

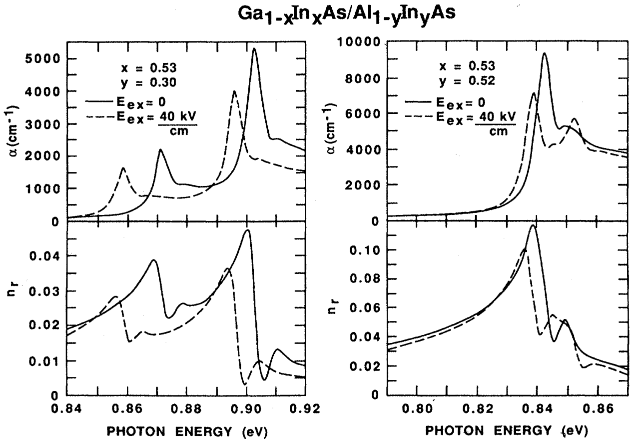

FIG. 34. Absorption coefficient and resonant part of the refractive index with and without an applied electric field as a function of photon energy for $(M_a=25)/(N_b=50)$ strained-layer and lattice-matched superlattices.

thick-layer superlattices. The decrease in transition energy is essentially quadratic with the magnitude of the applied field. The sign of the applied field is not important for the lattice-matched superlattice. For the strained-layer superlattice, the external field adds to the internal strain-induced electric field in the quantum well and decreases the transition energy. The effect is greater for thick-layer superlattices. The decrease in transition energy is essentially *linear* with the magnitude of the applied field and is much greater than for the lattice-matched superlattice. The sign of the applied field is important for the strained-layer superlattice; for the opposite polarity to that shown in Fig. 33 the transitions will shift to higher energy.

In Fig. 34 we show calculations of the absorption coefficient and the resonant contribution to the real part of the refractive index as a function of photon energy for strained-layer and lattice-matched superlattices with 25 molecular layers of the Ga alloy and 50 molecular layers of the Al alloy. Results are shown with no applied electric field and with an applied electric field of 40 kV/cm. Transitions from the first two heavy-hole bands to the lowest conduction band are included. Other transitions occur outside of the energy range shown. Exciton effects are included in these optical calculations. A scattering time (T_2) that gives a FWHM of 6 meV was used. For the lattice-matched superlattice, the HH_1-C_1 transition strongly dominates the spectra with no applied field. The HH_2-C_1 transition is very weak in this case. As the external field is applied, the HH_1-C_1 transition moves to lower energy and loses oscillator strength, whereas the HH_2-C_1 transition stays approximately constant in energy and gains oscillator strength. For the strained-layer superlattice, the HH_1-C_1 and HH_2-C_1 transitions are both fairly strong with no applied field. The internal field has caused the HH_2-C_1 transition to be strongly allowed. Indeed, it is even stronger than the HH_1-C_1 transition. As the external field is applied (the applied electric field has the same sign as the internal field in the Ga-alloy quantum well), both the HH_1-C_1 and HH_2-C_1 transitions move to lower energy. The shift is larger for the HH_1-C_1 transition. Both transitions lose oscillator strength, which is transferred to higher-energy transitions.

In Fig. 35 we show calculated electro-optic coefficients

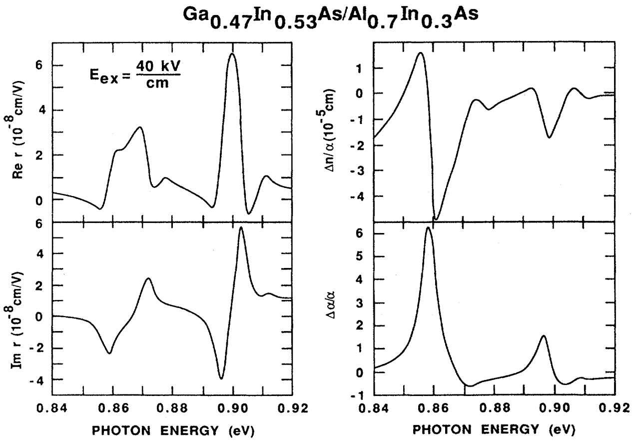

FIG. 35. Electro-optic coefficients as a function of photon energy for the $(M_a=25)/(N_b=50)$ strained-layer superlattice.

for the strained-layer superlattice described above. The coefficient r is defined by

$$n(E)-n(0)=\frac{-|n(0)|^3 rE}{2}\ , \tag{3.28}$$

where n is the index of refraction and E is the applied field. The index-of-refraction calculations in Fig. 34 were used to determine the electro-optic coefficients presented in Fig. 35. The total index of refraction, which appears in Eq. (3.25), consists of the field-dependent, resonant part shown in Fig. 34 plus a field-independent, nonresonant part. We get the nonresonant part by averaging the nonresonant indices of refraction of the superlattice constituent materials. For many electro-optic applications, the change in refractive index or absorption coefficient divided by the zero-field absorption coefficient is an important figure of merit. Therefore in Fig. 35 we also show

$$\Delta n/a=\frac{n(E)-n(0)}{a(0)} \tag{3.29a}$$

and

$$\Delta a/a=\frac{a(E)-a(0)}{a(0)} \tag{3.29b}$$

for $E=40$ kV/cm as a function of photon energy. The coefficients plotted in Fig. 35 reach very large values. For comparison, in potassium dihydrogen phosphate (KDP) the coefficient r is about 10^{-9} cm/V (Kaminow and Turner, 1971).

F. Effects of external uniaxial stress

In this section we consider how the electronic structure and optical properties of semiconductor superlattices can be modulated by the application of an external uniaxial stress. We consider first [001]-growth-axis lattice-matched superlattices. We then consider [111]-oriented strained-layer superlattices. In the case of [001]-oriented lattice-matched superlattices, the variations of the electronic structure caused by the application of an external stress are due to deformation-potential effects. The application of an external stress on a [111]-oriented strained-layer superlattice causes changes in the electronic structure by a combination of two effects: deformation-potential effects and piezo-modulation of the internal polarization fields. For thin-layer superlattices, deformation-potential effects dominate. However, for thick-layer superlattices, the response of the superlattice to an external stress is dominated by the modulation of the internal piezoelectric fields.

We consider the effects of an applied compressive uniaxial stress on the electronic structure of GaAs/$\mathrm{Ga}_{1-x}\mathrm{Al}_x\mathrm{As}$ lattice-matched quantum wells grown along the [001] axis. We specifically consider the cases in which the uniaxial stress $\mathbf{X}$ is applied in a direction parallel ($\mathbf{X}\|[001]$) and perpendicular ($\mathbf{X}\|[100]$) to the [001] growth axis of the quantum well, which is chosen to coincide with the spin quantization axis. In contrast with bulk behavior, strain-induced energy shifts depend sensitively on whether the external compressive stress is applied along the [001] or [100] axis. For a stress applied perpendicular to the quantum-well growth axis, the heavy- and light-hole quantum-well states are admixed by the strain Hamiltonian. Consequently, the transition energies associated with the heavy- and light-hole quantum-well states are nonlinear functions of the magnitude of the applied stress and exhibit a behavior that depends on the thickness of the GaAs quantum well. However, for a stress applied in a direction parallel to the quantum-well growth axis, only the transition energies associated with the light-hole quantum-well states show a strong nonlinear behavior as a function of the applied stress, because the strain Hamiltonian does not admix the heavy- and light-hole states.

We consider alloy composition $x=0.30$ and superlattices in which the $\mathrm{Ga}_{1-x}\mathrm{Al}_x\mathrm{As}$ layers are sufficiently thick so that the GaAs quantum wells are isolated. We analyze the strain-induced zone-center ($\mathbf{k}_\|=\mathbf{0}$) energy shifts of the heavy-hole (HH_1-C_1, HH_2-C_1) and light-hole (LH_1-C_1) transitions as a function of the orientation and magnitude of the applied compressive stress. Exciton binding energies are fairly invariant with respect to the magnitude of the applied stress, and we neglect exciton effects in the analysis presented below. We consider, in turn, uniaxial stresses applied perpendicular ($\mathbf{X}\|[100]$) and parallel ($\mathbf{X}\|[001]$) to the [001] quantum-well growth axis. Strain interactions in the bulk states of GaAs and $\mathrm{Ga}_{1-x}\mathrm{Al}_x\mathrm{As}$ are well understood, so that no additional parameters are required in the analysis.

We quantize spin along the [001] quantum-well growth axis and denote its projection on the quantization axis by m_j. In the case of $\mathbf{X}\|[100]$, bulk light ($m_j=\pm\frac{1}{2}$) and heavy ($m_j=\pm\frac{3}{2}$) states are admixed by the applied stress. However, in the case of $\mathbf{X}\|[001]$, $|m_j|$ is a good quantum number for the bulk states, and bulk light ($m_j=\pm\frac{1}{2}$) and heavy ($m_j=\pm\frac{3}{2}$) states are not admixed by the applied stress. These interactions result in strain-induced transition energy shifts that are nonlinear functions of the magnitude of the applied compressive stress.

Figure 36 shows the zone-center ($\mathbf{k}_\|=\mathbf{0}$) strain-induced energy shifts for the transitions HH_1-C_1, LH_1-C_1 [panel (a)], and HH_2-C_1 [panel (b)] as a function of the magnitude of the compressive uniaxial stress applied perpendicular to the [001] growth axis, $\mathbf{X}\|[100]$. We consider GaAs quantum wells with thicknesses of 40, 110, and 220 Å and compare these with measurements of the strain-induced energy shifts in GaAs/$\mathrm{Ga}_{0.70}\mathrm{Al}_{0.30}\mathrm{As}$ quantum wells (Jagannath *et al.*, 1986). There is good agreement between the theoretical and experimental results shown in Fig. 36(a). For comparison purposes, the zone-center strain-induced energy shifts for the HH-C and LH-C transitions in bulk GaAs are also shown in Fig. 36.

Strain-induced energy shifts for the transition HH_2-C_1 are indicated in Fig. 36(b). Comparison between Figs.

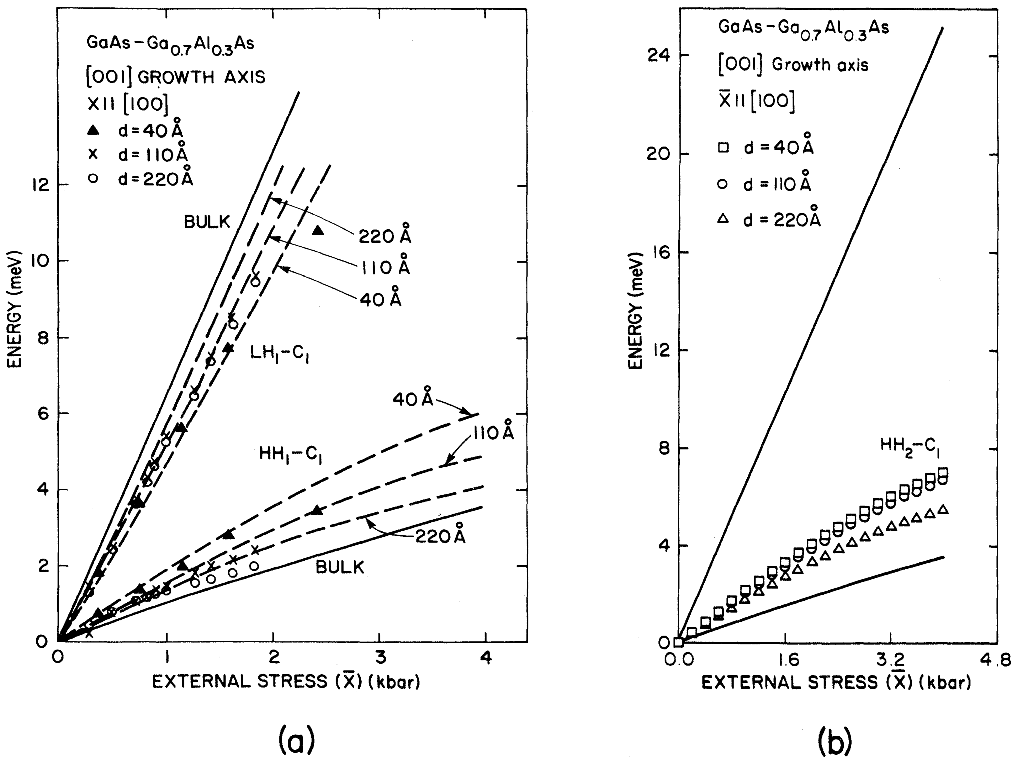

FIG. 36. Strain-induced transition energy shifts resulting from a compressive stress applied along the [100] axis of a GaAs/Ga$_{0.70}$Al$_{0.30}$As quantum well grown along the [001] axis: (a) measurements (Jagannath *et al.*, 1986) (symbols) and calculations (dashed lines) of the energy shifts for the transitions HH$_1$-C$_1$ and LH$_1$-C$_1$; (b) calculations of the energy shifts for the transition HH$_2$-C$_1$. The strain-induced transitions in bulk GaAs are indicated by the solid lines.

36(a) and 36(b) shows that the strain-induced energy shifts are larger for the transition HH$_2$-C$_1$ than for the transition HH$_1$-C$_1$, indicating that the transitions to excited states deviate more from the bulk GaAs behavior. However, the thickness dependence of the strain-induced energy shifts is weaker for the HH$_2$-C$_1$ transitions than for the HH$_1$-C$_1$ transitions.

The results for the zone-center ($\mathbf{k}_\parallel = \mathbf{0}$) strain-induced transition energy shifts for a compressive uniaxial stress applied parallel to the quantum-well growth axis, $\mathbf{X} \parallel [001]$, are indicated in Fig. 37. Again, the zone-center strain-induced energy shifts for bulk GaAs are also shown for comparison. Inspection of Fig. 37 indicates that when the compressive stress is applied parallel to the quantum growth axis, the LH$_1$-C$_1$ transition energy shifts are thickness dependent and strongly nonlinear, whereas the HH$_1$-C$_1$ and HH$_2$-C$_1$ transitions are virtually independent of the quantum-well width and are very nearly linear functions of the magnitude of the applied stress. For a stress applied in a direction parallel to the spin quantization axis, the bulk strain Hamiltonian does not admix states with different values of $|m_j|$. The nonlinear behavior shown in Fig. 37 for the LH$_1$-C$_1$ transition results from mixing by the strain Hamiltonian of the light-

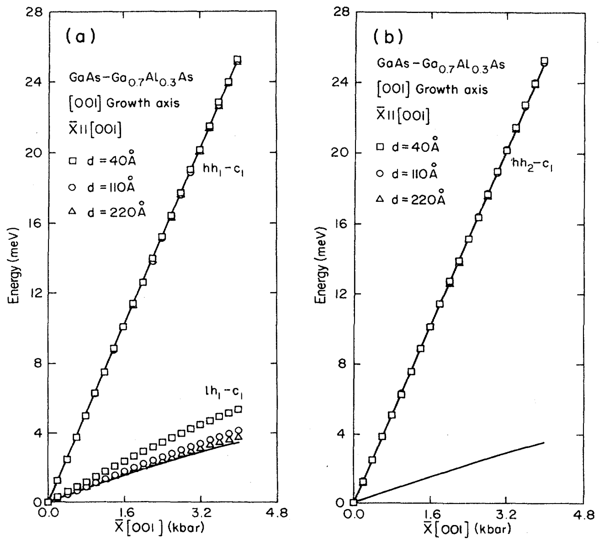

FIG. 37. Calculated strain-induced transition energy shifts resulting from a compressive stress applied along the [001] axis of a GaAs/Ga$_{0.70}$Al$_{0.30}$As quantum well grown along the [001] axis: (a) transitions HH$_1$-C$_1$ and LH$_1$-C$_1$; (b) transition HH$_2$-C$_1$. The strain-induced transitions in bulk GaAs are indicated by the solid lines.

hole states $|j=\frac{3}{2};\,m_j=\pm\frac{1}{2}\rangle$ and spin split-off states $|j=\frac{1}{2};\,m_j=\pm\frac{1}{2}\rangle$.

Comparison of Figs. 36 and 37 indicates that the strain-induced energy shifts are very different for the cases in which the compressive uniaxial stress is applied perpendicular ($\mathbf{X}\|[100]$) or parallel ($\mathbf{X}\|[001]$) to the quantum-well growth axis. These differences are a consequence of the mixing of the heavy- and light-hole states by the strain interactions. In the bulk, the distinction between the cases $\mathbf{X}\|[100]$ and $\mathbf{X}\|[001]$ is, of course, immaterial.

The application of an external uniaxial stress on a lattice-matched superlattice causes modifications of the electronic structure because of deformation-potential effects. An additional effect arises in [111]-growth-axis strained-layer superlattices, where the application of an external stress also causes a variation of the internal piezoelectric field. As a result, the electronic structure of a [111]-growth-axis strained-layer superlattice is modified by a combination of two effects: deformation-potential effects arise because of the variation of the internal strain, and Stark effects arise because the internal piezoelectric fields are modulated in accordance to the strain variations.

The application of an external stress on the substrate of a superlattice induces variations of the internal strains in the constituent semiconductors. Let ε_l^i be the internal strain tensor in semiconductor i arising from lattice mismatch at the superlattice interfaces. (For a lattice-matched superlattice, $\varepsilon_l^i=0$.) A strain variation $\delta\varepsilon_{\text{ext}}^s$ externally imposed on the substrate (s) of the superlattice generates a variation of the internal strain tensor $\delta\varepsilon_{\text{ext}}^i$ in each semiconductor (i). The total strain tensor in semiconductor i is the sum of the lattice-mismatch-induced strain (ε_l^i) and the strain arising from the applied compressive stress ($\delta\varepsilon_{\text{ext}}^i$),

$$\varepsilon^i=\varepsilon_l^i+\delta\varepsilon_{\text{ext}}^i\ . \tag{3.30}$$

For a given strain variation $\delta\varepsilon_{\text{ext}}^s$ imposed on the substrate, we determine the internal strain tensor $\delta\varepsilon_{\text{ext}}^i$ in each semiconductor by minimizing the mechanical strain energy in the superlattice subject to the boundary conditions imposed by the pseudomorphic nature of the hetero-interfaces. In a typical III-V semiconductor, the change of internal electrical field is typically on the order of $\delta E_{[111]}^i\simeq 1-10$ kV/cm for a strain modulation of $\delta\varepsilon_{\text{ext}}^s=10^{-3}$.

Piezoelectric fields can be generated by an external strain both for conventional [001]-growth-axis superlattices (lattice-matched or strained-layer) and for lattice-matched [111]-growth-axis superlattices in which the piezoelectric fields vanish without the external strain. In principle, these external strain-generated fields modify the electronic structure of the superlattice. However, these modifications are quadratic in the magnitude of the field. For the range of external strains considered here, the modifications of the electronic structure caused by external strain-generated fields are very small if there is no built-in electric field. If there is a large built-in electric field already present (as is the case for [111]-growth-axis strained-layer superlattices), the modifications of the electronic structure caused by external strain-generated fields are quite significant because they correspond to modulations of a quadratic effect about a large bias point. Unlike the internal fields, which point in opposite directions in the two constituent materials forming the superlattice, the external strain-induced field is nearly uniform in the superlattice. As a result, it can be screened by external charges at the superlattice surface and at the interface between the superlattice and the substrate. We consider the case in which the strain modulation is fast compared to the surface charging time, so that such screening does not occur.

We illustrate the effects of a compressive uniaxial stress applied on the substrate of a [111]-growth-axis $\mathrm{Ga_{0.47}In_{0.53}As/Al_{0.70}In_{0.30}As}$ strained-layer superlattice. The strained-layer superlattice is grown onto an InP substrate, and external uniaxial stress is applied on the substrate along the [110] axis. The strained-layer superlattice consists of M_a layers of $\mathrm{Ga_{0.47}In_{0.53}As}$ alternating with $N_b=2M_a$ layers of $\mathrm{Al_{0.70}In_{0.30}As}$. The $\mathrm{Ga_{0.47}In_{0.53}As}$ quantum-well layers are in biaxial compression resulting from a 1.5% lattice mismatch. We consider the case of free-standing superlattices grown on a buffer layer in which both the $\mathrm{Ga_{0.47}In_{0.53}As}$ (quantum-well) and the $\mathrm{Al_{0.70}In_{0.30}As}$ (barrier) layers are strained, i.e., neither of the constituent semiconductors is pseudomorphic with the InP substrate.

The application of a compressive uniaxial stress on the InP substrate along the [110] axis increases the value of the internal compressive strain and consequently the value of the internal strain-induced piezoelectric field. A strain variation of $\delta\varepsilon_{\text{ext}}^s=1.5\times10^{-3}$ corresponds to an applied pressure of roughly 1 kbar. When no external stress is applied to the InP substrate, the internal piezoelectric field has a value of $\delta E_{[111]}^i=141$ kV/cm in the $\mathrm{Ga_{0.47}In_{0.53}As}$ layers for all three superlattice thicknesses considered below. As the external uniaxial stress is increased, the internal compressive strain in the $\mathrm{Ga_{0.47}In_{0.53}As}$ quantum-well layers is also increased, and the magnitude of the internal piezoelectric field *increases* at the rate of approximately $\delta E_{[111]}^i\approx 3$ kV/cm for a strain modulation of $\delta\varepsilon_{\text{ext}}^s=10^{-3}$.

In Fig. 38, the variation of the $\mathrm{HH_1}$-$\mathrm{C_1}$ ground-state transition energy is shown as a function of the external uniaxial stress applied on the InP substrate. Results are shown with and without the effects of the internal strain-induced piezoelectric fields. (We set $E_{[111]}^i=0$ in the calculation of the electronic structure in the latter case.) Results are shown for three superlattices layer thicknesses: $M_a/N_b=25/50$, 30/60, and 35/70. Inspection of Fig. 38 indicates that deformation-potential effects and internal electric field effects produce transition energy shifts in *opposite* directions: as the applied compressive stress is increased, deformation-potential effects *increase* the $\mathrm{HH_1}$-$\mathrm{C_1}$ transition energy, whereas internal electric field effects *reduce* the HH_1-C_1 transition energy (the magnitude of the internal piezoelectric fields increases with the applied compressive stress). When the internal strain-induced piezoelectric fields are included (solid line in Fig. 38), the transition energy shifts exhibit a strong dependence on the superlattice layer thickness at large external stress. The magnitude of the Stark shifts scales with the thickness over which the internal field acts. When only deformation-potential effects are included (dashed line in Fig. 38), the transition energy shifts are only slightly dependent on the superlattice layer thickness for the layer thicknesses considered here. Figure 38 indicates that the response of the HH_1-C_1 transition to an external uniaxial stress is dominated by internal piezoelectric field (Stark shift) effects.

The results for the HH_2-C_1 excited-state transition energy shifts are shown in Fig. 39 with and without the presence of internal piezoelectric fields. In the absence of strain-induced piezoelectric fields, the energy shifts are larger for the HH_2-C_1 transition than for the HH_1-C_1 transition. This result is due to the mixing of light- and heavy-hole states caused by the strain Hamiltonian. Conversely, when the effects of the internal piezoelectric fields are included, the energy shifts are smaller for the HH_2-C_1 transition than for the HH_1-C_1 transition. This result is due to the fact that excited states exhibit smaller Stark shifts than the ground state. For small values of applied compressive stress, the energy shifts of the HH_2-C_1 transition are dominated by deformation-potential effects at small superlattice layer thicknesses. For large values of compressive stress, internal-field effects dominate the HH_2-C_1 transition energy shifts. As in the case of the HH_1-C_1 transition, the HH_2-C_1 transition energy shifts exhibit a strong thickness dependence when internal electric fields are taken into account but a weak thickness dependence in the field-free case.

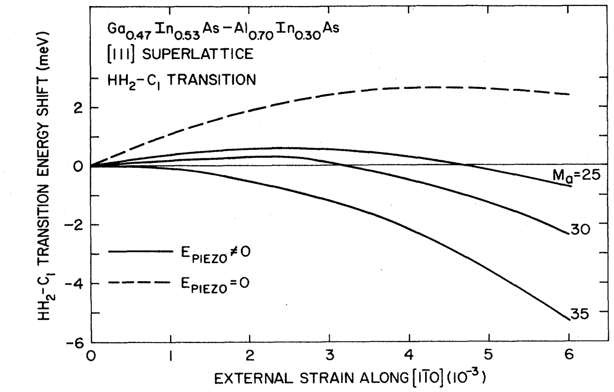

FIG. 39. Variation of the HH_2-C_1 transition as a function of the strain caused by the application of a compressive stress on the substrate of a $Ga_{0.47}In_{0.53}As/Al_{0.70}In_{0.30}As$ strained-layer superlattice grown along the [111] axis. The compressive stress is applied to the InP substrate along the [110] axis. When no external stress is applied to the InP substrate, the (unscreened) internal piezoelectric field has a value of $E^{i}_{[111]}=141$ kV/cm in the $Ga_{0.47}In_{0.53}As$ layers. The $Ga_{0.47}In_{0.53}As/Al_{0.70}In_{0.30}As$ superlattice consists of M_a layers of $Ga_{0.47}In_{0.53}As$ (wells) alternating with $N_b=2M_a$ layers of $Al_{0.70}In_{0.30}As$ (barriers). The $Ga_{0.47}In_{0.53}As$ layers are under biaxial compression resulting from a 1.5% lattice mismatch at the hetero-interfaces. Results are shown with (solid lines) and without (dashed lines) the presence of internal strain-induced piezoelectric fields. Without the internal field, the calculated shift is essentially the same for the three superlattices.

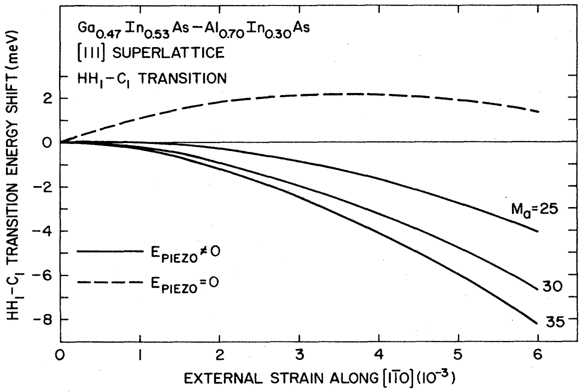

FIG. 38. Variation of the HH_1-C_1 transition as a function of the strain caused by the application of a compressive stress on the substrate of a $Ga_{0.47}In_{0.53}As/Al_{0.70}In_{0.30}As$ strained-layer superlattice grown along the [111] axis. The compressive stress is applied on the InP substrate along the [110] axis. When no external stress is applied to the InP substrate, the (unscreened) internal piezoelectric field has a value of $E^{i}_{[111]}=141$ kV/cm in the $Ga_{0.47}In_{0.53}As$ layers. The $Ga_{0.47}In_{0.53}As/Al_{0.70}In_{0.30}As$ superlattice consists of M_a layers of $Ga_{0.47}In_{0.53}As$ (wells) alternating with $N_b=2M_a$ layers of $Al_{0.70}In_{0.30}As$ (barriers). The $Ga_{0.47}In_{0.53}As$ layers are under biaxial compression resulting from a 1.5% lattice mismatch at the hetero-interfaces. Results are shown with (solid lines) and without (dashed lines) the presence of internal strain-induced piezoelectric fields. Without the internal field, the calculated shift is essentially the same for the three superlattices.

We now consider the modulation of optical properties of strained-layer superlattices by the application of a compressive uniaxial stress to the superlattice substrate. Results of optical-absorption calculations are shown in Fig. 40 for incoming radiation propagating along the [111] growth axis. The superlattice consists of $M_a=25$ layers of $Ga_{0.47}In_{0.53}As$ (wells in biaxial compression) alternating with $N_b=50$ layers of $Al_{0.70}In_{0.30}As$ (barriers in biaxial tension) grown onto an InP substrate. We present numerical results without [Fig. 40(a)] and with [Fig. 40(b)] the effects of internal strain-induced piezoelectric fields. In both cases, the optical-absorption spectrum is calculated for zero external stress and for an external stress producing a strain variation of $\delta\epsilon^{s}_{\rm ext}=5\times10^{-3}$. Only the optical transitions HH_1-C_1, HH_2-C_1, and HH_3-C_1 are shown.

When internal piezoelectric fields are neglected [Fig. 40(a)], the HH_1-C_1 optical transition is strongly allowed, whereas the HH_2-C_1 and HH_3-C_1 transitions are very weakly allowed. The application of an external compressive stress increases the optical transition energies when the internal-field effects are neglected. The presence of internal piezoelectric fields [Fig. 40(b)] modifies the optical matrix elements and decreases the oscillator strength associated with the HH_1-C_1 transition while increasing the oscillator strength associated with the HH_2-C_1 and HH_3-C_1 transitions. In fact, in the presence of internal fields, the HH_2-C_1 transition is the dominant feature in the optical-absorption spectrum. The application of an external compressive uniaxial stress produces different responses, depending on the optical transition: the HH_1-C_1 transition energy is decreased, the HH_2-C_1 transition energy remains nearly unshifted, and the HH_3-C_1 transition energy is increased by the application of external stress.

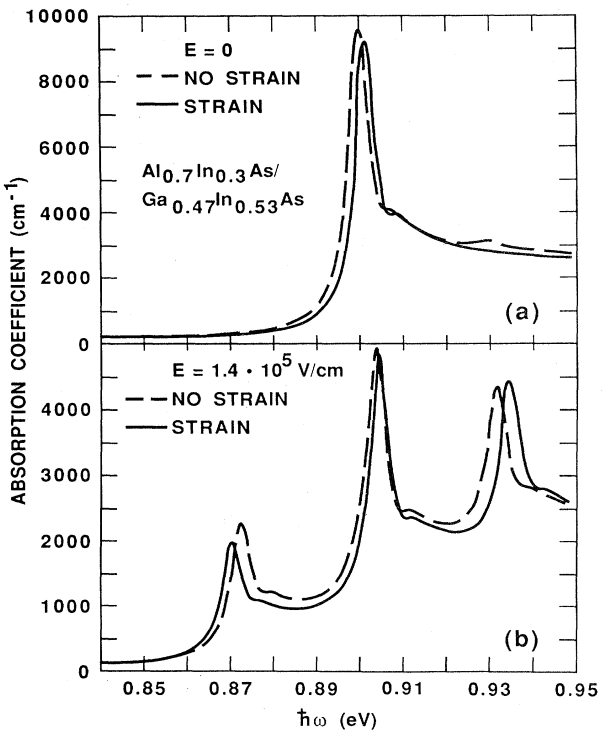

FIG. 40. Optical absorption spectrum of a $Ga_{0.47}In_{0.53}As/Al_{0.70}In_{0.30}As$ [111]-growth-axis strained-layer superlattice consisting of $M_a=25$ layers of $Ga_{0.47}In_{0.53}As$ (wells in biaxial compression) alternating with $N_b=50$ layers of $Al_{0.70}In_{0.30}As$ (barriers in biaxial tension) grown onto an InP substrate: (a) optical absorption without internal piezoelectric field effects; (b) optical absorption with the presence of internal strain-induced piezoelectric fields oriented along the [111] growth axis. The incoming light is propagating along the [111] growth axis. Optical absorption results are shown with no external stress (dashed line) and with a compressive stress causing a strain modulation of $\delta\varepsilon^{s}_{\text{ext}}=5\times10^{-3}$ (solid line). The compressive stress is applied on the InP substrate along the [110] axis.

IV. COMPARISON OF RESULTS OBTAINED BY DIFFERENT THEORETICAL TECHNIQUES

In this section we compare three theoretical schemes currently used for the calculation of the electronic structure of semiconductor superlattices. We specifically consider the tight-binding model as formulated by Schulman and Chang (1983), the two-band envelope-function model as formulated by Bastard (1981), and the **k**·**p** model as formulated by Smith and Mailhiot (1986). The tight-binding model can describe states throughout the Brillouin zone. The **k**·**p** model can describe states near the zone center. The two-band envelope-function model can describe states near the zone center whose wave vector is along the superlattice growth axis. We present the results of band-structure calculations (1) for a [001]-oriented $GaAs/Ga_{0.7}Al_{0.3}As$ superlattice consisting of 30 layers of GaAs alternating with 10 layers of $Ga_{0.7}Al_{0.3}As$ and (2) for a [001]-oriented InAs/GaSb superlattice consisting of 17 layers of InAs alternating with 17 layers of GaSb. The tight-binding calculations are taken from Schulman and Chang (1985a). These models are based on different descriptions of the bulk constituent materials. All three models require the input of empirical parameters. The two-band envelope-function model can be interpreted as a simplified version of the **k**·**p** model. Therefore there is a correspondence between the input parameters required for these two methods. However, there is no direct correspondence between the input parameters for the tight-binding model and those for the **k**·**p** and two-band envelope-function models. The results of these three methods depend on the values of the input parameters. Therefore any comparison of the results of the models is influenced by one's choice of input parameters. There is no unique method for relating the input parameters.

The two-band envelope-function method can be derived from the **k**·**p** method by making a series of approximations (Smith and Mailhiot, 1986). Starting with the **k**·**p** method, this can be done by considering only the $\mathbf{k}_{\parallel}=0$ case, carrying out perturbation theory only to zeroth order in wave functions and first order in energies, and taking the spin-orbit interaction to be very large so as to drop the split-off band states. Taking the spin-orbit interaction to be very large reduces the Hamiltonian matrix to 6×6. Neglecting higher-order terms in Löwdin perturbation theory and taking $\mathbf{k}_{\parallel}=0$ decouples the heavy-hole states from the light-hole and conduction-band states. The 4×4 Hamiltonian describing the light-hole and conduction-band states is block diagonal in two identical 2×2 blocks. Solution of these two 2×2 matrices gives the two-band envelope-function method. Strictly speaking, the heavy-hole bands are dispersionless if coupling to higher-lying zone-center basis states is neglected. Here, we allow such a coupling and describe the heavy-hole bands by a scaled Kronig-Penney model in which the heavy-hole effective mass is an input parameter.

The tight-binding calculations (Schulman and Chang, 1985a) were performed using five orthonormal spatial orbitals centered at each atomic site and first-nearest-neighbor coupling, with the spin-orbit interaction included. Strain was neglected for these nearly lattice-matched superlattices. Input parameters to the tight-binding model consisted of bulk Hamiltonian matrix elements (13 in each material), spin-orbit-interaction matrix elements for the p-type orbitals (2 in each material), a valence-band offset, and a prescription for choosing the Hamiltonian matrix elements for the interface atoms. (For the GaAs/GaAlAs superlattice, three on-site parameters for the As at the interface must be specified. For the InAs/GaSb superlattice, which has both a GaAs- and an InSb-like interface, there are 32 interface parameters that must be specified. This number is reduced to 16 if the interfacial atoms are chosen to have bulk on-site matrix elements.) Calculated bulk values of band gaps, effective masses in the [001] direction, and spin-orbit splitting energies were reported. Superlattice energy subband dispersion near the zone center, both parallel to the growth axis and in the interface plane, was computed.

In the $\mathbf{k}\cdot\mathbf{p}$ model, a reference Hamiltonian is defined by averaging the bulk pseudopotentials of the constituent materials. This reference Hamiltonian is diagonalized at the zone center, and first- and second-order momentum matrix elements are calculated. The bulk constituent materials are described near the zone center by treating the $\mathbf{k}\cdot\mathbf{p}$ and ΔV operators, where ΔV is the difference between the material pseudopotential and the reference pseudopotential, to first order for wave functions and second order for energies in Löwdin perturbation theory. The lowest Γ_1 conduction-band state and highest Γ_{15} valence-band states, coupled with spinors, are treated explicitly. The spin-orbit interaction is included between the explicitly treated states. In order to compare this model with the tight-binding calculations, strain is neglected. Input parameters to the $\mathbf{k}\cdot\mathbf{p}$ model consist of bulk pseudopotential form factors (6 in each material), spin-orbit splitting parameters (1 for each material), and a valence-band offset.

For $\mathbf{k}$ along the [001] direction, effective masses for heavy-hole, light-hole, and conduction-band states are given by

$$\frac{m}{m_h}=1+\frac{2m}{\hbar^2}M\ , \tag{4.1}$$

$$\frac{m}{m_l}=\left[1+\frac{2m}{\hbar^2}\left(\tfrac{2}{3}L'+\tfrac{1}{3}M\right)\right]-\frac{2m}{\hbar^2}|P|^2\frac{2}{3E_g}\ , \tag{4.2}$$

$$\frac{m}{m_c}=\left[1+\frac{2m}{\hbar^2}A'\right]+\frac{2m}{\hbar^2}|P|^2\left[\frac{2}{3E_g}+\frac{1}{3(E_g+\Delta)}\right]\ , \tag{4.3}$$

where m_h, m_l, and m_c are the heavy-hole, light-hole, and conduction-band effective masses, respectively. Here m is the free-electron mass, E_g is the band-gap energy, Δ is the valence-band spin-orbit splitting, $|P|$ is the first-order momentum matrix element between the Γ_1 and Γ_{15} states, and M, L', and A' are second-order momentum matrix elements (Kane, 1966). In the $\mathbf{k}\cdot\mathbf{p}$ model, the $\mathbf{k}\cdot\mathbf{p}$ and ΔV interactions are treated to second order for energies. The first-order momentum matrix element $|P|$ is modified by the potential ΔV [i.e., cross terms proportional to $(\mathbf{k}\cdot\mathbf{p})\Delta V$ occur in the second-order energy expressions]. Therefore $|P|$ has different values in the two constituent materials. However, the second-order momentum matrix elements are not modified by the potential ΔV. As a result, they must take on the same value in the two constituent materials. Thus, for example, the heavy-hole effective mass must be the same in the two constituent materials. It would be necessary to calculate to at least third order [so that terms of the form $(\mathbf{k}\cdot\mathbf{p})^2\Delta V$ occurred in the energy expressions] for the second-order momentum matrix elements to be different in the constituent materials.

The two-band envelope-function model can be interpreted as an approximation to the $\mathbf{k}\cdot\mathbf{p}$ model in which only $\mathbf{k}_\parallel=0$ is considered, perturbation theory is carried out to first order for energies, and the spin-orbit interaction is taken to be very large. Strictly speaking, the heavy-hole band is dispersionless in this model. Here we include it by a scaled Kronig-Penney model with the heavy-hole effective mass as an input parameter. The input parameters to the calculation are the band gaps of the two constituent materials, the first-order momentum matrix element, the heavy-hole effective mass, and the valence-band offset. The first-order momentum matrix element is the same in the two constituent materials because the perturbation theory is only through first order for energies. If different values for this matrix element are taken in the two constituent materials, current is not conserved at the interface. For $\mathbf{k}$ along the [001] direction, the light-hole and electron effective masses are given by

$$m_l=-m_c\ , \tag{4.4}$$

$$\frac{m}{m_c}=\frac{2m}{\hbar^2}|P|^2\frac{2}{3E_g}\ . \tag{4.5}$$

A pseudopotential calculation gives band gaps and first- and second-order momentum matrix elements, which are input to the $\mathbf{k}\cdot\mathbf{p}$ model. The band gaps and effective masses that result are in fair but not precise agreement with those obtained in the tight-binding model. In order to compare results of the two models, we use the same band gaps in the $\mathbf{k}\cdot\mathbf{p}$ model as were calculated in the tight-binding model; adjust the second-order momentum matrix element M so that the heavy-hole effective mass in the $\mathbf{k}\cdot\mathbf{p}$ model is the average of the heavy-hole effective masses for the two constituent materials in the tight-binding model; adjust the two first-order momentum matrix elements so that the electron effective masses in the two constituent materials are the same as those in the tight-binding model; and use the same valence-band offset and spin-orbit splitting as in the

TABLE I. Effective masses in the tight-binding, **k·p**, and envelope-function models.

	Tight-binding model	**k·p** model	Envelope-function model
		GaAs	
m_c	0.067	0.067	0.11
$\|m_l\|$	0.070	0.091	0.11
$\|m_h\|$	0.45	0.48	0.48
		$Ga_{0.7}Al_{0.3}As$	
m_c	0.10	0.10	0.15
$\|m_l\|$	0.093	0.14	0.15
$\|m_h\|$	0.52	0.48	0.48
		InAs	
m_c	0.023	0.023	0.031
$\|m_l\|$	0.027	0.028	0.031
$\|m_h\|$	0.41	0.37	0.37
		GaSb	
m_c	0.049	0.049	0.061
$\|m_l\|$	0.051	0.060	0.061
$\|m_h\|$	0.33	0.37	0.37

tight-binding model. The other second-order momentum matrix elements were as calculated in the pseudopotential method. Other schemes for picking the parameters could be used. For example, the second-order momentum matrix elements A' and L' could have been adjusted to try to match the light-hole effective masses in the tight-binding model. (We did not do this because the light-hole effective mass is rather insensitive to these second-order matrix elements and larger adjustments were required than we felt were physically reasonable to match the tight-binding model values.) The same band gaps, valence-band offsets, and heavy-hole effective masses were used in the envelope-function model as in the **k·p** model. The first-order momentum matrix was taken to be the average value for the constituent materials of the **k·p** model. This is the value the matrix element takes if the envelope-function model is viewed as a simplified version of the **k·p** model in which the difference potential ΔV is treated to lower order in perturbation theory. Table I lists the effective masses for the four materials in the three models.

Results of energy-band dispersion along the [001] growth axis of the $GaAs/Ga_{0.7}Al_{0.3}As$ superlattice calculated in the tight-binding, **k·p**, and envelope-function models are shown in Fig. 41. The valence-band offset is 71 meV. The zero of energy corresponds to the GaAs valence-band maximum. For superlattice wave vectors along the [001] growth axis, the factor group is C_{2V}. There is only a single two-dimensional representation compatible with spin. Consequently, all bands are twofold degenerate, and band crossing is forbidden. From the figure, one sees that there is generally good correspondence between the results of the three models. The envelope-function model does not include interaction between heavy- and light-hole bands and therefore does not correctly describe the anticrossing behavior. The tight-binding and **k·p** models do include this interaction and correctly describe the anticrossing behavior. However, the interaction is not very strong in these models, and the energy range of significant band mixing is not very large.

Results of energy-band dispersion when the superlattice wave vector lies in the [100] direction, which is in the plane of the interfaces, calculated in the tight-binding and **k·p** models, are shown in Fig. 42. The envelope-function model does not describe dispersion in the plane of the interfaces. For superlattice wave vectors in this direction, the factor group is C_2. This group contains two one-dimensional representations compatible with spin. Superlattice subbands belonging to different representations can cross, but those belonging to the same representation cannot cross. There is generally good correspondence between the results of the two models. The tight-binding model results have slightly larger dispersion. This is probably related to the fact that the bulk light-hole effective masses are somewhat smaller in the tight-binding model.

Results of energy-band dispersion along the [001] growth axis of the InAs/GaSb superlattice, calculated in the tight-binding, **k·p**, and envelope-function models, are shown in Fig. 43. Results of energy-band dispersion along the [100] axis, calculated in the tight-binding and **k·p** models, are shown in Fig. 44. The energy difference between the conduction-band minimum of InAs and the valence-band maximum of GaSb is 0.10 eV. The zero of energy corresponds to the InAs valence-band maximum. The superlattice valence-band maximum lies at slightly less than 0.5 eV, and the conduction-band minimum lies slightly over 0.6 eV in the three calculations. There is generally good correspondence between the calculations. As for GaAs/GaAlAs, the envelope-function model does not include interactions between heavy- and light-hole bands. However, these interactions are rather small in both the tight-binding and the **k**·**p** models. In Fig. 44, the size of the spin splittings is larger in the tight-binding model than in the **k**·**p** model. The size of these splitting is parameter dependent, and the fact that it is larger in the tight-binding model probably has more to do with the input parameters than with anything fundamental about the models.

Comparisons of energy-band dispersion calculations for a GaAs/GaAlAs and an InAs/GaSb superlattice indicate generally good correspondence between the tight-binding, **k**·**p**, and envelope-function models. Discrepancies between the three models are on the order of 10 meV or less. The discrepancies tend to be larger for states away from the superlattice band gap. For the **k**·**p** and envelope-function models, there is a direct correspondence between the input parameters of the models. There is no direct correspondence, however, between the input parameters of the tight-binding model and those of the other two. Discrepancies between the results of the models probably come from the slightly different descriptions of the bulk constituents as much as from a different treatment of the superlattice.

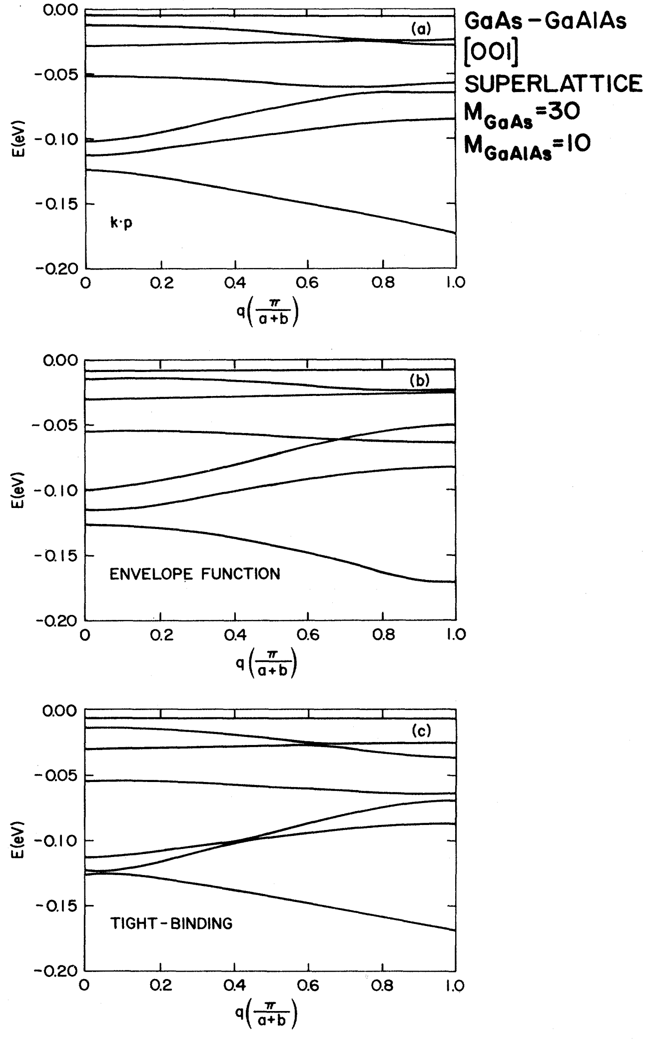

FIG. 41. Energy subband dispersion along the [001] growth axis of a GaAs/$Ga_{0.70}Al_{0.30}As$ superlattice consisting of $M_a=30$ layers of GaAs alternating with $N_b=10$ layers of $Ga_{0.70}Al_{0.30}As$, from results obtained using the following models: (a) **k**·**p**; (b) envelope-function; (c) tight-binding. The tight-binding results are from Schulman and Chang (1985a). The zero of energy is the valence-band maximum of GaAs.

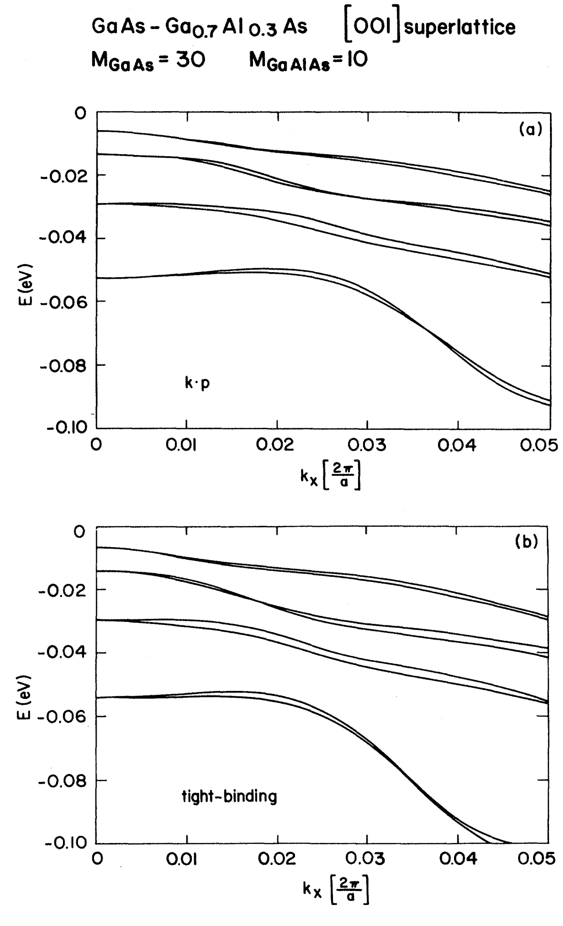

FIG. 42. Energy subband dispersion along the [100] direction of a [001]-oriented GaAs/$Ga_{0.70}Al_{0.30}As$ superlattice consisting of $M_a=30$ layers of GaAs alternating with $N_b=10$ layers of $Ga_{0.70}Al_{0.30}As$, from results obtained using the following models: (a) **k**·**p**; (b) tight binding. The tight-binding results are from Schulman and Chang (1985a).

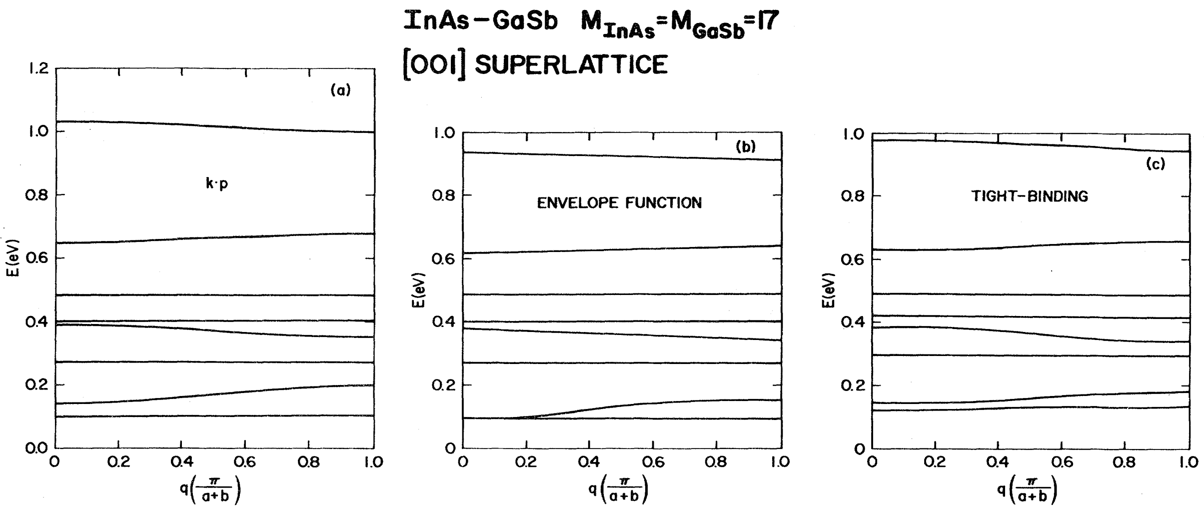

FIG. 43. Energy subband dispersion along the [001] growth axis of an InAs/GaSb superlattice consisting of $M_a=17$ layers of InAs alternating with $N_b=17$ layers of GaSb, from results obtained using the following models: (a) **k**·**p**; (b) envelope function; (c) tight binding. The tight-binding results are from Schulman and Chang (1985a). The zero of energy is the valence-band maximum of InAs.

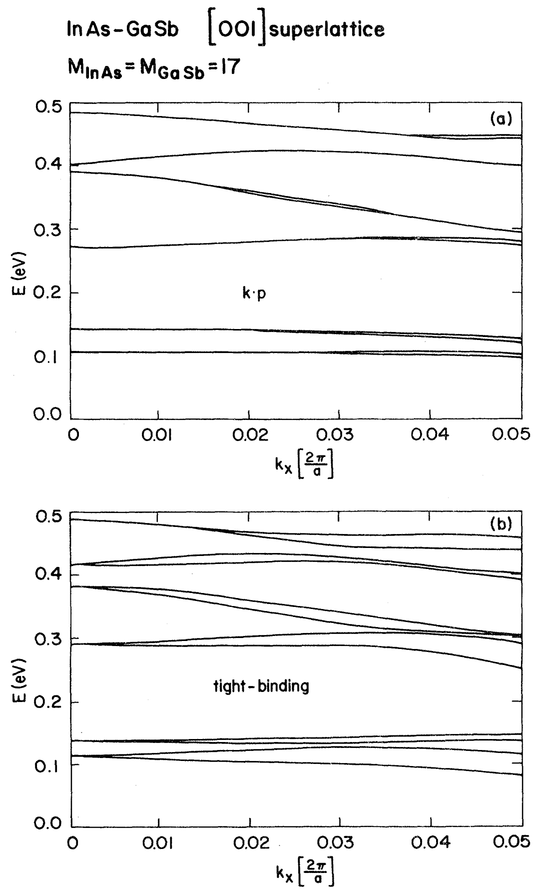

FIG. 44. Energy subband dispersion along the [100] direction of a [001]-oriented InAs/GaSb superlattice consisting of $M_a=17$ layers of InAs alternating with $N_b=17$ layers of GaSb, from results obtained using the following models: (a) **k**·**p**; (b) tight binding. The tight-binding results are from Schulman and Chang (1985a).

V. SUMMARY

In this review we have discussed various theoretical schemes currently used for the calculation of the electronic structure and optical properties of semiconductor superlattices. These schemes differ substantially in their level of numerical complexity and in their ability to provide a realistic description of the superlattice.

The bulk electronic states that are most perturbed by the superlattice potential are those whose mean free path is longer than or comparable to the superlattice period. Consequently, electronic states whose energies are close to the conduction- or valence-band edges of the constituent semiconductors are of greatest interest in the description of superlattice materials. The novel electronic and optical features that occur in semiconductor superlattices usually manifest themselves within an energy range of a few tenths of an eV from the energy-band edges of the constituent semiconductors. As a result, the most useful theoretical approaches for the calculation of electronic structure and optical properties of superlattices are based on techniques that provide a detailed description of the bulk electronic states near the energy-band edges of the constituent semiconductors.

Theoretical methods that serve as the basis for a description of the electronic structure of semiconductor superlattices can roughly be divided into two general classes. In one approach, the superlattice is essentially viewed as a new material, whose unit cell is enlarged to the dimensions of the superlattice period. A Hamiltonian is constructed to describe the electronic interactions within this enlarged unit cell. We refer to this description as the supercell method. In another approach, the electronic structure and optical properties of the superlattice are explicitly related to those of the constituent bulk semiconductors. At a given energy, the superlattice wave function is expanded in terms of the propagating (real values of **k**) and evanescent (complex values of **k**) bulk states of the constituent semiconductors with the same energy. The superlattice energy eigenvalue spectrum and wave functions are obtained by imposing a set of boundary conditions on the superlattice state across the interfaces. We refer to this description as the boundary-condition method.

The supercell technique is essentially identical to traditional electronic band-structure formalisms in which the crystal wave vector is input and the energy eigenvalues associated with this wave vector are obtained by diagonalization of the Hamiltonian matrix. Both empirical and first-principles approaches have been used. The supercell method provides a description of the superlattice electronic structure over a large energy range. The size of the Hamiltonian matrix increases with the superlattice period. Consequently, the application of supercell methods to thick-layer superlattices leads to numerical complexities that make the method impractical for these cases. Only thin-layer superlattices can realistically be treated with this formal approach. For this reason, supercell methods are seldom used in the interpretation of experimental data on commonly grown superlattices. Supercell techniques have proven to be useful in first-principles descriptions of the valence-electron charge redistribution at semiconductor hetero-interfaces. These *ab initio* methods have been particularly useful in the study of semiconductor heterojunction energy-band offsets.

In the boundary-condition framework, superlattice states are interpreted in terms of the bulk eigenstates associated with the constituent semiconductors. The calculation of the bulk states in the constituent semiconductors is usually performed within the context of an empirical procedure. However, first-principles methods have been applied to a single hetero-interface. Input parameters include superlattice energy-band offsets, in addition to any set of parameters necessary to describe the bulk Bloch states of the constituent semiconductors in a given basis. The superlattice wave function is then expanded as a liner combination of the bulk states of the two constituent semiconductors. The expansion coefficients of a particular superlattice state are determined by simultaneously imposing a set of boundary conditions on the superlattice wave function across the superlattice interfaces and requiring that the superlattice wave function satisfy Bloch's theorem. Since the superlattice wave function is expanded in terms of bulk Bloch states, a clear physical interpretation emerges from the identification of the bulk states that enter the expansion of the superlattice wave function. This method is different from traditional electronic band-structure algorithms, since the energy is input and all the corresponding superlattice solutions are obtained from the interfacial and periodic boundary conditions. At an arbitrary energy, the superlattice solutions will, in general, have complex wave vectors that are associated with evanescent states. Consequently this method requires that an energy search be performed to identify the superlattice solutions associated with real superlattice wave vectors. Unlike supercell methods, boundary-condition methods do not increase in numerical complexity with superlattice layer thickness, so that they can, in principle, be applied to superlattices with arbitrary layer thickness. This method is currently the most widely used in the interpretation of experimental data.

The numerical results presented in this article were mostly obtained by the boundary-condition approach using a **k**·**p** method for the calculation of the electronic structure of the bulk constituent semiconductors and of the superlattice. For comparison purposes, superlattice electronic-structure calculations using an empirical tight-binding method and the two-band envelope-function method were also presented. The results of these three models are in generally good agreement. The modest discrepancies between the results of the models probably come from a slightly different description of the bulk constituents as much as from a different treatment of the superlattice.

On the whole, currently available theoretical methods appear to describe the electronic structure of semiconductor superlattices at least qualitatively. Detailed quantitative comparison between theory and experiment is complicated by the need for precise structural characterization of the samples and by the need for accurate knowledge of empirical parameters. Knowledge of valence-band offsets is often a particular problem. Perhaps the most important role of theory in superlattice research is in the design of new materials that have interesting and useful properties. The detailed values of parameters are often not critical in this process.

ACKNOWLEDGMENTS

We thank J. N. Schulman and Y. C. Chang for permission to use their results. The work of D. L. Smith was supported by Los Alamos National Laboratory Institutional Supporting Research.

REFERENCES

Altarelli, M., 1983, Phys. Rev. B **28**, 842.

Altarelli, M., 1985, J. Lumin. **30**, 472.

Altarelli, M., U. Ekenberg, and A. Fasolino, 1985, Phys. Rev. B **32**, 5138.

Ando, T., A. B. Fowler, and F. Stern, 1982, Rev. Mod. Phys. **54**, 437.

Andreoni, W., A. Baldereschi, and R. Car, 1978, Solid State Commun. **27**, 821.

Baraff, G. A., J. A. Appelbaum, and D. R. Hamann, 1977, Phys. Rev. Lett. **38**, 237.

Bastard, G., 1981, Phys. Rev. B **24**, 5693.

Bastard, G., 1982, Phys. Rev. B **25**, 7584.

Bastard, G., 1985, in *Proceedings of the NATO Advanced Study*

Institute on Molecular Beam Epitaxy and Heterostructures, edited by L. L. Chang and K. Ploog (Nijhoff, The Hague), p. 381.

Bastard, G., and J. A. Brum, 1986, IEEE J. Quantum Electron. **QE-22**, 1625.

Batra, I. P., S. Ciraci, and J. S. Nelson, 1987, J. Vac. Sci. Technol. B **5**, 1300.

Bean, J. C., 1985, in *Proceedings of the First International Symposium on Silicon Molecular Beam Epitaxy,* edited by J. C. Bean (Electrochemical Society, New Jersey), p. 339.

Beery, J. G., B. K. Laurich, C. J. Maggiore, D. L. Smith, K. Elcess, C. G. Fonstad, and C. Mailhiot, 1989, Appl. Phys. Lett. **54**, 233.

Ben-Daniel, D. J., and C. B. Duke, 1966, Phys. Rev. **152**, 683.

Bir, G. L., and G. E. Pikus, 1974, *Symmetry and Strain-Induced Effects in Semiconductors* (Wiley, New York).

Blakeslee, A. E., and C. F. Aliotta, 1970, IBM J. Res. Dev. **14**, 686.

Bloss, W. L., and L. Friedman, 1982, Appl. Phys. **41**, 1023.

Bloss, W. L., and L. Friedman, 1983, J. Vac. Sci. Technol. B **1**, 150.

Brum, J. A., and G. Gastard, 1985, Phys. Rev. B **31**, 3893.

Brum, J. A., P. Voisin, M. Voos, L. L. Chang, and L. Esaki, 1988, Surf. Sci. **196**, 545.

Burt, M. G., 1988, Semicond. Sci. Technol. **3**, 739.

Bylander, D. M., and L. Kleinman, 1986, Phys. Rev. B **34**, 5280.

Bylander, D. M., and L. Kleinman, 1987a, Phys. Rev. Lett. **59**, 2091.

Bylander, D. M., and L. Kleinman, 1987b, Phys. Rev. B **36**, 3229.

Cady, W. F., 1946, *Piezoelectricity* (McGraw-Hill, New York), p. 192.

Capasso, F., K. Mohammed, A. Y. Cho, R. Hull, and A. L. Hutchinson, 1985a, Appl. Phys. Lett. **47**, 420.

Capasso, F., K. Mohammed, A. Y. Cho, R. Hull, and A. L. Hutchinson, 1985b, Phys. Rev. Lett. **55**, 1152.

Cardona, M., and F. H. Pollak, 1966, Phys. Rev. **142**, 530.

Caruthers, E., and P. J. Lin-Chung, 1977, Phys. Rev. Lett. **38**, 1543.

Caruthers, E., and P. J. Lin-Chung, 1978a, Phys. Rev. B **17**, 2705.

Caruthers, E., and P. J. Lin-Chung, 1978b, J. Vac. Sci. Technol. **15**, 1459.

Chadi, D. J., 1977a, Phys. Rev. B **16**, 790.

Chadi, D. J., 1977b, Phys. Rev. B **16**, 3572.

Chang, L. L., and B. C. Giessen, 1985, eds., *Synthetic Modulated Structures* (Academic, New York).

Chang, L. L., and K. Ploog, 1985, eds., *Proceedings of the NATO Advanced Study Institute on Molecular Beam Epitaxy and Heterostructures* (Nijhoff, The Hague).

Chang, L. L., G. A. Sai-Halasz, L. Esaki, and R. L. Aggarwal, 1981, J. Vac. Sci. Technol. **19**, 589.

Chang, Y. C., 1982, Phys. Rev. B **25**, 605.

Chang, Y. C., 1985a, J. Appl. Phys. **58**, 499.

Chang, Y. C., 1985b, Appl. Phys. Lett. **46**, 710.

Chang, Y. C., 1988, Phys. Rev. B **37**, 8215.

Chang, Y. C., and J. N. Schulman, 1982a, Phys. Rev. B **25**, 3975.

Chang, Y.-C., and J. N. Schulman, 1982b, J. Vac. Sci. Technol. **21**, 540.

Chang, Y. C., and J. N. Schulman, 1983, Appl. Phys. Lett. **43**, 536.

Chang, Y. C., and J. N. Schulman, 1985, Phys. Rev. B **31**, 2069.

Chang, Y. C., J. N. Schulman, and U. Efron, 1987, J. Appl. Phys. **62**, 453.

Chemla, D. S., D. A. B. Miller, P. W. Smith, A. C. Gossard, and W. Wiegmann, 1984, IEEE J. Quantum Electron. **QE-20**, 265.

Cho, A. Y., 1971, Appl. Phys. Lett. **19**, 467.

Christensen, N. E., 1988, Phys. Rev. B **37**, 4528.

Christensen, N. E., E. Molinari, and G. B. Bachelet, 1985, Solid State Commun. **56**, 125.

Ciraci, S., and I. P. Batra, 1987, Phys. Rev. Lett. **58**, 2114.

Ciraci, S., and I. P. Batra, 1988, Phys. Rev. B **38**, 1835.

Cohen, M. L., 1980, Adv. Electron. Electron. Phys. **51**, 1.

Cooperman, G., L. Friedman, and W. L. Bloss, 1984, Appl. Phys. Lett. **44**, 977.

Dingle, R., 1987, ed., *Applications of Multiquantum Wells, Selective Doping, and Superlattices* (Academic, New York).

Dingle, R., A. C. Gossard, and W. Wiegmann, 1975, Phys. Rev. Lett. **34**, 1327.

Dingle, R., W. Wiegmann, and C. H. Henry, 1974, Phys. Rev. Lett. **33**, 827.

Döhler, G. H., 1981, Phys. Scr. **24**, 430.

Dresselhaus, G., A. F. Kip, and C. Kittel, 1955, Phys. Rev. **98**, 368.

Ekenberg, U., and M. Altarelli, 1984, Phys. Rev. B **30**, 3369.

Elcess, K., J.-L. Liévin, and C. G. Fonstad, 1988, J. Vac. Sci. Technol. B **6**, 638.

Eppenga, R., and M. F. H. Schuurmans, 1988, Phys. Rev. B **38**, 3541.

Eppenga, R., M. F. H. Schuurmans, and S. Colak, 1987, Phys. Rev. B **36**, 1554.

Esaki, L., 1985a, in *Synthetic Modulated Structures,* edited by L. L. Chang and B. C. Giessen (Academic, New York), p. 3.

Esaki, L., 1985b, in *Proceedings of the 17th International Conference on the Physics of Semiconductors,* edited by J. D. Chadi and W. A. Harrison (Springer, New York), p. 473.

Esaki, L., L. L. Chang, W. E. Howard, and V. L. Rideout, 1972, in *Proceedings of the 11th International Conference on the Physics of Semiconductors,* edited by M. Miasek (Polish Scientific, Warsaw), p. 431.

Esaki, L., L. L. Chang, and R. Tsu, 1970, in *Proceedings of the 12th International Conference on Low Temperature Physics* (Keigaku, Tokyo), p. 551.

Esaki, L., and R. Tsu, 1970, IBM J. Res. Dev. **14**, 61.

Fasolino, A., and M. Altarelli, 1984a, in *Two-Dimensional Systems, Heterostructures and Superlattices,* edited by G. Bauer, F. Kucher, and H. Heinrich (Springer, Berlin/New York), p. 176.

Fasolino, A., and M. Altarelli, 1984b, Surf. Sci. **142**, 322.

Faurie, J. P., S. Sivananthan, and J. Reno, 1986, J. Vac. Sci. Technol. A **4**, 2096.

Frank, F. C., 1963, J. Appl. Phys. **34**, 117.

Frank, F. C., and J. H. van der Merwe, 1949, Proc. R. Soc. London, Ser. A **198**, 216.

Fritz, I. J., L. R. Dawson, and T. E. Zipperian, 1983, Appl. Phys. Lett. **43**, 846.

Froyen, S., D. W. Wood, and A. Zunger, 1988, Phys. Rev. B **37**, 6893.

Gell, M. A., D. Ninno, M. Jaros, and D. C. Herbert, 1986, Phys. Rev. B **34**, 2416.

Gell, M. A., K. B. Wong, D. Ninno, and M. Jaros, 1986, J. Phys. C **19**, 3821.

Godby, R. W., M. Schlüter, and L. J. Sham, 1986, Phys. Rev. Lett. **56**, 2415.

Godby, R. W., M. Schlüter, and L. J. Sham, 1987, Phys. Rev. B **35**, 4170.

Goossen, K. W., S. A. Lyon, and K. Alavi, 1988, Appl. Phys.

Lett. **52**, 1701.

Harrison, W. A., 1980, *Electronic Structure and the Properties of Solids* (Freeman, San Francisco).

Hayakawa, T., T. Suyama, K. Takahashi, M. Kondo, S. Yamamoto, and T. Hijikata, 1988, Appl. Phys. Lett. **52**, 339.

Hayakawa, T., K. Takahashi, M. Kondo, T. Suyama, S. Yamamoto, and T. Hijikata, 1988a, Phys. Rev. Lett. **60**, 349.

Hayakawa, T., K. Takahashi, M. Kondo, T. Suyama, S. Yamamoto, and T. Hijikata, 1988b, Phys. Rev. B **38**, 1526.

Heine, V., 1963, Proc. Phys. Soc. London **81**, 300.

Holonyak, N., Jr., R. M. Kolbas, R. D. Dupuis, and P. D. Dapkus, 1980, IEEE J. Quantum Electron. **QE-16**, 170.

Hybertsen, M. S., and S. G. Louie, 1985, Phys. Rev. Lett. **55**, 1418.

Hybertsen, M. S., and S. G. Louie, 1986, Phys. Rev. B **34**, 5390.

Hybertsen, M. S., and M. Schlüter, 1987, Phys. Rev. B **36**, 9683.

Ihm, J., and M. L. Cohen, 1979, Phys. Rev. B **20**, 729.

Ihm, J., P. K. Lam, and M. L. Cohen, 1979, Phys. Rev. B **20**, 4120.

Jagannath, C., E. S. Koteles, J. Lee, Y. J. Chen, B. S. Elman, and J. Y. Chi, 1986, Phys. Rev. B **34**, 7027.

Jaros, M., K. B. Wong, and M. A. Gell, 1985, Phys. Rev. B **31**, 1205.

Jaros, M., K. B. Wong, M. A. Gell, and D. J. Wolford, 1985, J. Vac. Sci. Technol. B **3**, 1051.

Jha, S. S., and N. Bloemberger, 1968, Phys. Rev. **171**, 891.

Johnson, N. F., H. Ehrenreich, K. C. Hass, and T. C. McGill, 1987, Phys. Rev. Lett. **59**, 2352.

Jones, R. O., 1966, Proc. Phys. Soc. London **89**, 443.

Kaminow, I. P. and E. H. Turner, 1971, "Linear Electro-optical Materials," in *Handbook of Lasers,* edited by R. J. Pressley (Chemical Rubber, Cleveland), p. 452.

Kane, E. O., 1956, J. Phys. Chem. Solids **1**, 82.

Kane, E. O., 1957, J. Phys. Chem. Solids **1**, 249.

Kane, E. O., 1966, *Semiconductors and Semimetals,* edited by R. K. Willardson and A. C. Beer (Academic, New York), Vol. 1, p. 75.

Koster, G. F., J. O. Dimmock, R. G. Wheeler, and H. Statz, 1963, *Properties of the Thirty-two Point Groups* (MIT Press, Cambridge, MA).

Kroemer, H., 1983, Surf. Sci. **132**, 543.

Kroemer, H., 1985, in *Proceedings of the NATO Advanced Study Institute on Molecular Beam Epitaxy and Heterostructures,* edited by L. L. Chang and K. Ploog (Nijhoff, The Hague), p. 331.

Kunc, K., and R. M. Martin, 1981, Phys. Rev. B **24**, 3445.

Kurtz, S. R., L. R. Dawson, T. E. Zipperian, and S. R. Lee, 1988, Appl. Phys. Lett. **52**, 1581.

Lamari, S., and L. J. Sham, 1988, Surf. Sci. **196**, 551.

Laurich, B. K., K. Elcess, C. G. Fonstad, J. G. Beery, C. Mailhiot, and D. L. Smith, 1989, Phys. Rev. Lett. **62**, 649.

Lee, D. H., and J. D. Joannopoulos, 1981a, Phys. Rev. B **23**, 4988.

Lee, D. H., and J. D. Joannopoulos, 1981b, Phys. Rev. B **23**, 4997.

Levine, B. F., C. G. Bethea, G. Hasnain, J. Walker, and R. J. Malik, 1988, Appl. Phys. Lett. **53**, 296.

Löwdin, P. O., 1951, J. Chem. Phys. **19**, 1396.

Luttinger, J. M., 1956, Phys. Rev. **102**, 1030.

Luttinger, J. M., and W. Kohn, 1955, Phys. Rev. **97**, 869.

Maan, J. C., 1988, Surf. Sci. **196**, 518.

Madhukar, A., N. V. Dandekar, and R. N. Nucho, 1979, J. Vac. Sci. Technol. **16**, 1507.

Madhukar, A., and J. Delgado, 1981, Solid State Commun. **37**, 199.

Madhukar, A., and R. N. Nucho, 1979, Solid State Commun. **32**, 331.

Mailhiot, C., T. C.McGill, and J. N. Schulman, 1983, J. Vac. Sci. Technol. B **1**, 439.

Mailhiot, C., T. C. McGill, and D. L. Smith, 1984, J. Vac. Sci. Technol. B **2**, 371.

Mailhiot, C., and D. L. Smith, 1986a, Phys. Rev. B **33**, 8360.

Mailhiot, C., and D. L. Smith, 1986b, J. Vac. Sci. Technol. B **4**, 996.

Mailhiot, C., and D. L. Smith, 1987a, Phys. Rev. B **35**, 1242.

Mailhiot, C., and D. L. Smith, 1987b, J. Vac. Sci. Technol. B **5**, 1268.

Mailhiot, C., and D. L. Smith, 1987c, Phys. Rev. B **36**, 2942.

Mailhiot, C., and D. L. Smith, 1988a, Solid State Commun. **66**, 859.

Mailhiot, C., and D. L. Smith, 1988b, Phys. Rev. B **38**, 5520.

Mailhiot, C., and D. L. Smith, 1988c, Phys. Rev. B **37**, 10415.

Marsh, A. C., and J. C. Inkson, 1984a, Solid State Commun. **52**, 1037.

Marsh, A. C., and J. C. Inkson, 1984b, J. Phys. C **17**, 6561.

Marsh, A. C., and J. C. Inkson, 1986, J. Phys. C **19**, 43.

Massida, S., B. I. Min, and A. J. Freeman, 1987, Phys. Rev. B **35**, 9871.

Matthews, J. W., and A. E. Blakeslee, 1974, J. Cryst. Growth **27**, 118.

Matthews, J. W., and A. E. Blakeslee, 1975, J. Cryst. Growth **29**, 273.

Matthews, J. W., and A. E. Blakeslee, 1976, J. Cryst. Growth **32**, 265.

Miller, D. A. B., D. S. Chemla, T. C. Damen, A. C. Gossard, W. Wiegmann, T. H. Wood, and C. A. Burrus, 1984a, Phys. Rev. Lett. **53**, 2173.

Miller, D. A. B., D. S. Chemla, T. C. Damen, A. C. Gossard, W. Wiegmann, T. H. Wood, and C. A. Burrus, 1984b, J. Appl. Phys. **45**, 13.

Miller, D. A. B., D. S. Chemla, T. C. Damen, A. C. Gossard, W. Wiegmann, T. H. Wood, and C. A. Burrus, 1985, Phys. Rev. B **32**, 1043.

Morrison, I., and M. Jaros, 1988, Phys. Rev. B **37**, 916.

Morrison, I., M. Jaros, and K. B. Wong, 1987, Phys. Rev. B **35**, 9693.

Mukherji, D., and B. R. Nag, 1975, Phys. Rev. B **12**, 4338.

Nakayama, T., and H. Kamimura, 1985, J. Phys. Soc. Jpn. **54**, 4726.

Nelson, J. S., C. Y. Fong, and I. P. Batra, 1987, Appl. Phys. Lett. **50**, 1595.

Ninno, D., K. B. Wong, M. A. Gell, and M. Jaros, 1985, Phys. Rev. B **32**, 2700.

Nucho, R. N., and A. Madhukar, 1978, J. Vac. Sci. Technol. **15**, 1530.

Osbourn, G. C., 1980, J. Vac. Sci. Technol. **17**, 1104.

Osbourn, G. C., 1981, J. Vac. Sci. Technol. **19**, 592.

Osbourn, G. C., 1982a, J. Appl. Phys. **53**, 1586.

Osbourn, G. C., 1982b, J. Vac. Sci. Technol. **21**, 469.

Osbourn, G. C., 1983, Phys. Rev. B **27**, 5126.

Osbourn, G. C., 1984, J. Vac. Sci. Technol. B **2**, 176.

Osbourn, G. C., 1985, J. Vac. Sci. Technol. A **3**, 826.

Osbourn, G. C., R. M. Biefeld, and P. L. Gourley, 1982, Appl. Phys. Lett. **41**, 172.

Osbourn, G. C., and D. L. Smith, 1979a, Phys. Rev. B **19**, 2124.

Osbourn, G. C., and D. L. Smith, 1979b, J. Vac. Sci. Technol. **16**, 1529.

Oshiyama, A., and M. Saito, 1987, Phys. Rev. B **36**, 6156.

Pendry, J. B., 1969, J. Phys. C **2**, 2273.

People, R., J. C. Bean, D. V. Lang, A. M. Sergent, H. L. Störmer, K. W. Wecht, R. T. Lynch, and K. Baldwin, 1984, Appl. Phys. Lett. **45**, 1231.

People, R., K. W. Wecht, K. Alavi, and A. Cho, 1983, Appl. Phys. Lett. **43**, 118.

Perdew, J. P., and M. Levy, 1983, Phys. Rev. Lett. **51**, 1884.

Pickett, W. E., and M. L. Cohen, 1978, Phys. Rev. B **18**, 939.

Pickett, W. E., S. G. Louie, and M. L. Cohen, 1978, Phys. Rev. B **17**, 815.

Ploog, K. and G. H. Döhler, 1983, Adv. Phys. **32**, 285.

Pollak, F. H., and M. Cardona, 1966, J. Phys. Chem. Solids **27**, 423.

Pollmann, J., and A. Mazur, 1983, Thin Solid Films **104**, 257.

Sai-Halasz, G. A., L. L. Chang, J.-M. Welter, C.-A. Chang, and L. Esaki, 1978, Solid State Commun. **27**, 935.

Sai-Halasz, G. A., L. Esaki, and W. A. Harrison, 1978, Phys. Rev. B **18**, 2812.

Sai-Halasz, G. A., R. Tsu, and L. Esaki, 1977, Appl. Phys. Lett. **30**, 651.

Sakaki, H., L. L. Chang, R. Ludeke, C.-A. Chang, G. A. Sai-Halasz, and L. Esaki, 1977, Appl. Phys. Lett. **31**, 211.

Sanders, G. D., and Y. C. Chang, 1985a, Phys. Rev. B **31**, 6892.

Sanders, G. D., and Y. C. Chang, 1985b, Phys. Rev. B **32**, 4285.

Sanders, G. D., and Y. C. Chang, 1987, Phys. Rev. B **35**, 1300.

Satpathy, S., R. M. Martin, and C. G. Van de Walle, 1988, Phys. Rev. B **38**, 13237.

Schirber, J. E., I. J. Fritz, and L. R. Dawson, 1985, Appl. Phys. Lett. **46**, 187.

Schulman, J. N., 1983, J. Vac. Sci. Technol. B **1**, 644.

Schulman, J. N., and Y. C. Chang, 1981, Phys. Rev. B **24**, 4445.

Schulman, J. N., and Y. C. Chang, 1983, Phys. Rev. B **27**, 2346.

Schulman, J. N., and Y. C. Chang, 1985a, Phys. Rev. B **31**, 2056.

Schulman, J. N., and Y. C. Chang, 1985b, Appl. Phys. Lett. **46**, 571.

Schulman, J. N., and Y. C. Chang, 1986, Phys. Rev. B **33**, 2594.

Schulman, J. N., and T. C. McGill, 1977, Phys. Rev. Lett. **39**, 1680.

Schulman, J. N., and T. C. McGill, 1979a, Phys. Rev. B **19**, 6341.

Schulman, J. N., and T. C. McGill, 1979b, Appl. Phys. Lett. **34**, 663.

Schulman, J. N., and T. C. McGill, 1979c, J. Vac. Sci. Technol. **16**, 1513.

Schulman, J. N., and T. C. McGill, 1981, Phys. Rev. B **23**, 4149.

Schulman, J. N., and T. C. McGill, 1985, in *Synthetic Modulated Structures,* edited by L. L. Chang and B. C. Giessen (Academic, New York), p. 77.

Sham, L. J., and M. Nakayama, 1979, Phys. Rev. B **20**, 734.

Sham, L. J., and M. Schlüter, 1983, Phys. Rev. Lett. **51**, 1888.

Shum, K., P. P. Ho, R. R. Alfano, D. F. Welch, G. W. Wicks, and L. F. Eastman, 1985, Phys. Rev. B **32**, 3806.

Smith, D. L., 1986, Solid State Commun. **57**, 919.

Smith, D. L., and C. Mailhiot, 1986, Phys. Rev. B **33**, 8345.

Smith, D. L., and C. Mailhiot, 1987a, J. Appl. Phys. **62**, 2545.

Smith, D. L., and C. Mailhiot, 1987b, J. Vac. Sci. Technol. A **5**, 2060.

Smith, D. L., and C. Mailhiot, 1987c, Phys. Rev. Lett. **58**, 1264.

Smith, D. L., and C. Mailhiot, 1988a, Surf. Sci. **196**, 683.

Smith, D. L., and C. Mailhiot, 1988b, J. Appl. Phys. **63**, 2717.

Smith, D. L., T. C. McGill, and J. N. Schulman, 1983, Appl. Phys. Lett. **43**, 180.

Stiles, M. D., and D. R. Hamann, 1988, Phys. Rev. B **38**, 2021.

Stolz, W., L. Tapfer, A. Breitschwerdt, and K. Ploog, 1985, Appl. Phys. A **38**, 97.

Taguchi, A., and T. Ohno, 1988, Phys. Rev. B **38**, 2038.

Taylor, R. I., and M. G. Burt, 1987, Semicond. Sci. Technol. **2**, 485.

Tsang, W. T., 1981, Appl. Phys. Lett. **39**, 786.

Van de Walle, C. G., and R. M. Martin, 1986a, J. Vac. Sci. Technol. B **4**, 1055.

Van de Walle, C. G., and R. M. Martin, 1986b, Phys. Rev. B **34**, 5621.

Van de Walle, C. G., and R. M. Martin, 1987, Phys. Rev. B **35**, 8154.

van der Ziel, J. P., R. Dingle, R. C. Miller, W. Wiegmann, and W. A. Nordland, Jr., 1975, Appl. Phys. Lett. **26**, 463.

Vogl, P., H. P. Hjalmarson, and J. Dow, 1983, J. Phys. Chem. Solids **44**, 365.

Wang, W. I., T. S. Kuan, and E. E. Mendez, 1985, Phys. Rev. B **31**, 6890.

Weiner, J. S., D. S. Chemla, D. A. B. Miller, T. H. Wood, D. Sivco, and A. Y. Cho, 1985, Appl. Phys. Lett. **46**, 619.

White, S. R., and L. J. Sham, 1981, Phys. Rev. Lett. **47**, 879.

Wood, D. M., S.-H. Wei, and A. Zunger, 1987, Phys. Rev. Lett. **58**, 1123.

Wood, D. M., S.-H. Wei, and A. Zunger, 1988, Phys. Rev. B **37**, 1342.

Wood, T. H., R. W. Tkach, and A. R. Chraplyvy, 1987, Appl. Phys. Lett. **50**, 798.

Woodall, J. M., 1972, J. Cryst. Growth **12**, 32.

Wu, G. Y., T. C. McGill, C. Mailhiot, and D. L. Smith, 1989, Phys. Rev. B **39**, 6060.

Wu, G. Y., T. C. McGill, D. L. Smith, and C. Mailhiot, 1987, J. Vac. Sci. Technol. A **5**, 3096.

Wu, G. Y., D. L. Smith, C. Mailhiot, and T. C. McGill, 1986, Appl. Phys. Lett. **49**, 1551.